# SCHOOL OF MECHANICAL ENGINEERING

# GEORGIA INSTITUTE OF TECHNOLOGY

## Atlanta, Georgia

# Investigations of Lubricant Rheology as Applied to Elastohydrodynamic Lubrication

**NASA GRANT No.**
**11–002–133**

By:

**S. Carlson**

**V. Turchina**

**J. Jakobsen**

Graduate Students

**D. M. Sanborn,** Assistant Professor

**W. O. Winer,** Professor & Principal Investigator

For:

**NASA–LEWIS RESEARCH CENTER**

**21000 BROOKPARK ROAD**

**CLEVELAND, OHIO 44135**

**OCTOBER 1973**

| 1. Report No. CR - 134539 | 2. Government Accession No. | 3. Recipient's Catalog No. |
|---|---|---|
| 4. Title and Subtitle INVESTIGATIONS OF LUBRICANT RHEOLOGY AS APPLIED TO ELASTOHYDRODYNAMIC LUBRICATION | | 5. Report Date October, 1973 |
| | | 6. Performing Organization Code |
| 7. Author(s) S. Carlson, V. Turchina, J. Jakobsen, D. M. Sanborn, and W. O. Winer | | 8. Performing Organization Report No. |
| 9. Performing Organization Name and Address School of Mechanical Engineering Georgia Institute of Technology Atlanta, Georgia 30332 | | 10. Work Unit No. |
| | | 11. Contract or Grant No. NGR 11-002-133 |
| 12. Sponsoring Agency Name and Address National Aeronautics and Space Administration Washington, D.C. 20546 | | 13. Type of Report and Period Covered Contractor Report |
| | | 14. Sponsoring Agency Code |

15. Supplementary Notes

Project Manager, William R. Jones, Jr., Fluid System Components Division, NASA Lewis Research Center, Cleveland, Ohio

16. Abstract

This is the final technical report for NASA Grant No. NGR 11-002-133. The research under this grant consisted of pressure-viscosity and of elastohydrodynamic lubrication (ehd) studies. The pressure viscometer has been modified to permit the measurement of viscosity at elevated pressures and shear stresses up to $5 \times 10^6$ N/m$^2$ (720 psi). This shear stress is within a factor of three of the shear stress occurring in a sliding ehd point contact such as occurs in the ehd simulator in this laboratory. Viscosity data were taken on five lubricant samples and it was found that viscous heating effects on the viscosity were predominant and not non-Newtonian behavior at the high shear stresses. The development of the infrared temperature measuring technique for the ehd simulator was completed and temperature data for a set of operating conditions and one lubricant are reported. The numerical analysis of the behavior of non-linear lubricants in the lubrication of rollers has progressed and the results are reported.

| 17. Key Words (Suggested by Author(s)) Elastohydrodynamic Lubrication Pressure Viscosity Measurements Liquid Lubricants Lubricant Rheology | 18. Distribution Statement Unclassified - unlimited | | |
|---|---|---|---|
| 19. Security Classif. (of this report) Unclassified | 20. Security Classif. (of this page) Unclassified | 21. No. of Pages ~~140~~ /4ə | 22. Price* 9, ə5 ~~$3.00~~ |

# I. INTRODUCTION

The research efforts over the past contract year have resulted in significant progress in several areas. These include:

1. The extension of pressure-viscosity data on lubricants to shear stresses of $5 \times 10^7$ d/cm$^2$ ( N/m$^2$) which is within a factor of 3 to 5 of the average shear stress occurring in the sliding ehd simulator used in this laboratory. For all lubricants examined except a high polymer blend and a dimethyl siloxane polymer the data appears to be explainable on the basis of viscous heating up to at least $5 \times 10^6$ d/cm$^2$. Analysis of the capillary flow which is in progress but not reported here is expected to verify this interpretation. It appears that for the other lubricants examined no non-Newtonian behavior was observed in the range of parameters very near those occurring in a sliding ehd contact.

2. The development of the technique for the infrared temperature measurement in an ehd film was completed and data at a set of operating conditions for a single lubricant were obtained. It is expected during the present contract year to utilize the technique to explore the thermal behavior of ehd films as a function of operating conditions and lubricant composition.

3. The computer analysis of the behavior of non-linear fluids in the lubrication of rollers has progressed to the stage where results are presented for the case of rigid cylinders with non-linear pressure dependent fluid properties. During the present contract year we expect to complete the program including elastic

1

cylinder behavior under the ehd conditions and possibly to
begin to introduce thermal effects.

Other related research conducted in the laboratory but under the
sponsorship of an NSF Grant deserves mention. A program to explore the
extent of lubricant molecular degradation in a sliding ehd contact has
been undertaken. Modification of the ehd simulator mentioned in this
report permitted the acquisition of a 10-15 μl lubricant sample from the ehd
contact just outside the high pressure region near the film exit. Samples
were also taken from the inlet zone and the supply reservior, which served
as a control sample. Eight fluids were examined and varying amounts of
molecular degradation were observed. In general the degradation increases
with increasing energy dissipation per grammole of lubricant. Typically
the degradation increased as molecular weight increased but measurable de-
gradation occurred even for relatively low molecular weight lubricants
such as 2-ethyl hexyl sebacate. This research is being prepared for
publication in the near future.

## II. LUBRICANT RHEOLOGY STUDIES

a. High Shear Stress Behavior of Some Lubricants

### Introduction

Investigations have been carried out in the high pressure viscometer to determine lubricant behavior at high shear stress. The operating temperatures, pressures and shear stresses for a lubricant in an EHD-contact can be approached in the viscometer. Furthermore, all these operational parameters can be varied independently of each other.

Five lubricants were investigated: a diester, a polyalkyl aromatic plus additive (DN 600 plus Additive), a synthetic paraffinic oil (XRM 177 F4), a silicone oil (Dimethyl Siloxane DC-200-50) and a mixture (B3J) of paraffinic, mineral oil with 11.5% polyalkylmetha-crylate (PL 4523) with an average molecular weight of .2 $\times 10^7$. A detailed description is found in Appendix A.

Apparent Newtonian behavior has been found for all fluids except B3J up to a shear stress of approximately 700 psi ($\sim 4.8 \times 10^7$) dyn/cm$^2$), which is the present upper limit of shear stress for the high pressure viscometer. Viscous dissipation heating alone seems to dominate up to the maximum stress in causing an apparent shear thinning effect. The data for the mixture (B3J) of paraffinic mineral oil and 11.5% polymer (PL 4523) shows a significant amount of scatter when the apparent viscosity is plotted against calculated capillary wall shear stress. The scatter of the data is pronounced at shear stresses above 1 – 2 psi ($\sim 10^5$ dyn/cm$^2$) making interpretation difficult in terms of liquid behavior alone.

Distinct non-liquid behavior was observed at extreme pressures

and temperatures for the lubricant DN 600 plus Additive. Similar be-
havior was observed for the siloxane but at high shear stresses, 150-600
psi (1- 4 x $10^6$dyn/cm$^2$)

## Modifications of the High Pressure Viscometer

The measurements were carried out in a high pressure viscometer.
The design and operation of the viscometer is described in [ 1 ] and [ 2 ].
The equipment has since then been modified in some respects and the
operational procedure has been changed. Figure 1 shows a schematic of the
viscometer including the most recent modifications.

The displacement transducer, which is used for flow rate measure-
ment, has been replaced with a velocity transducer, Hewlett-Packard L6V1,
and a high gain amplifier. The change was motivated by the addition of
the analog-to-digital data recorder, which made a direct signal preferable
to a differentiated signal. Interest in the possibility of measurements
of transient phenomena also motivated the change. The addition of the re-
corder has been mentioned in a previous report.

Two high precision pressure gauges (Heise Bourdon Tube Co., 40
kpsi and 100 kpsi) have been added to facilitate and improve calibration
and operations.

An infinitely variable drive has been provided for displacing the
translating piston (see Figure 1) with constant velocity. The piston is
moved hydraulically as before by charging volume III or IV with a low
pressure fluid. The flow rate of this fluid is, however, kept constant by
direct coupling of the drive unit to the piston of the charging pump. The
drive unit gives good reproducibility of the measurements. The displace-
ment of the pump piston is, however, not big enough to obtain a satisfactory
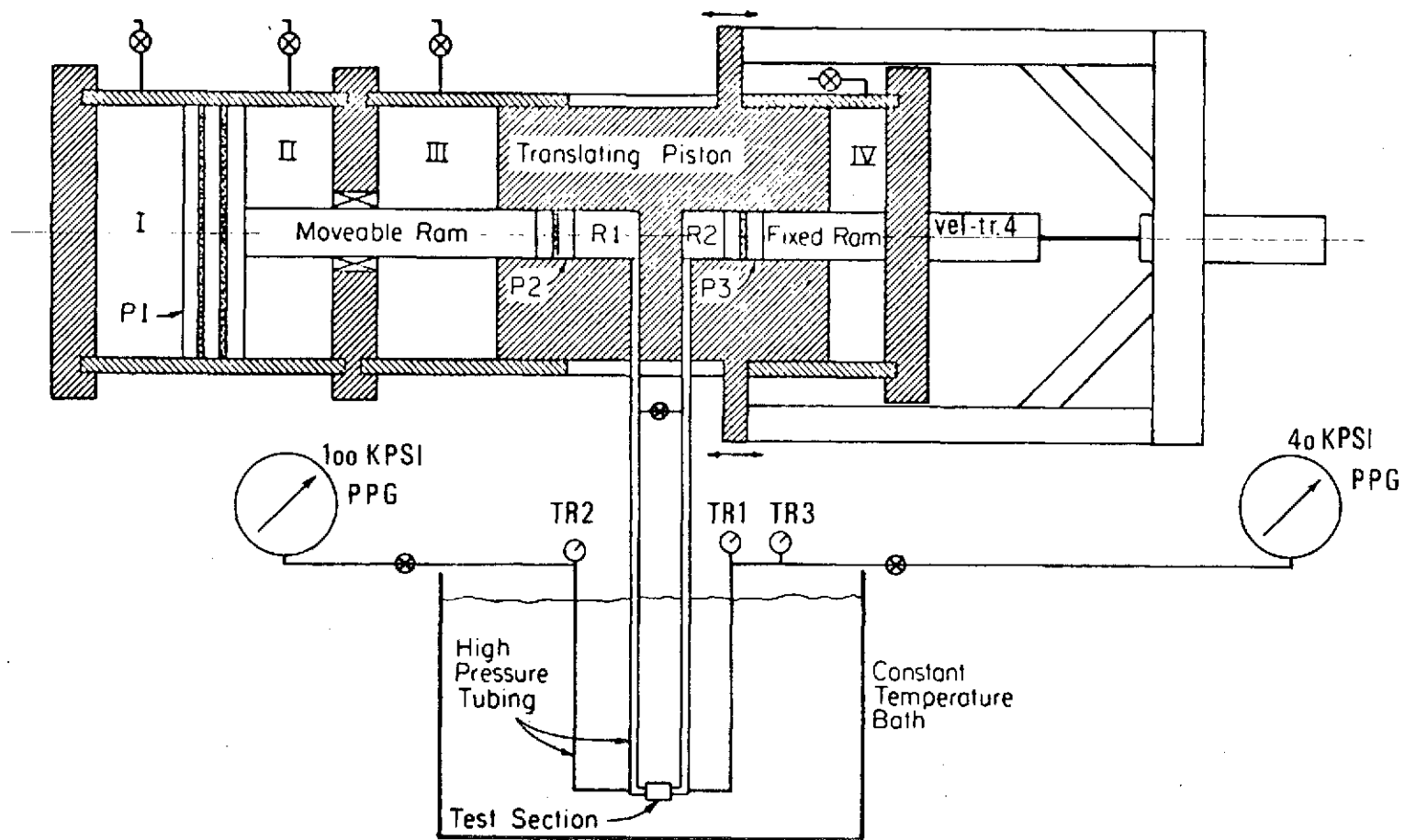
Schematic Drawing of Viscometer.

Figure 1.   The Modified Viscometer.

flow rate for measurements at the highest attainable shear stresses. Manual drive (hand pull) is therefore used for these measurements. Satisfactory reproducibility can be obtained for these higher speed displacements of the translating piston of the viscometer.

Capillaries with a low L/D ratio have been used. The smallest ratio applied has been L/D = .1 (L = 0.001 inch and D = .01 inch) this ratio, however, was used only for exploratory purposes. The entrance correction was found to be excessive for the L/D ratio of .1. Measurements were therefore not carried out with this capillary. The lowest ratio used so far is L/D = 1.35 and the smallest diameter used is .0035 inch.

The measurements were carried out with capillaries of L/D = 297, L/D = 14.9 and L/D = 1.35.

## Table I

### Capillary Dimensions and Materials

|  |  | L/D | D Inch | L Inch |
|---|---|---|---|---|
| Stainless Steel | Capillary No. 4 | 297 | .01009 | 2.996 |
| Stainless Steel | Capillary No. 1 | 14.9 | .00785 | .117 |
| Sapphire | Capillary No. 0 | 1.35 | .0035 | .0047 |

### Calibration Procedures

The viscosity measurements are carried out essentially as measurements of pressure drop and flow rate in the capillary. Shear stress is derived from the pressure drop measured with the differential pressure transducers TR1 and TR2 (Figure 1). Shear rate is determined from measurements of flow rate indicated by the velocity transducer TR4. Pressure transducer TR3 measures the pressure level.

The differential pressure transducers have been calibrated with an approach involving summation of small increments of pressure in the test section of the viscometer. Pressure readings from the Heise precision gauges are recorded simultaneously with the amplifier outputs from TR1 and TR2. Only one transducer is calibrated at a time. The pressure increments are applied with the small piston diameters pressurizing hand pump of the viscometer and controlled through measurements of the transducer-amplifier output. The output is measured with a DC-Differential Voltmeter (Hewlett-Packard 3420B) which has a precision of 10 μvolts. The voltmeter is used as a null meter. The steps are accurately monitored and measured to 6.0 volts, from an output of -3.0 volts to +3.0 volts from the symmetric transducer amplifier. The estimated accuracy of the setting of a pressure increment is equivalent to .02 volt. The precision range (10 μV) of the differential voltmeter is, therefore, completely sufficient.

The amplifier output is changed from +3.0 volts to -3.0 volts after each pressure measurement by balancing the input potentiometers of the amplifier. This change is a preparation for the next pressure in-crease. The accuracy of the change in potentiometer setting is estimated to be .01 volt. Total estimated accuracy of a measurement of a pressure increment is therefore .03 volt, on a deflection of 6.0 volts, which is equivalent to .5%. This error estimate is also valid for the voltage sum of the steps. Each increment of 6.0 volts is equivalent to approxi-mately 440 psi for 6 volts excitation of the transducers. The accuracy of the high pressure gauges is better than .1% of full scale deflection (40 psi or 100 psi). This is about 10% to 25% of a single pressure in-crement. This high inaccuracy will, however, diminish rapidly with

increasing numbers of steps. The gauge accuracy of .1% is constant. A

typical calibration of a transducer-amplifier involves nearly 100 pressure

increments. The pressure gauge error will, therefore, typically be of the

order of .1% - .2%. The estimated accuracy of .5% for the voltage sum and

the pressure gauge accuracy of .1% - .2% may safely imply that the calibra-

tion procedure is correct within considerably less than 1% of the full

range of calibration.

It is essential for the accuracy of the calibration procedure that

the system pressure remain constant during the change of potentiometer

setting of amplifier output from +3.0 volts to -3.0 volts. The constancy

of system pressure has been assured by steady state conditions. These are

obtained when temperature transients, possible relaxation of seals, etc.,

have faded away from each pressure increment. The change of potentiometer

setting can be carried out in about 10 seconds. The constancy of system

pressure during this period can be verified and measured with the trans-

ducer-amplifier, which is not undergoing calibration. Changes as small as

30 millivolts (~ 2.0 psi) can be detected with this channel when it is

used as null indicator. System pressure constancy is assumed to be

achieved when no pressure variation is detected for a period of about 100

seconds.

The exitation voltage for the transducers was measured continuously

during the calibration procedure. Changes in the voltage were, however,

insignificant and about .1 millivolts. The average value was applied in

calculations. Standard excitation voltage level is 6 volts. Some high

shear stress measurements, however, were carried out with 1.5 volt excita-

tion. The transducer sensitivity is directly proportional to the excitation

voltage. Measurement accuracy is, therefore, not impaired by changes in excitation voltage. A series of control measurements confirmed this assumption.

The pressure level transducer (TR3, Figure 1) was calibrated by recording transducer output and pressure readings from the high precision gauges. An interval of 5 kpsi was used. The transducer characteristic was linear above 5 kpsi within calibration accuracy.

The velocity transducer measures linear, straight line velocity. It consists of a shielded coil and an axially located, cylindrical core. The core is a high coercitive force permanent magnet. Motion of the core generates a voltage in the coil proportional to linear velocity with an output of 545 millivolts/ips. The working range is 1.0 inch. Manufacturer's specifications show a linearity of better than 1% and output variations between 95% and 100% of nominal output over the total working range.

Considerations of the function of the transducer suggest considerably increased accuracy above the mentioned magnitude of ±2.5%, however, for a reduced working range. A working range of about 0.5 inch was, therefore, maintained during the experiment.

The transducer and amplifier calibration were carried out as measurements of displacement and corresponding time duration. The velocity of the traversing piston was maintained constant with the above mentioned drive unit during the calibration. The amplifier output was sampled by the appropriate channel on the analog-to-digital recorder. A typical calibration speed was 0.001 in/sec.

These switches were connected electrically over the inputs of two dummy channels on the analog-to-digital converter. The opening times can, therefore, easily be assessed from a computer printout.

The travelled distance between activation of the switches was measured with a precision dial indicator and was typically 0.01 - 0.02 inch. The accuracy of the indicator is guaranteed to be better than 0.0001 inch. This was confirmed in a series of measurements performed with parallel gauge blocks (Grade L).

The amplifier gain was approximately 890. The transfer function for the transducer and amplifier was therefore 485 V/in/sec. The input to the analog-to-digital recorder will be 485 millivolts for a calibrating speed of 0.001 in/sec. This output level of about 500 mv is appropriate for accurate recording by the analog-to-digital converter, which has a threshold of destinction of 4.85 millivolts. This 1% ratio between threshold and signal magnitude is however lowered considerably by the great amount of sampled data and the following averaging process in the computer treatment.

Two calibration fluids were used, a viscosity standard, S-60 from Cannon Instrument Company, and diester (bis 2-ethylhexylsebacate) from Rohm and Haas Company. Table 2 summarizes the viscosities of the fluids.

Table 2

Viscosities (cp) of Calibration Fluids
at Atmospheric Pressure

|         | 100 °F   | 210 °F   | 300 °F  |
|---------|----------|----------|---------|
| S-60    | 51.06 cp | 5.899 cp | ---     |
| Diester | 11.41 cp | 2.86 cp  | 1.46 cp |

Viscosities for S-60 are from the manufacturer's specifications.

The fluid S-60 was used only at low shear stress calibrations. The diester was used over the total range of shear stress. Both fluids are assumed to be Newtonian liquids in the sense that the ratio between measured shear stress and shear rate is constant.

The viscosity of the diester was determined at 100 °F, 210 °F and 300 °F with a Cannon-Fenske Routine Glass viscometer 150-E707. This viscometer was calibrated with the S-60 fluid. Capillary 4 (see Table I) was used as the standard capillary for high pressure measurements. Calibration of capillary 4 was carried out at atmospheric pressure with diester and checked with the S-60 fluid. The diameter of capillary 4 was found to be 0.01009 inch. Later calibrations confirmed this measurement within 5 μinch.

These statements about the diameter of capillary 4 assume the physical length of the capillary tube to be 2.996 ± .001 inch as measured with a micrometer screw. The diameter 0.01009 inch contains, therefore, all possible corrections originating outside the capillary cavity, however, only for Newtonian liquids.

Calibration of the capillary 1 was carried out as a comparison of low shear stress measurements with capillary 4 measurements. The diester was used as calibration fluid. The pressure range applied was 10 - 40 kpsi. Calibration temperature was 31.9 °F ± 0.1 °F. This temperature was selected because the viscosity of the calibrating fluid for the applied pressures is then about $10^3$ cp, well within the expected viscosity range in the elastohydrodynamic lubrication film. The selected calibration temperature is also appropriate for comparison with previous work, notably ASME 1953 [ 3 ].

The diameter of capillary 1 was found to be 0.00785 inch for a measured physical length of 0.117 inch. This diameter statement includes all possible corrections originating outside the capillary cavity, however, only for Newtonian liquids.

The capillary with $L/D = 1.35$, capillary 0, is a sapphire ring (see Figure 2) embedded in stainless steel high pressure seals of a similar type as employed by AMINCO (AMINCO is the manufacturer of the utilized standard high pressure tubes and fittings). The seals are of local design and manufacture.

Calibration of capillary 0 was carried out as a comparison of low shear stress measurements with capillary 1 and capillary 4 measurements. The calibration fluid was the diester. The applied pressure range was 10 – 40 kpsi. The calibration was carried out at $31.9 \pm 0.1$ °F. The diameter of the sapphire capillary was determined with a high power microscope (200X and 500X) to be 0.0035 inch with an estimated accuracy of 3%. The magnitude 0.00348 inch was actually used in the computer program because this number was believed to be the most nearly accurate.

The comparison with capillary 1 and capillary 4 measurements showed the effective capillary length to be 0.0047 inch. This calibration also takes into account all possible corrections originating outside the cylindrical part of the capillary cavity. It will, therefore, also give a correct shear stress determination, according to the expression $\tau = \Delta p D / 4L$.

One known correction originating outside the capillary is the pressure drop in the conical part of the sapphire (see Figure 2). An estimate of this correction can be given in terms of equivalent length for the capillary diameter $D_0$. The equivalent length is $D_0/6 \, \mathrm{tg}\, \psi$, where $2\psi$ is

Figure 2
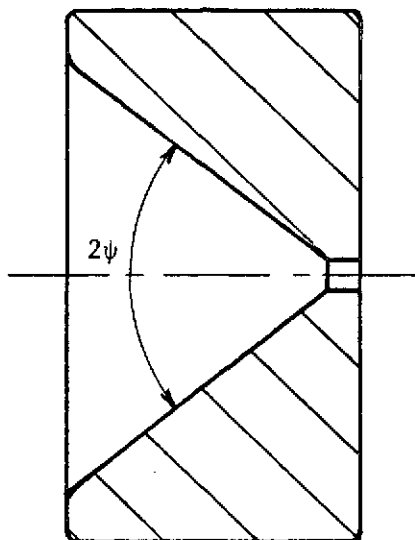


Capillary 0.   Sapphire.   Outside diameter .055 inch.   Thick-
ness .030 inch.   Cone angle ≃ 80°.   Capillary
diameter .0035 inch. Capillary length ≃ .0047 inch.

the cone angle, see Appendix B.

The cone angle of capillary 0 is approximately 80°, which gives an

equivalent length of about 0.0008 inch and, therefore, a physical length

of the capillary of about 0.0039 inch.   This is somewhat greater than the

manufacturer's specified length of 0.0035 inch.   The difference may be as-

sociated with a further correction due to flow contraction and dispersion

outside the capillary cavity or possibly to a small inaccuracy in the manu-

facture.

No directional effect was found for the capillaries during the

calibration measurements.   Reversal of flow direction for all capillaries

gave consistantly identical results within the measuring accuracy.

The distance in the capillary from the entrance to the point of

nearly fully developed flow (95%) is called the entrance length [1 ].

The calibration of capillary 0 was carried out for entrance length from 1%

down to 0.03%. The corresponding Reynolds numbers for the low shear stress

measurements were 0.2 to 0.006. Entrance lengths as great as 4% did not,

however, produce significant deviations in apparent viscosity. It should be

added that calibration for capillary 1 was carried out for equally small

Reynolds numbers.

The calibration measurements are found in Table 5 - Diester, 32 °F.

The measurements with the standard high pressure capillary, capillary 4,

are plotted in Figures 3 and 4 . Table 3 gives a comparison of the averaged

data of a diester with data for a diester reported as sample A1 in the ASME

Pressure Viscosity Report of 1953 [ 3].

The data summarized in Table 3 are taken from two different charges.

The dates of the measurements are about 20 years apart. The viscosity

values in columns 1973 and 1953 are interpolated graphically. This process

also incorporates inaccuracies in the data of corresponding pressure levels

(5 - 40 kpsi) aside from graphically generated inaccuracies in the visco-

sity values. It must furthermore be delineated that the viscosity values

are obtained in two basically different ways of calibration and measurement

approaches.

Table 3 shows that the 1973 data deviate less than ± 2% from the

1953 data. This small magnitude of deviation can be interpreted as a veri-

fication and a support of the previous stated measurement inaccuracy of

± 1%, when all prepositioned conditions for the data of Table 3 are taken

into consideration.

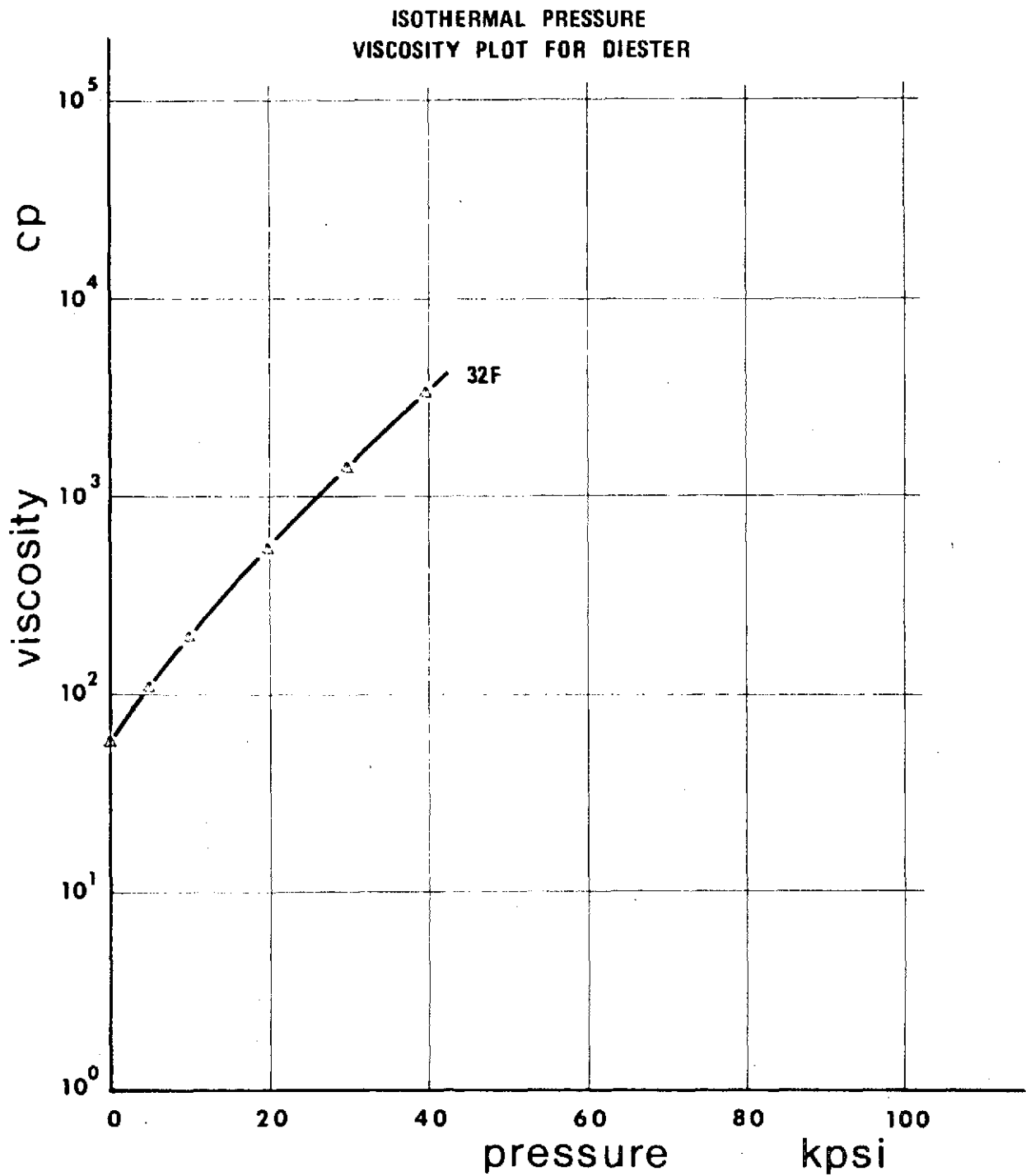The data of Table 3 indicate also that a search for further

ISOTHERMAL PRESSURE
VISCOSITY PLOT FOR DIESTER

Figure 3.   Isothermal Pressure Viscosity Plot for
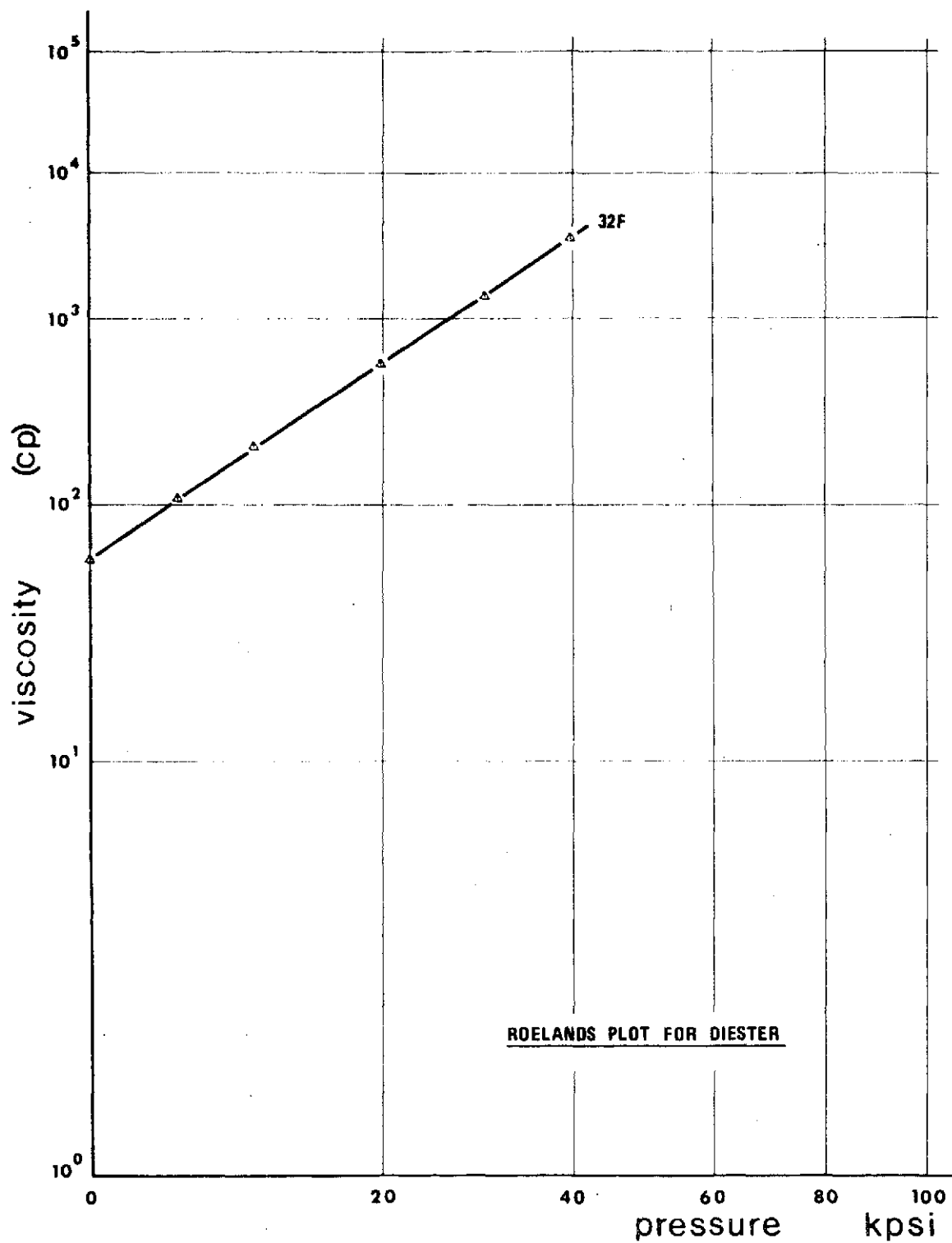Diester.   (Semilog Presentation.)

Figure 4 . Roelands Plot for Diester.

Table 3

## Pressure Viscosity Relation    (Diesters)

| 32 °F at: | Data 1973 – Capillary 4 | ASME 1953 – Al | Deviation of 1973 Data from ASME 1953 Data |
|---|---|---|---|
| 0 kpsi | 57.5 cp | 56.8 cp | +1.2% |
| 5 | 109.5 cp | 108 cp | +1.4% |
| 10 | 196. cp | 194 cp | +1.0% |
| 20 | 546. cp | 547. cp | – .2% |
| 30 | 1400. cp | 1420. cp | -1.4% |
| 40 | 3365. cp | 3310. cp | +1.7% |

All viscosities are interpolated graphically on expanded semilog diagrams.

For the column:  DATA 1973 – capillary 4:

Measurements at pressure levels 5 kpsi to 40 kpsi are performed in the high pressure viscometer. Measurements at atmospheric pressure are extrapolated from straight line pressure viscosity characteristics mapped on a rectifying diagram (lnln$\eta$T) of type ASTM D 341-43.

increase of measuring accuracy will probably not be of particularly great value. An accuracy of ± 1% seems to be satisfactory for general investigations of high pressure properties of lubricants as long as the lubricants are no more well defined. The conclusions of the work are not at all impaired by a ± 1% accuracy of the measurements. A greater accuracy would only have contributed insignificantly, it is believed, to refinements of the results.

Figure 5 shows the viscosity measurements plotted as function of shear stress. The figure illustrates the high degree of correspondence of the low shear stress measurements for capillary 0 and capillary 1 with those of capillary 4. The high shear stress measurements of Figure 5 ($\mu$ vs $\tau$) show for both capillary 0 and capillary 1 an apparent shear thinning behavior of the diester. This calibration liquid, which is assumed to have completely Newtonian properties, is presumably then subject to dissipation heating in the capillary cavity. A series of measurements with only one capillary cannot easily discern shear thinning effects from dissipation. Comparison between measurements with different L/D ratios will allow a differentiation of these effects.

The measurements plotted in Figure 5 for capillary 0 (L/D = 1.35) and capillary 1 (L/D = 14.9) show for the same fluid at each pressure level consistently lower measured viscosity values for capillary 1 in the overlap zone of the shear stress ranges of the capillaries. This holds true whatever shear stress or shear rate is used as a basis of comparison.

The general form of the characteristics of Figure 5 at 20 – 30 – 40 kpsi and particularly the comparison between capillary 0 and capillary 1 measurements at the overlap zone ( $\sim 5 \times 10^5$ dyn/cm$^2$) where capillary 1
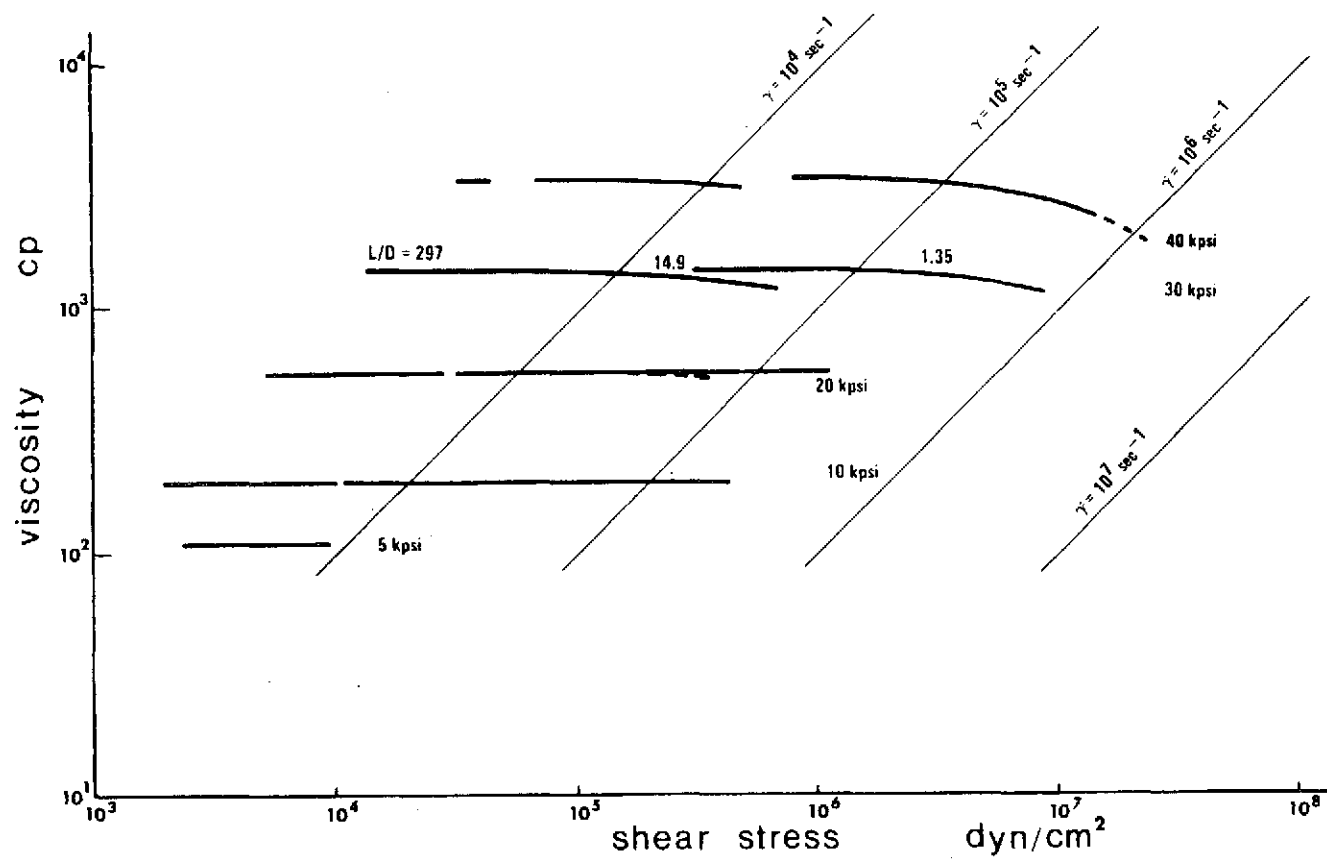
Figure 5.  Flow Curves for Diester, Calibration, T = 32°F.

results deviate from the Newtonian characteristic, indicates strongly that shear thinning effects cannot explain the high shear stress behavior of the diester as it is measured with capillary 1.

The diester behaves, therefore, as a Newtonian liquid up to about $10^6$ dyn/cm$^2$ which is the upper limit for capillary 1 measurements in this series of experiements. The common form of the characteristic leads furthermore to the supposition that the diester behaves as a Newtonian fluid up to about $2 \times 10^7$ dyn/cm$^2$ (about 300 psi) shear stress.

Attempts were undertaken to use capillaries with L/D as small as 0.1 in order to increase the upper limit for the shear stress at the capillary wall. The corrections, which necessarily had to be applied, made interpretation of the measurements questionable. The approach was therefore abandoned.

## Fluid Measurements

Diester. The high shear stress behavior of diester was investigated at somewhat greater viscosity levels than the calibration measurements. Higher viscosities were achieved by applying a low temperature of 10° F and maintaining the pressure levels 10 - 20 - 30 - 40 kpsi. Figure 6 shows the results of the measurements as a graphical presentation. Measurements with capillary 4 were not performed because the low shear stress viscosities measured with capillary 0 and capillary 1 showed consistency with previously obtained data for the diester when interpreted through mapping on a ASTM Standard Viscosity-Temperature Chart. The mapping is illustrated in Figure 7.

The presentation of Figure 6 shows the same values of limiting low shear stress viscosity for capillary 0 and for capillary 1 at every pressure
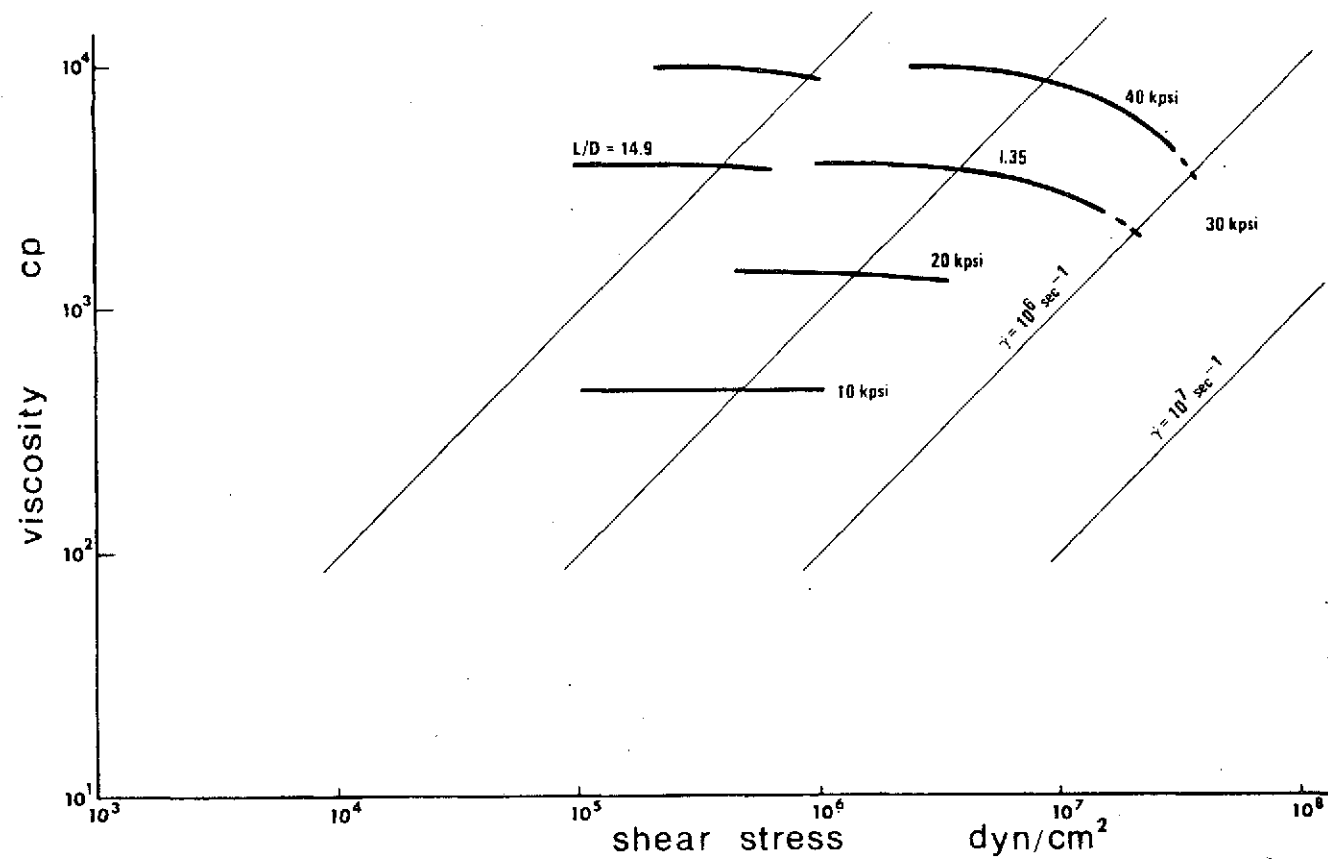
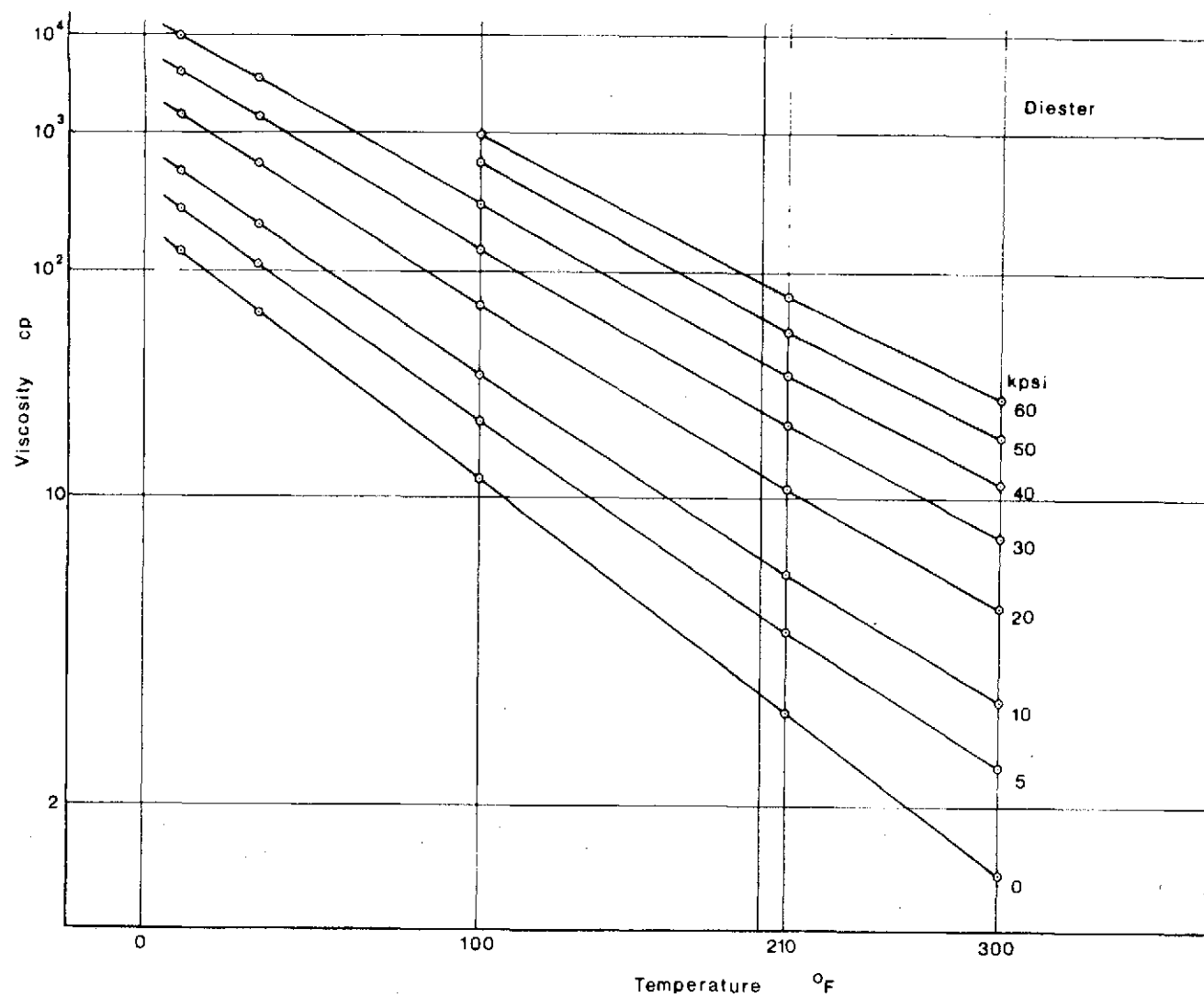Figure 6 .   Flow Curves for Diester, High Shear Stress, T = 10°F.

Figure 7 . Temperature Pressure Viscosity Presentation for Diester. (ASTM D-341-43).

level. These viscosities are within procedural accuracy of the viscosities

predicted by straight line characteristics as applied in Figure 8.

Comparison with Figure 3 shows that the high shear stress charac-

teristics have the same general form of constant shear stress. The measure-

ments with capillary 1 also show deviation at the same shear stress or the

same shear rate downward from the Newtonian characteristic measured with

capillary 0 in the same way as found in Figure 5. This confirms the state-

ment that the deviation of capillary 1 measurements at high shear cannot be

explained by a shear thinning effect.

The flow curves of Figure 5 (Diester, 10°F) are similar to the

flow curves for the diester at 32°F (Figure 5). A translation along the

viscosity axis (shear stress constant) will allow one flow curve to be

superimposed on another flow curve. This holds also for flow curves

measured at the same temperature. These observations suggest that the

mechanism responsible for the flow curve deviation from constant viscosity

is dependent on the pressure drop over the capillary, capillary geometry

(L and D), and possibly some fluid properties; but it is not dependent on

viscosity level nor on shear rate. It can be shown that dissipation heating

satisfies these requirements.

The highest shear stress shown in Figure 6 is about $3 \times 10^7$ dyn/cm$^2$

($\sim$435 psi). Slightly higher stresses were applied. However, amplifier

saturation of the velocity signal prevented proper measurements from being

taken. Similar conditions had also arisen for the diester, 32°F, 40 kpsi

(Figure 5 ). These measurements are not incorporated in Table 5.

An extrapolated flow curve signature has been used in Figure 5 and 6 to

show an estimated behavior of the fluid.

Figure 7 shows the low shear stress behavior of diester over the temperature range covered. Table 4 gives the numerical values of the pressure temperature viscosity characteristics of the diester plotted in Figure 7.

The rectifying diagramatic presentation of Figure 7 is essentially that of the ASTM Standard Viscosity-Temperature Charts (D 341 - 43). The generating formula for the chart is $\ln\ln(\nu + c_o) = \ln A - Q \ln T$, for example, see reference [ 4 ], where $\nu$ is the kinematic viscosity in centi-stokes at the absolute temperature T (°R) and $c_o$, A , Q are constants ($c_o$ = .6 cs for $\nu$ < 2cs). A and Q are material constants. The usefulness of these rectifying charts is based on the observation that mineral oils plot as straight lines presumably, however, only at atmospheric pressure. Hersey [ 4] states that fair results can be obtained by plotting the values of dynamic viscosity directly using the scale of kinematic viscosities. Figure 7 is generated with such a simplified plotting method.

The error that arises from the simplified use of the rectifying charts is, however, not significant for use in traction investigations of elastohydrodynamic lubrication. The density of the lubricant varies at most from about 0.9 g/cm$^3$ to 1.1 g/cm$^3$ [ 3 ] in the pressure and tempera-ture ranges of interest. This is a change in density of ± 10%. The equivalent plotted error is totally about ± 0.7% at 1000 cp, ± 1.4% at 100 cp and ± 5% at 10 cp. The relative error between consecutive points is certainly smaller. A somewhat greater error may be expected because the characteristics for many fluids tend to show a slight curvature above atmospheric pressure and for large temperature ranges. The lower bound for the viscosity range of interest in traction investigations is 100 cp to

Table **4**

Pressure Temperature Viscosity Relationship for Diester

| | Temperature | | | | |
|---|---|---|---|---|---|
| kpsi | 10 | 32 | 100 | 210 | 300 °F |
| | units centipoise | | | | |
| 0 | [ 130. ] | [ 57.5 ] | 11.41 | 2.86 | 1.46 |
| 5 | 250. | 109.5 | 18.6 | 4.3 | 2.28 |
| 10 | 472. | 196.0 | 28.95 | 6.0 | 3.05 |
| 20 | 1420. | 546 | 64.2 | 10.7 | 4.92 |
| 30 | 3900. | 1400. | 134.5 | 18.0 | 7.52 |
| 40 | 9900. | 3365. | 268. | 79.1 | 11.1 |
| 50 | – | – | 510. | 46.7 | 16.2 |
| 60 | – | – | 940. | 72.0 | 23.2 |
| 70 | – | – | – | – | |

The table values above  kpsi are interpolated graphically on expanded semilog diagrams.

[ 4 ]   :      Extrapolated from straight line pressure viscosity characteristics mapped on a rectifying diagram $\ln\ln\eta - \ln T$ of type ASTM D  341-43.

1000 cp. The maximum error due to simplifications of the generating for-
mula is then about 1%. It will in most cases be considerably smaller.
The simplified plotting method may, therefore, safely be applied without
any appreciable loss of accuracy.

The constant $c_o$ (0.6cs) can also be discarded for traction investi-
gations. The magnitude of this change is about 0.1% at 100 cp and dimin-
ishes rapidly for higher viscosities. The generating formula can there-
fore be regarded as having the form: $\ln\ln\eta = \ln A - Q\ln T$ which conveni-
ently is a formula with two constants. The constant A stands for some
defined base viscosity. The constant Q expresses the change of viscosity
with temperature such that a large Q represents great changes in visco-
sity for a given temperature change.

Figure 7 shows that diester has straight line characteristics
in the $\ln\ln - \ln$ rectifying diagram for viscosities above 100 cp. It is
also seen that the characteristics are straight lines for the ranges 0 -
40 kpsi and 10°F to 100°F as well as for atmospheric pressure and 10°F to
300°F. There is a minor curvature at all the reported pressure levels
above atmospheric pressure and above 100°F, when the viscosity is less
than 100 cp. The curvature is, however, equivalent to deviations less
than about 5% of predicted viscosities. These deviations are furthermore
found at viscosity levels, less than 100 cp, which is outside the range
of interest for the high pressure range in elastohydrodynamic lubrication.

The high shear stress measurements of the calibration liquid,
diester, show that dissipation heating most likely is the cause of
the well observed deviation of flow curves of many lubricants from the
Newtonian characteristics toward smaller apparent viscosities for high

shear stress conditions. It was further shown that the diester has a con-
stant viscosity in the shear stress range up to about 14 psi ($\sim 10^6 dyn/cm^2$)
measured with capillary 1. This indicates that the diester is a Newtonian
liquid up to 14 psi. Non-Newtonian effects thus do not participate in
the generation of the deviationg flow curves for diester measured with
capillary 1.

Heat generation per unit volume and unit time is equal to the
product of shear stress and shear rate. The measurements of the diester
showed that the flow curves, Figures 5 and 6, for both capillary 1 and 0
were influenced by changes in shear stress, but hardly influenced by
changes in viscosity, or changes in shear rate. Decreasing shear rates,
or lower flow velocities, give equally longer resident times for the
liquid in the same capillary. The heat generation per unit volume in a
capillary is, therefore, independent of the shear rate and depends alone
on the shear stress, or on the pressure drop experienced by the fluid.
The temperature changes depend on the amount of heat generated, on
capillary geometry (location in the capillary cavity) and on fluid proper-
ties. Possible important fluid parameters are specific heat and density.

The specific heat per unit mass, and the density are both very
nearly constant for many lubricants. The values are in the range
$c_v$: 0.3 to 0.5 Btu/lbm°F (0.3 to 0.5 cal/g°C) and $\rho$:0.03 to 0.036 lbm/in$^3$
(0.83 to 1.0 g/cm$^3$) giving a specific heat c per unit volume of 85 - 170
lbf/in$^2$°F. The thermal conductivity and the previously mentioned material
constant Q are other possible important parameters.

The thermal conductivity does not vary drastically for mineral
oil lubricants and for many of the synthetic lubricants. The operational
values are in the range 0.015 - 0.017 lbf/sec°F (.7 - 0.8 Btu/hr°F ft)

with lower and upper extremes at 0.013 and 0.020 lbf/sec°F. The conduc-
tivity decreases about 3% per 100°F temperature increase and decreases
about 1% per percent increase in density [4]. Deviations from these
levels of thermal conductivities are few. Table 5 gives some examples of
deviations.

Dimethyl Siloxane DC-200-50. One outstanding property of sili-
cone oils is the relatively small decrease of viscosity with increasing
temperature. The Q-exponent is a factor of 2 to 4 less than the Q-
exponent of the diester. The flow curves for siloxane will therefore ex-
pectedly show considerably less deviation from the Newtonian characteris-
tic than the diester flow'curve for the same shear stress. Typical flow
curves for the siloxane and for the diester is plotted in Figure 8 . The
figure shows the much smaller loss of apparent viscosity for the siloxane,
thus supporting the hypothesis of heat dissipation as an important
mechanism in generating the deviating flow curves for the capillary 0
measurements.

Figures 9, 10 and 11 show the low shear behavior of the siloxane
as a function of pressure at 100°F, 210°F and 300°F. The characteristics
of Figure 9a are S-shaped and have inflection points at 20 - 60 kpsi.
This is similar to the shape of the characteristic of a 550 silicone oil
reported in [3 ] as sample 53 - H.

Figure 11 shows the considerably smaller slope of the characteris-
tics as compared to the curves of Figure 7 - Diester. Table 10 gives the
results of the measurements plotted in Figures 9, 10, 11. These measure-
ments were carried out before the modifications to the high pressure visco-
meter were made. A second series of measurements of the siloxane were

Table 5

The Coefficient of Heat Conduction for Some Liquids

|  | $k_t (lb_f/^\circ Fsec)$ |
|---|---|
| Clorofluorcarbon | .0087 |
| Fluorinated polyether | .0117 |
| Most hydrocarbon and methyl siloxane lubricants | .0150 to .0170 |
| Methylalcohol | .024 |
| Fluorsilicones | .034 |
| Glycerin | .036 |
| Water-Glycol mixtures | .05 to .06 |
| Water 32 $^\circ$F | .073 |
| Water 140 $^\circ$F | .082 |

Values from references [ 5 ] and [ 6 ]
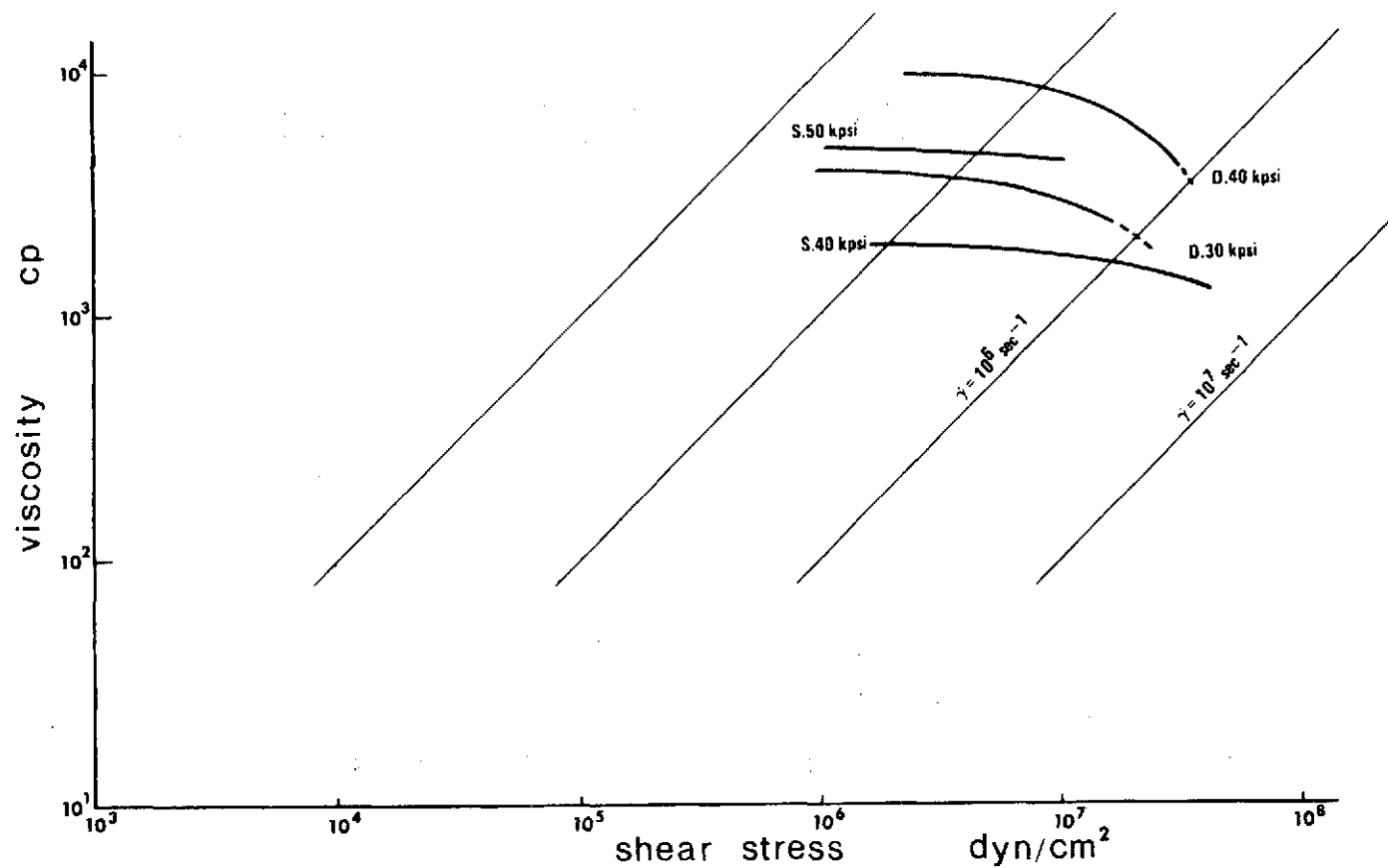
Figure 8 . Typical Flow Curves for Siloxane (S) and Diester (D). (Deviation from Newtonian behavior is more pronounced for the diester, which has a greater Q-exponent, than for the Siloxane.
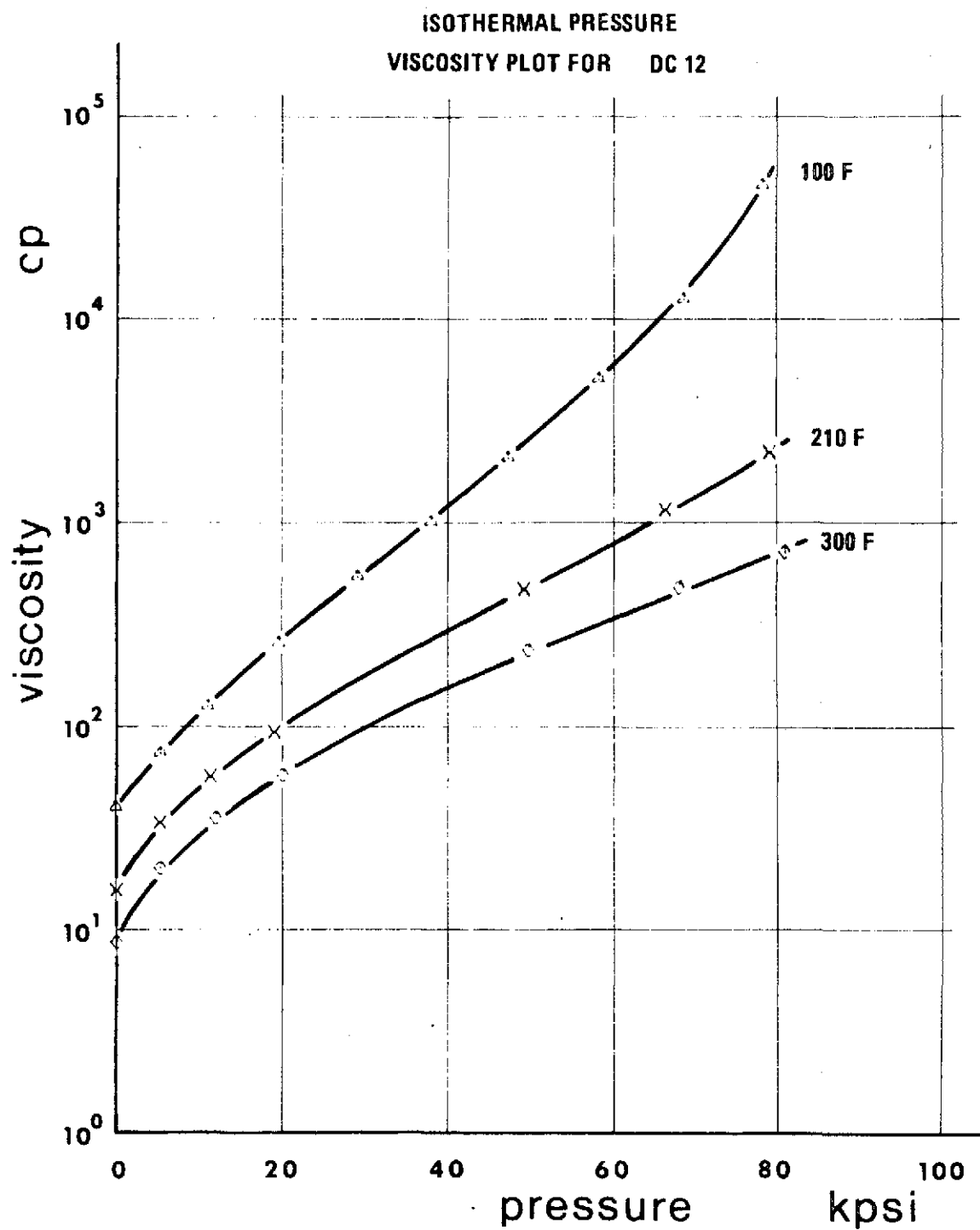
Figure 9. Low Shear Pressure Temperature Viscosity Characteristics
for Dimethyl Siloxane DC-200-50 (DC-12). (Semilog
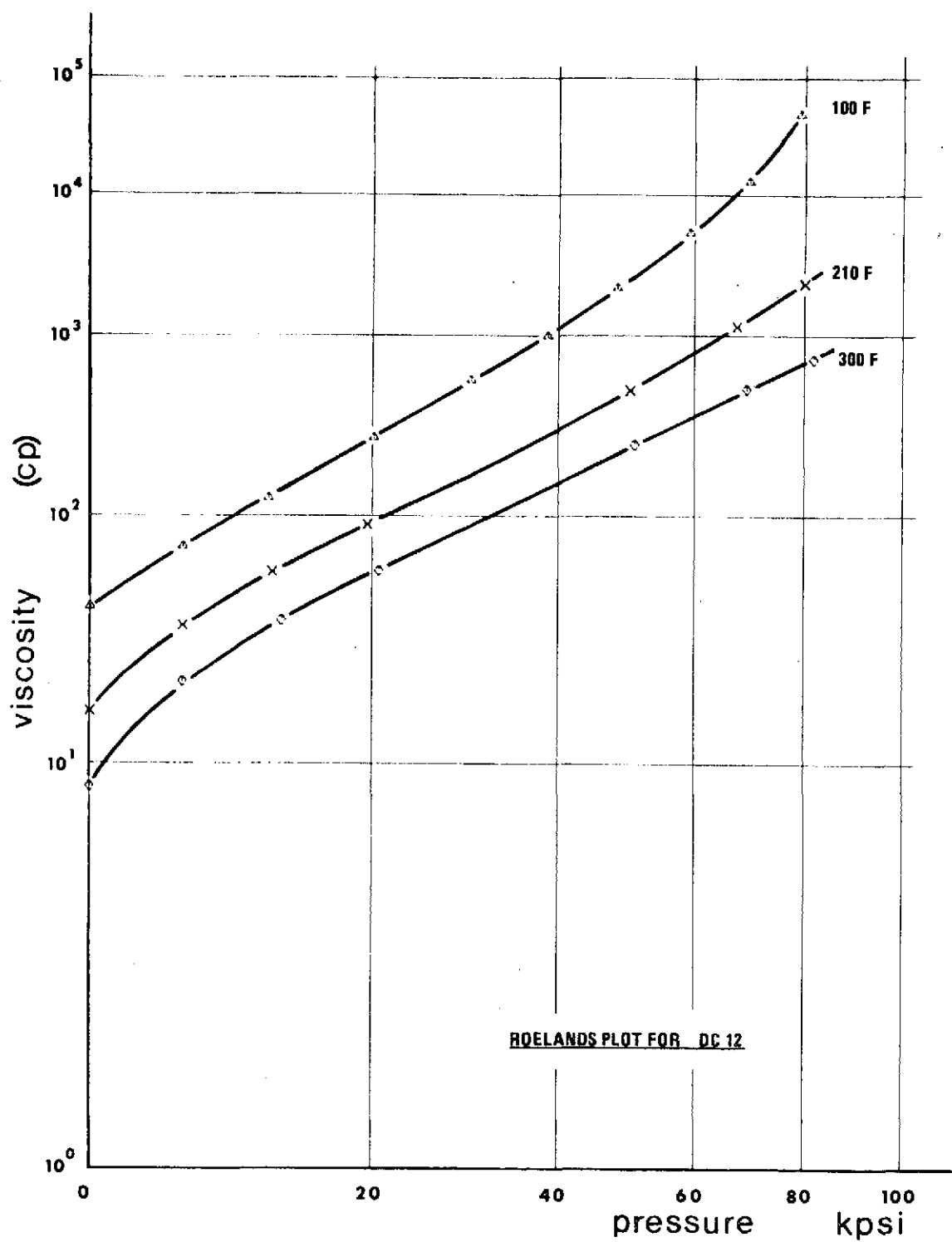representation.)

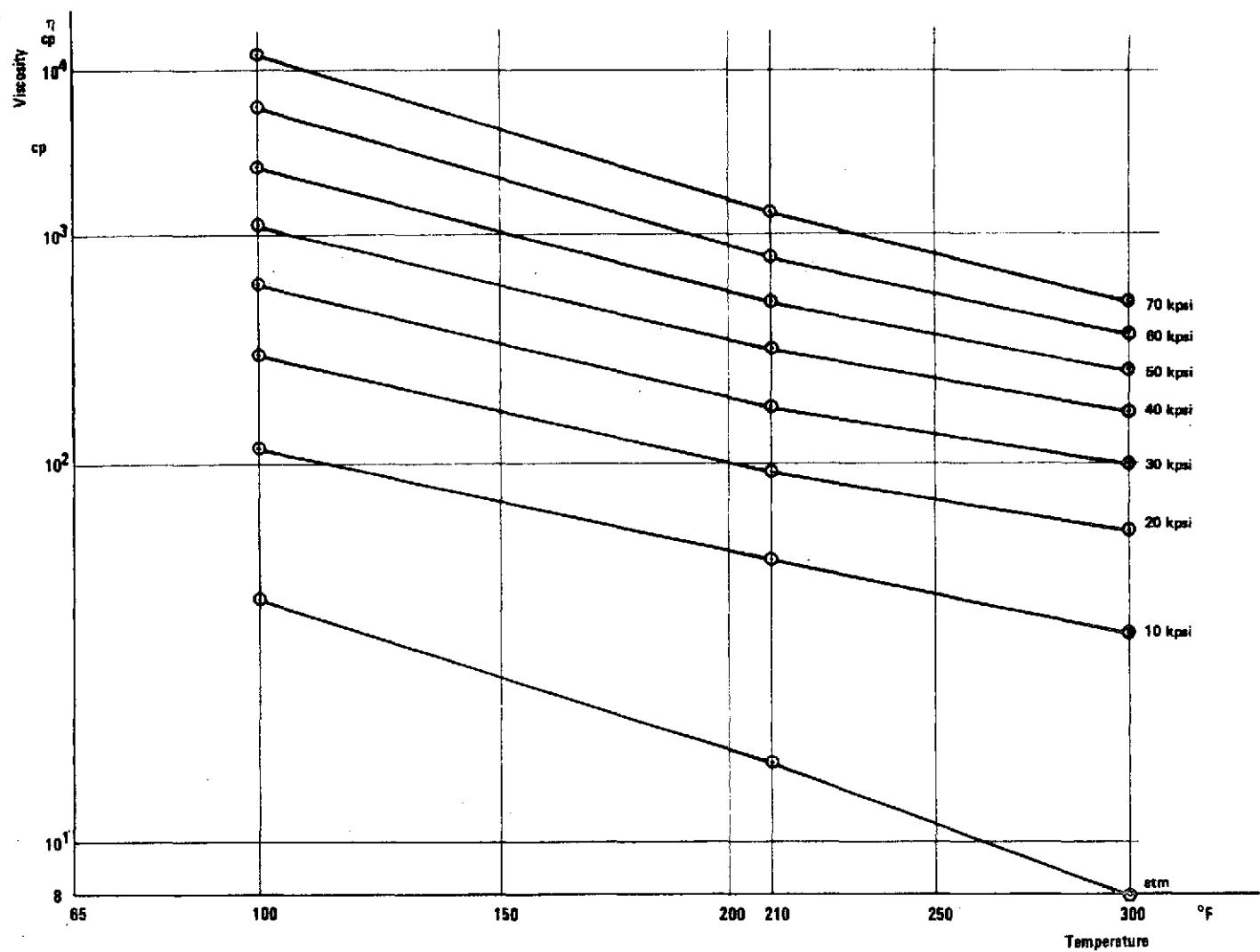Figure 10. Low Shear Pressure Temperature Viscosity Characteristics for Dimethyl Siloxane DC-200-50. (DC-12.)

Figure 11   Low Shear Temperature Pressure Viscosity Characteristics
for Dimethyl Siloxane DC-200-50.   (DC-12).

Table  6.  Dimethyl Siloxane DC - 200 - 50

L/D = 297  Averaged Data Points

DC200-20CS,CAP4,100F,3-23-71

| P (PSI) | V (CP) |
|---|---|
| .00000 | .39100+02 |
| .53657+04 | .72110+02 |
| .11194+05 | .12259+03 |
| .19878+05 | .25050+03 |
| .29445+05 | .52787+03 |
| .38386+05 | .97799+03 |
| .47685+05 | .20003+04 |
| .58765+05 | .48742+04 |
| .69115+05 | .12161+05 |
| .78921+05 | .44270+05 |

ALPHA STAR=   .96336-04
ALPHA OT=   .13550-03

DC200-20CS,210F,CAP4,3 24-71

| P (PSI) | V (CP) |
|---|---|
| .00000 | .15200+02 |
| .53667+04 | .32812+02 |
| .11503+05 | .55443+02 |
| .19311+05 | .91511+02 |
| .49638+05 | .45749+03 |
| .66850+05 | .11242+04 |
| .79730+05 | .21371+04 |

ALPHA STAR=   .95620-04
ALPHA OT=   .20481-03

DC200-20CS,300F,CAP4,3 25-71

| P (PSI) | V (CP) |
|---|---|
| .00000 | .84600+01 |
| .53631+04 | .19630+02 |
| .12202+05 | .34464+02 |
| .20354+05 | .56270+02 |
| .50249+05 | .23016+03 |
| .68638+05 | .46701+03 |
| .81603+05 | .69932+03 |

ALPHA STAR=   .95546-04
ALPHA OT=   .24187-03

carried out at low temperatures 32°F, 75°F and 100°F. Figures 12 and 13 summarize these measurements. The same general characteristics of the siloxane were found in the low temperature range. The pressure viscosity curve at 32°F, Figure 12, is S-shaped, however, the inflection point is located as low as 15 kpsi. The temperature viscosity characteristics, Figure 13, at low temperatures are straight lines with slopes of the same magnitude as the slopes in the temperature range 100-210°F, Figure 11 .

High shear stress measurements of the siloxane fluid were carried out at 75°F. The results are shown in Table 11 and Figure 14 . The flow curves, Figure 12, for capillary 1 measurements also deviate downward from the curves of capillary 0 at the same shear stress or the same shear rate in the shear stress range covered by both capillaries. Shear thinning is therefore not present for dimethyl siloxane for stresses up to at least $4 \times 10^6 \text{dyn/cm}^2$ (57 psi). This is particularly well illustrated with the flow curves at 30 kpsi where the overlap zone is more than a decade wide, $10^5 - 10^6 \text{dyn/cm}^2$, Figure 14. The flow curves for the siloxane fluid for both capillaries are seen to be similar in form. A translation along the viscosity axis will allow one flow to be superimposed on another curve. This indicates that dissipation heating is the cause of the observed deviation from Newtonian behavior for both capillary 1 and capillary 0 as was the case for the diester, and suggests further that the range where shear thinning effects are absent can be extended to the highest stress reported in Figure 12, which is $4 \times 10^7 \text{dyn/cm}^2$ (570psi).

Partial blockage of the capillary was occasionally experienced during the high shear experiment with capillary 0. Figure 15 shows the results from measurements at 30 and 40 kpsi with such partially blocked
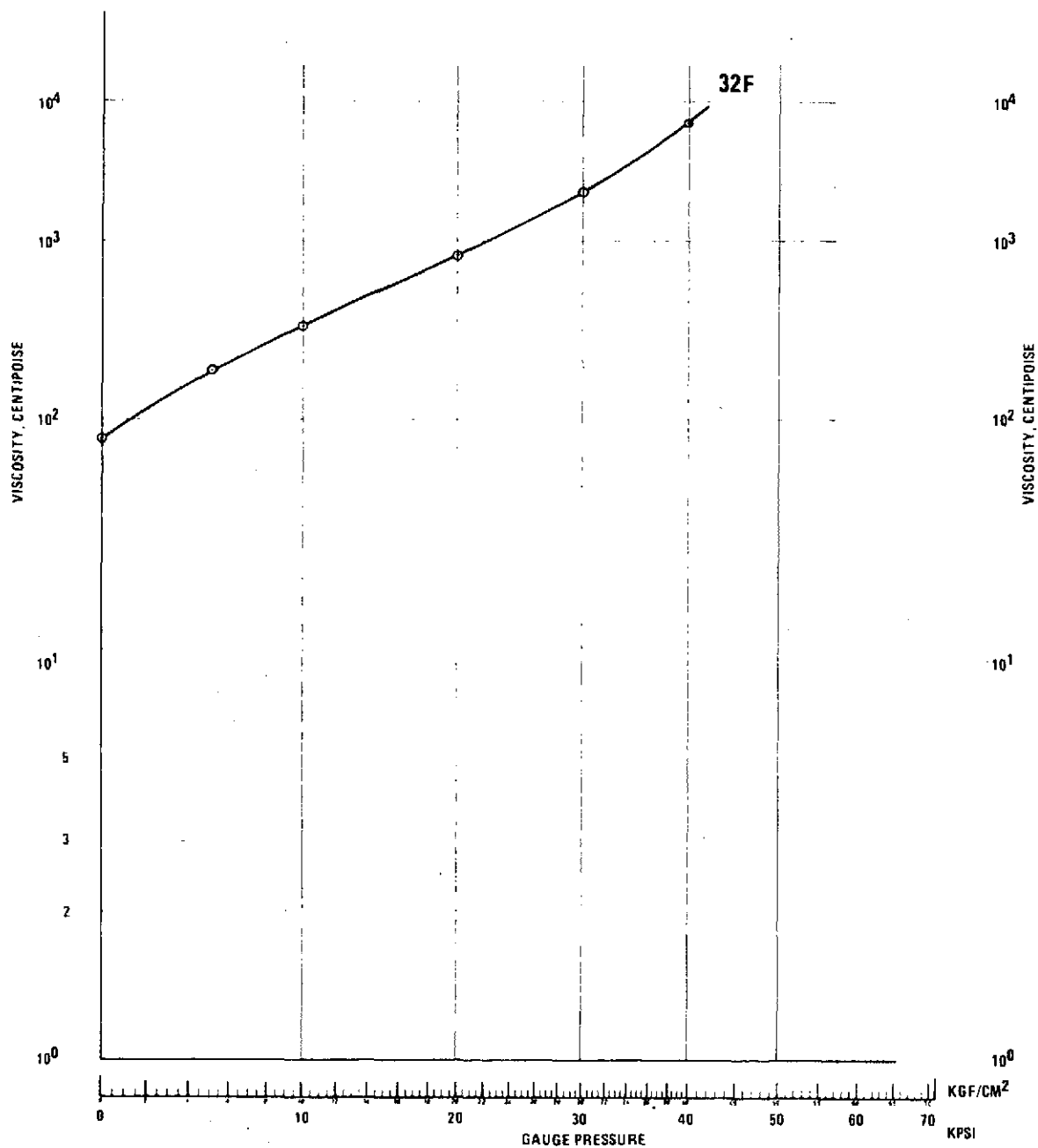
Figure 12 .   Low Shear Pressure Viscosity Characteristic of
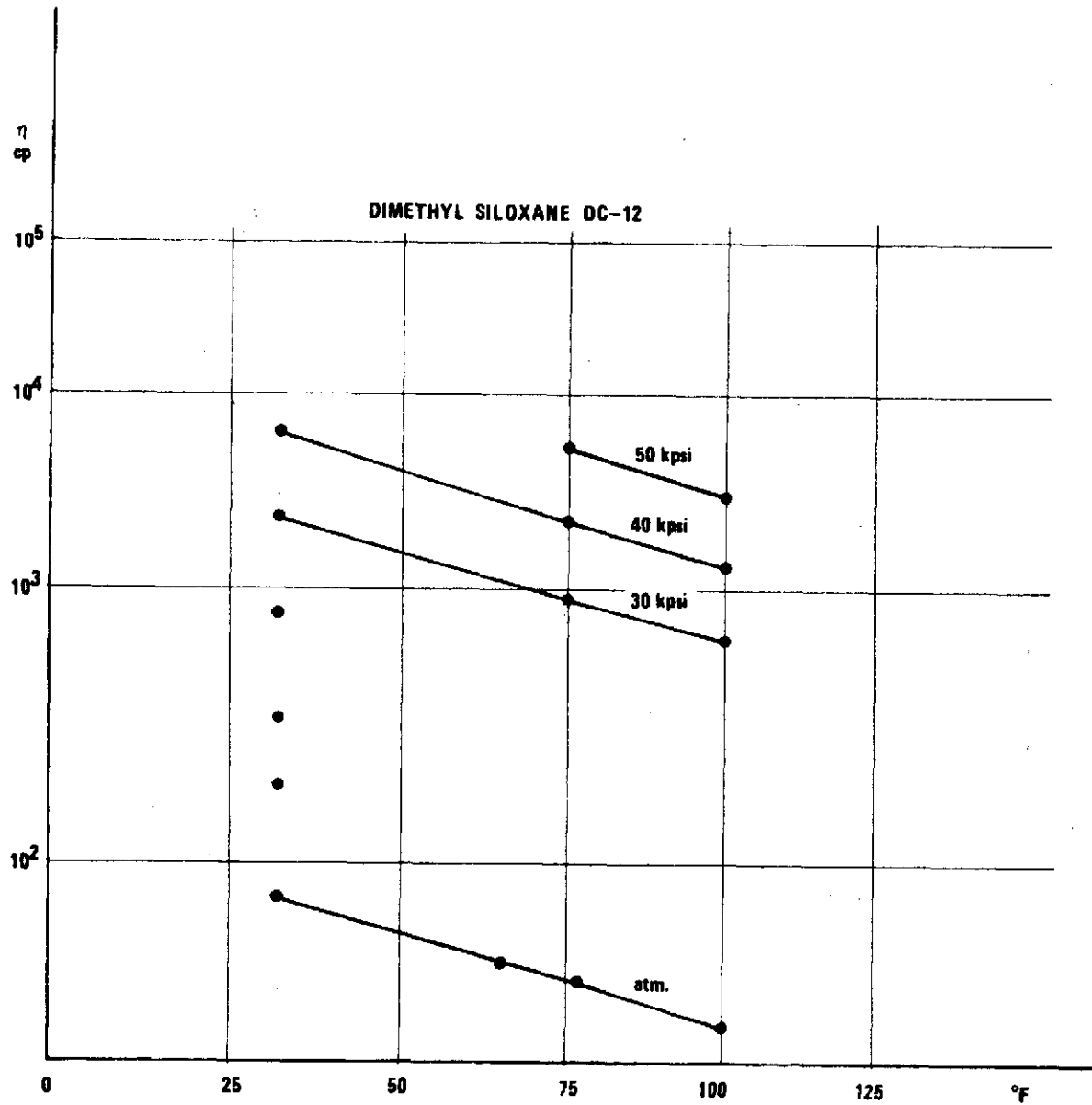Dimethyl Siloxane DC-200-50, 32°F.

Figure 13. Low Shear Temperature Pressure Viscosity Characteristics
of Dimethyl Siloxane DC-200-50 in the Range 32 - 100°F,
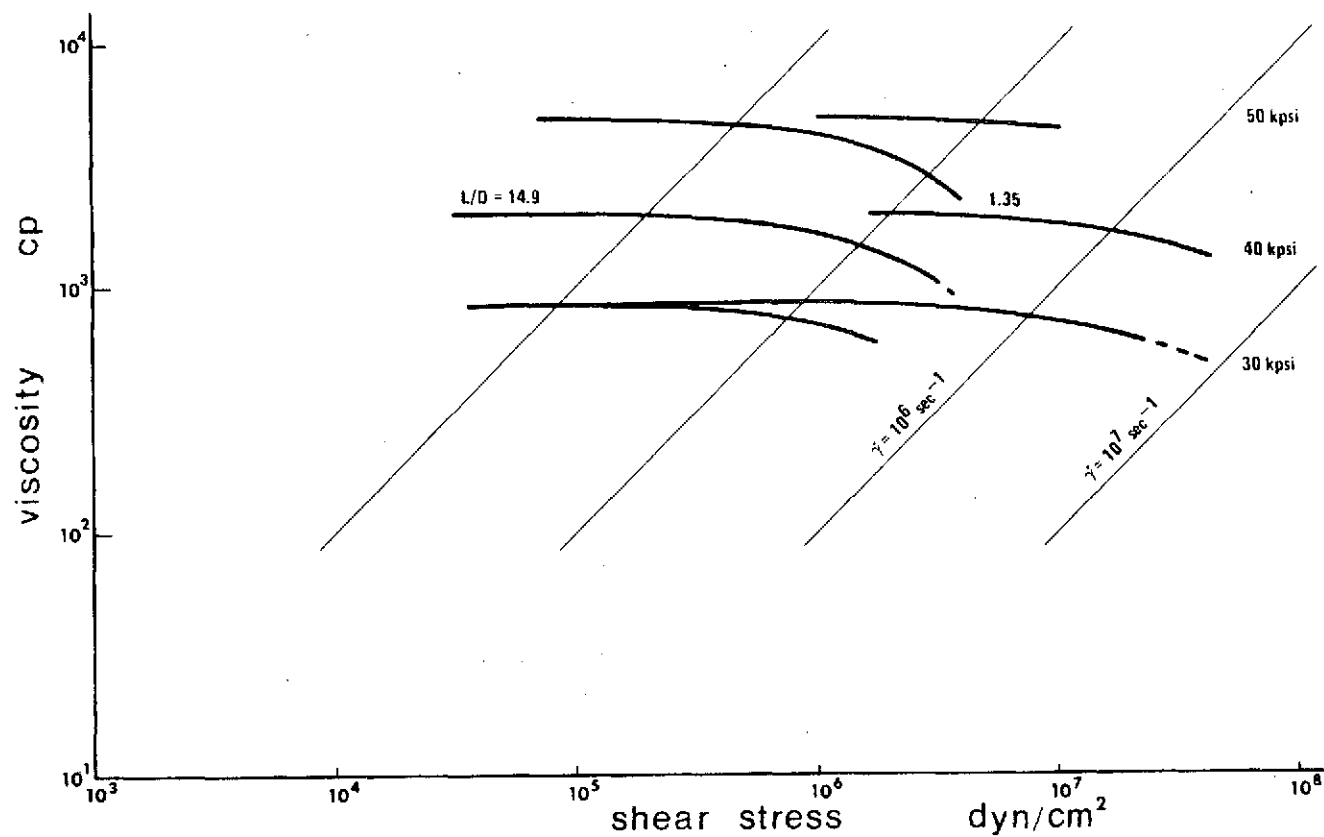(ASTM D 341-43).

viscosity cp

shear stress    dyn/cm²

$10^4$

$10^3$

$10^2$

$10^1$

$10^3$   $10^4$   $10^5$   $10^6$   $10^7$   $10^8$

50 kpsi

40 kpsi

30 kpsi

L/D = 14.9

1.35

$\dot{\gamma} = 10^6\ sec^{-1}$

$\dot{\gamma} = 10^7\ sec^{-1}$

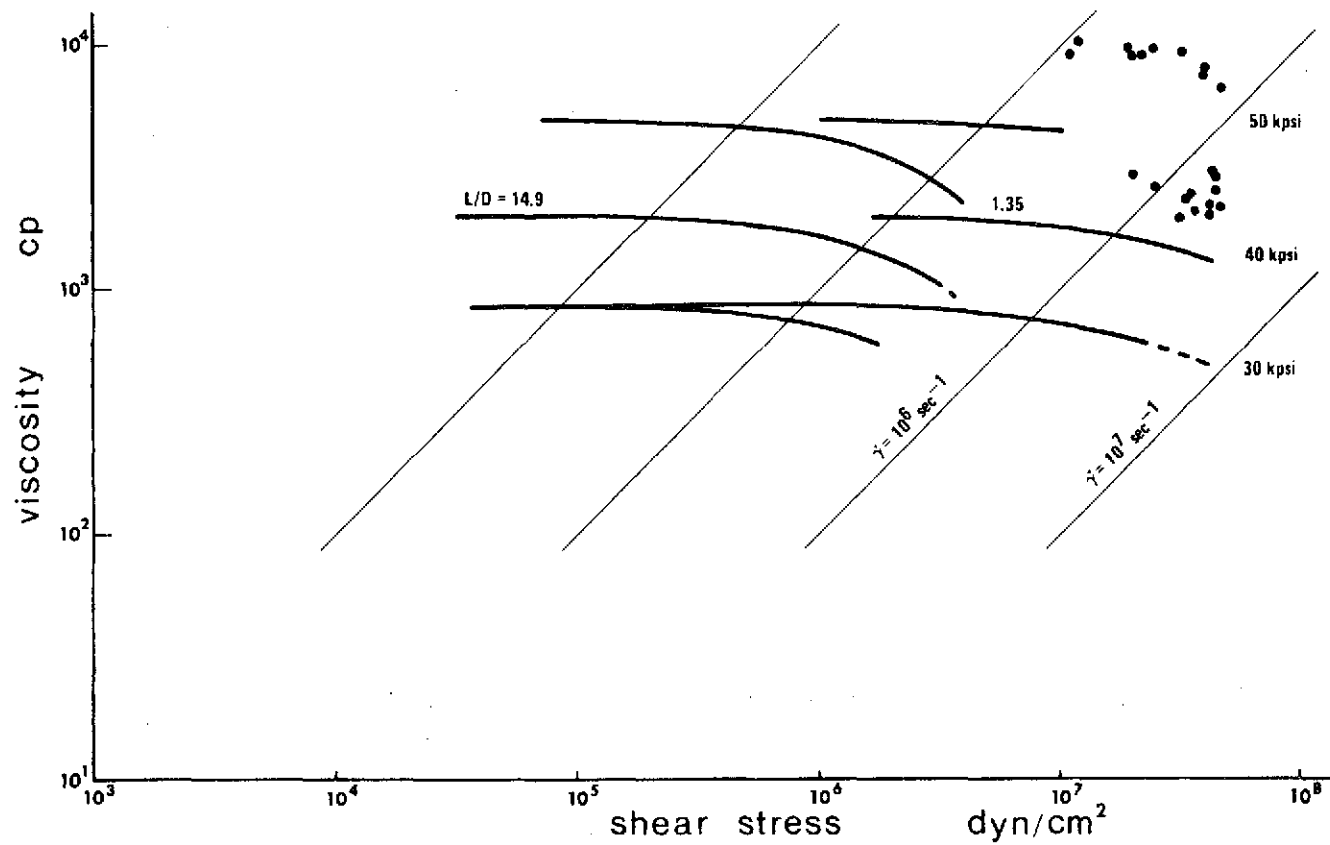Figure 14.   High Shear Measurements of Dimethyl Siloxane DC-200-50,
T = 75°F.

Figure 15. High Shear Measurements with Partially Blocked Capillary. (Dimethyl Siloxane DC-200-50. T = 75°F. The results are plotted with Figure 14 as the background.)

capillary and tubing. The results are plotted with Figure 14

as the background. It is apparent from Figure 15 that the plotted

results are grouped in a meaningless pattern in terms of liquid behavior.

All apparent viscosities are higher than what would be expected for

liquid behavior. These higher values of apparent viscosities possibly

indicate partial solidification of the siloxane.

The results of the first measurements taken follow the previously

measured flow curve for 40 kpsi - 75°F conditions. The applied shear

stress was below $2 \times 10^7$ dyn/cm$^2$ (285 psi). The latter part of the 40

kpsi series yields meaningless results, however. Applied shear stresses

were above $2 \ 10^7$ dyn/cm$^2$. High shear stress measurements were attempted.

at 50 kpsi with capillary O without giving meaningful results. This

explains the missing high shear stress in Figure 14 of the flow curve

for capillary O at 50 kpsi. The sapphire capillary, capillary O, was

taken out and inspected after such experiments. No damage to the sapphire

or its seals was ever observed.

The siloxane was investigated also at 32°F. Figure 16 shows the results.

In order to investigate high shear stress behavior, only capillary O

experiments were performed.

Measurements at 50 kpsi could not be carried out. A partial solid-

ification was observed at 40 kpsi above shear stresses of about

$3 \times 10^6$ dyn/cm$^2$ (43 psi). The siloxane seemed to be in a stable condition

in that lower shear stresses applied after a high stress situation gave

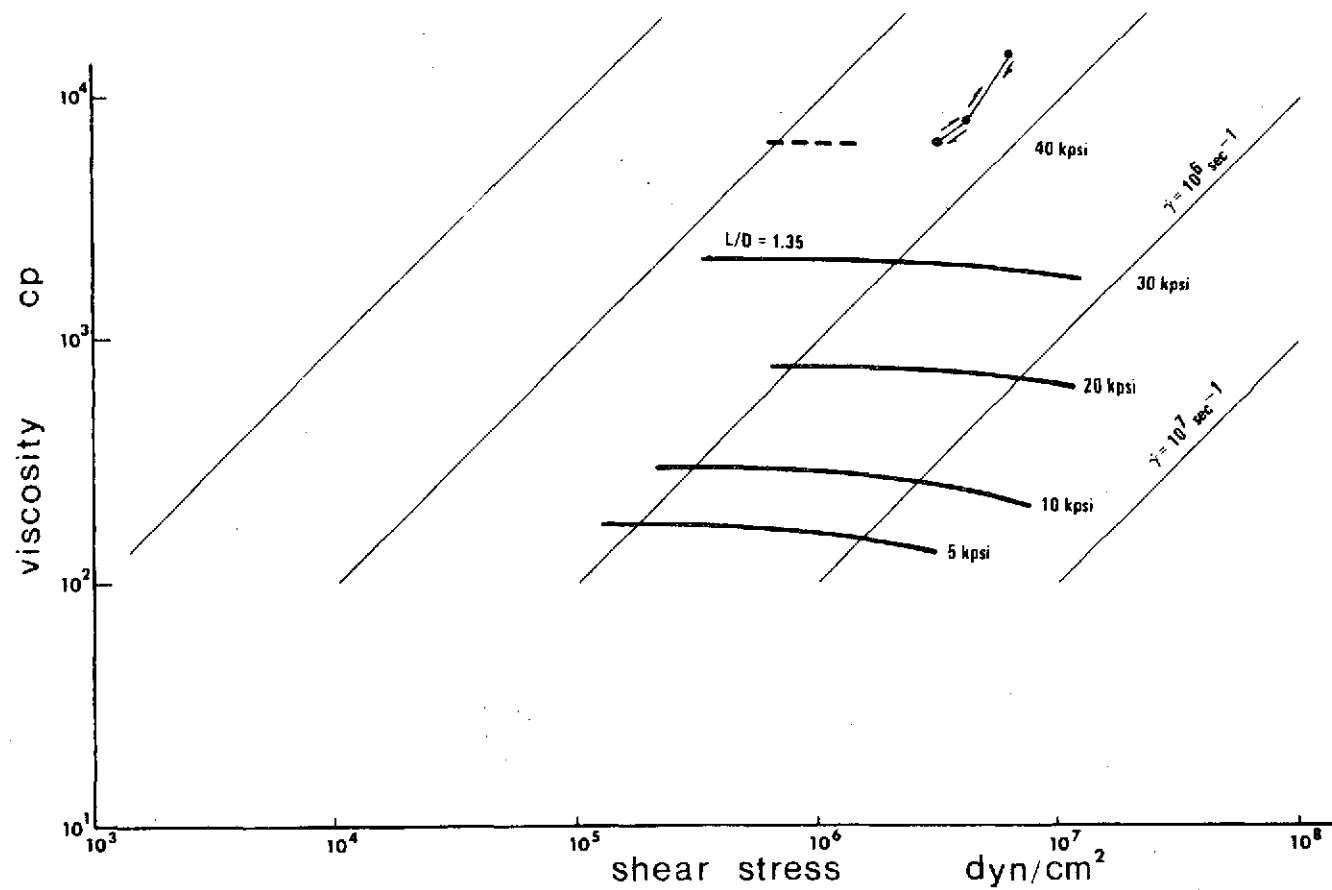results consistant with earlier results within the same series.

Figure 16. Non-Liquid Behavior of Siloxane at 40 kpsi, High Shear Measurements. (Apparent reversible behavior T = 32°F.)

The flow curves for siloxane, at 75°F, show smaller deviation from the Newtonian characteristic than the curves of diester as shown in Figure 8. This is consistant with the dissipation heating hypothesis and expectations based on the significantly smaller Q-factor for siloxane.

The flow curves of Figure 16 at 5 and 10 kpsi show greater deviation from the Newtonian characteristic than previously observed. This greater deviation is consistant with a slightly greater slope (greater Q) in the temperature region 32° – 75° as seen from Figure 13 compared with Figure 11.

The experiment was repeated under identical conditions as the previous measurements, 32°F capillary O only. The results are found in Figure 16. Non-liquid behavior was again observed at 40 kpsi and shear stresses above 3 x 10⁶ dyn/cm². A gradual process toward complete solidification seemed to prevail, however. No definite explanation was found for this slightly altered behavior under otherwise identical conditons.

The siloxane measured at 100°F with capillary 4 in order to establish a connection with low shear stress data previously measured. The results are plotted in Figure 18. The results of capillary 4 measurements were found to be of slightly larger magnitude than expected (see Figure 13 and Figure 11). The reason for this deviation was not pursued further because the discrepancy was considered insignificant for the general conclusions of the work.

Several investigations were performed into the solidification of the siloxane. The more rugged capillary 1 was mounted in the system during these investigations. The temperatures were 75°F and 32°F. Pressure was increased in steps of 10 kpsi with a waiting period of several minutes.
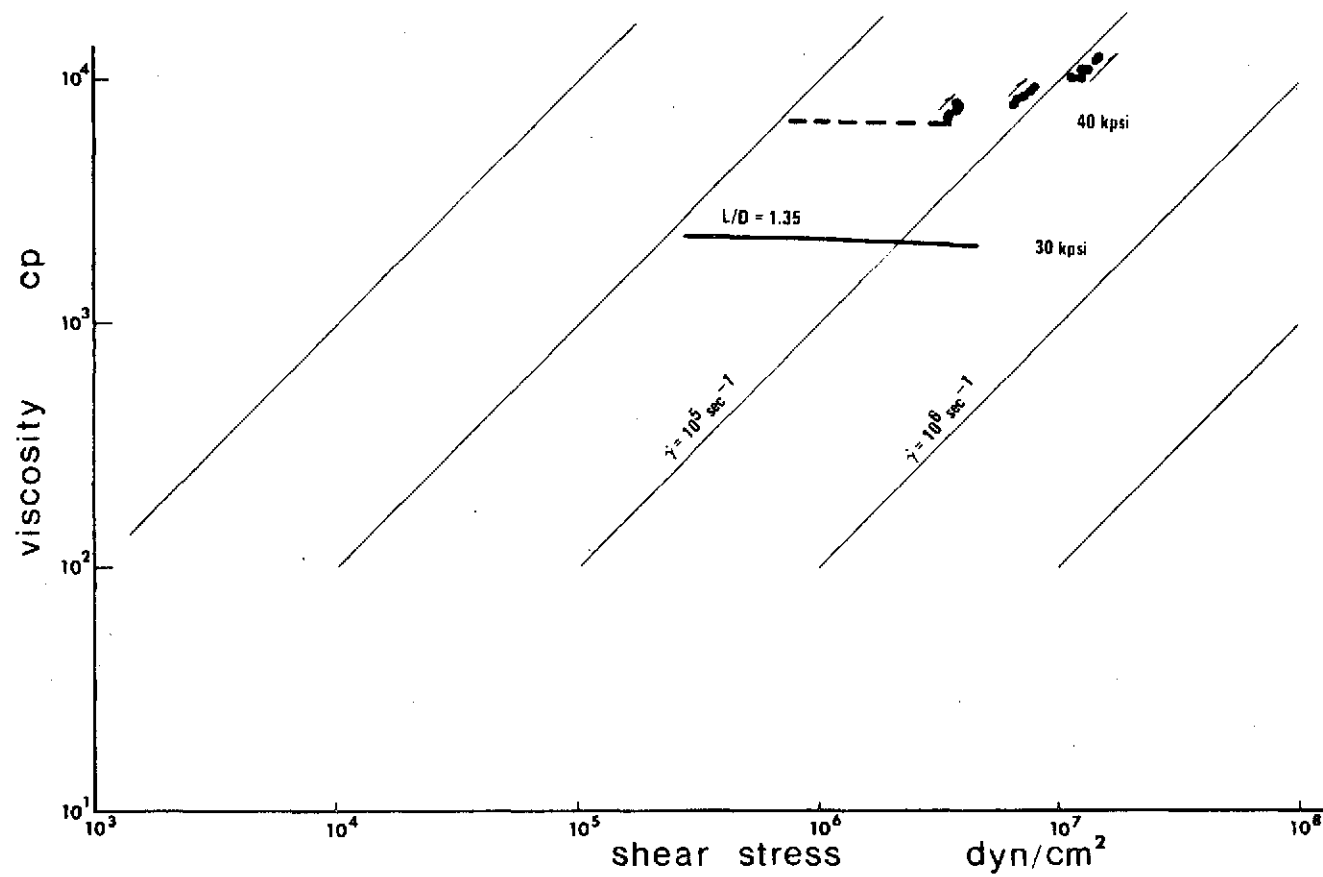
Figure 17. Non—Liquid Behavior of Siloxane at 40 kpsi, High
Shear Measurements. (Apparent irreversible behavior
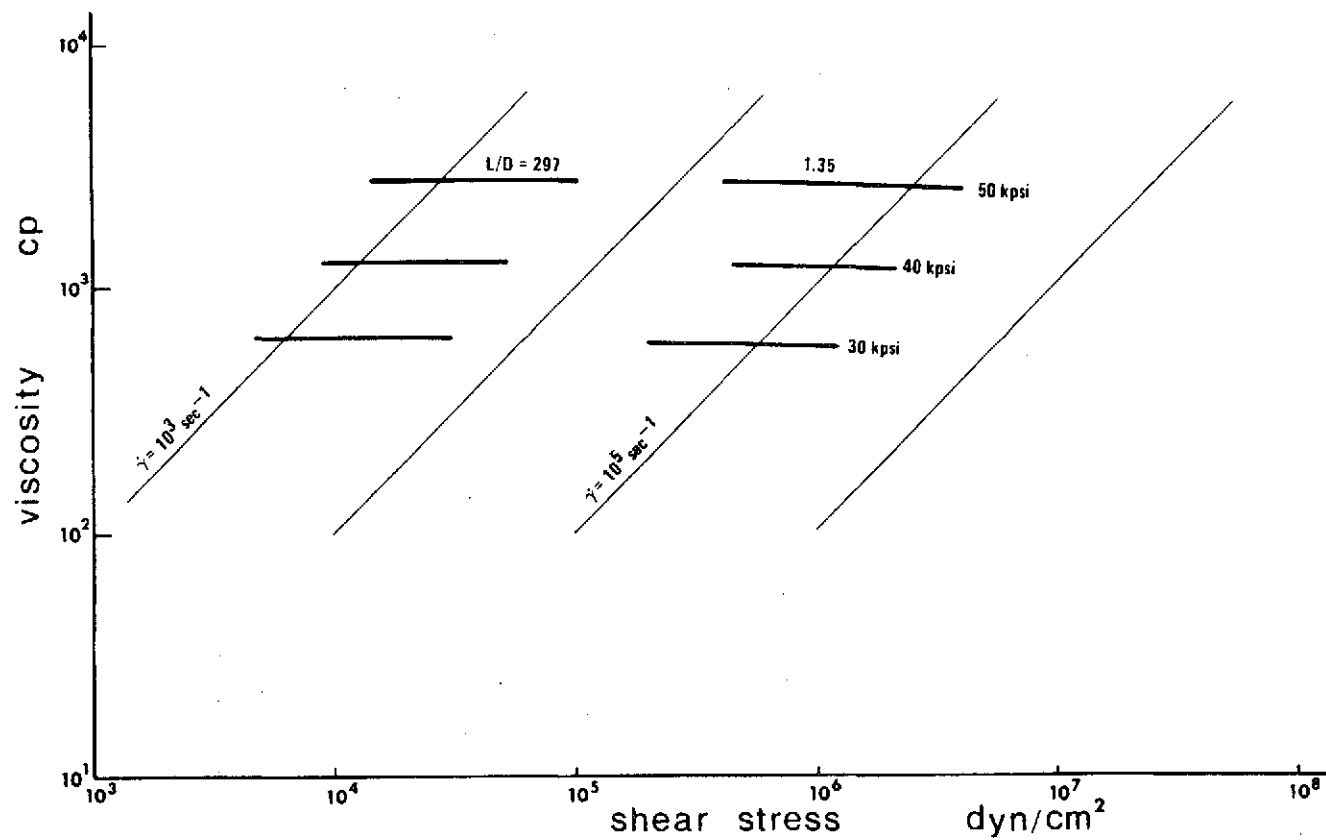T = 32°F.)

43

Figure 18. Low Shear Measurements (Capillary 4) and High Shear Measurements (Capillary 0) for Comparison with Previous Collected Data.

Shear stress shocks were applied at each pressure level to provoke

a possible solidification. Shear stress peaks are estimated to have been

of about 5 x $10^5$ cyn/cm$^2$. Complete blockage of some of the tube branches

of the test systems was observed at 60 kpsi for 75$^\circ$ and at 50 kpsi for 32$^\circ$F.

These observations were reproducible. A large hysteresis in reversal to complete

liquid state was found. A return to the liquid state started first after

the system pressure - in the still liquid branches - was lowered 25 to 35

kpsi below the blockage generating pressure. This return to the liquid

state was accompanied by a slight volume increase observed as a slight pressure

increase in the liquid branches. The observations of blockage pressures and

the solidifications experienced at lower pressures and viscosities seem

to justify a tentative viscosity - shear stress diagram (Figure 19 ) which

predicts ranges where non-liquid behavior can be anticipated. These ob-

servations are interesting and may provide a key to a possible explanation

for the anomalous behavior of some silicone oils in their ability to create

an elastohydrodynamic lubrication film. Figure 19 is plotted with Figure 15

as background.

Polyalkyl Aromatic + Additive (DN 600 + Additive). High shear stress measure-

ments of the synthetic lubricant DN600 + Additive are found in

Figure 20. The flow curves show Newtonian behavior at least up to

3 x $10^6$ dyn/cm$^2$ (435 psi). The general form of the flow curves suggests

that Newtonian behavior persists up to the maximum employed stress of 4.2 x

$10^7$ dyn/cm$^2$ (610 psi). Partially non-liquid behavior was possibly encountered

at 30 kpsi and certainly at 40 kpsi.

The table values of capillary l at 20 kpsi show some scatter around $10^6$

dyn/cm$^2$. These data were taken with a manual traverse of the viscometer.

Difficulties in maintaining steady conditions at very low speed may explain

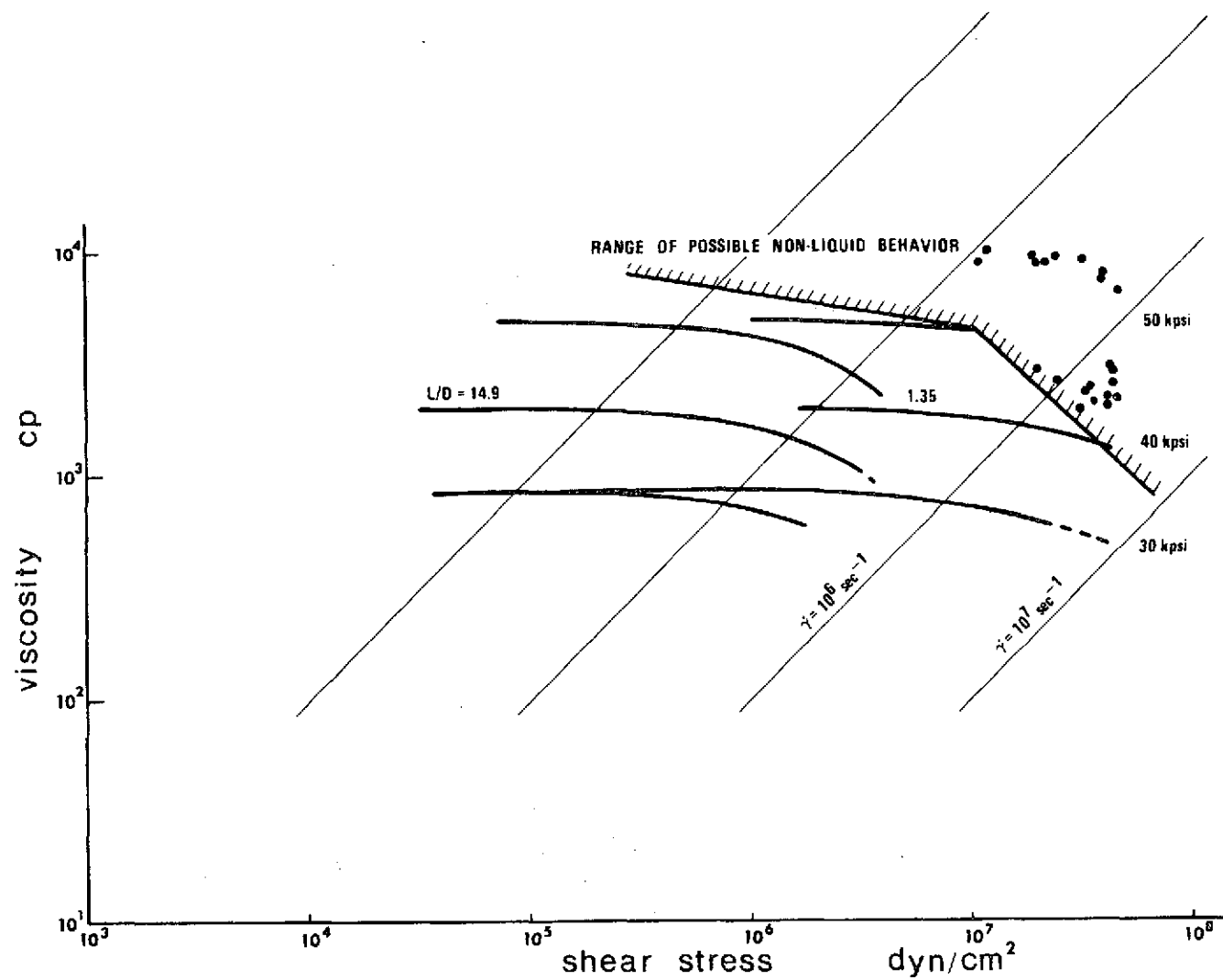the scatter. Some low speed data points created with the constant speed

Figure 19.   Range of Possible Non-liquid Behavior of Siloxane, 75°F.   (This figure is plotted with Figure 15 as the background.)
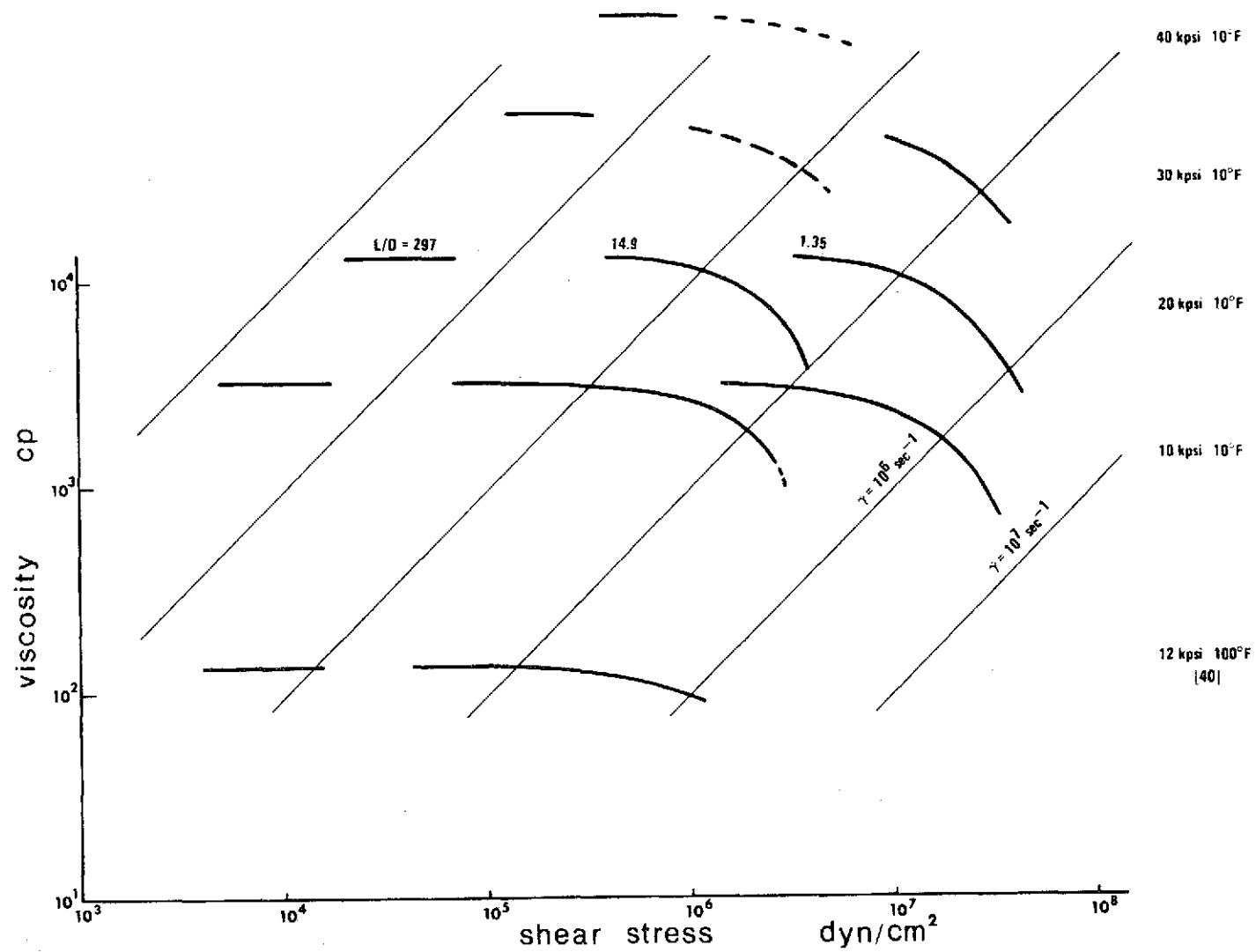
Figure 20. Flow Curves for Polyalkyl Aromatic + Additive (DN 600 + Additive). 10°F and 100°F.

47

drive are found at $3 \times 10^5$, $6.6 \times 10^5$, and $9.6 \times 10^5$ dyn/cm$^2$. Scatter for these groups is very small.

Previous measurements of DN600 + Aditive were carried out up to $1.65 \times 10^5$ cp. Conditions were 100 kspi and 100$^O$F. Non liquid behavior was not experienced, presumably due to the higher temperature. The scatter at $1 - 2 \times 10^5$ cp (40 kpsi, 10$^O$F) can possibly be explained as a partial solid-ification caused by low temperatures but not necessarily due to high shear stress.

Synthetic Paraffinic Oils XRM 109 F4 and XRM 177 F4. The lubricants XRM 109 F4 and XRM 177 F4 are essentially the same, except that XRM 177 F4 is blended with an anti-wear additive. This additive is not expected to cause significant changes in the viscosity of the blend. The base lubricant in XRM 109 F4 and XRM 177 F4 is a synthetic paraffinic oil similar to Fluid D, the synthetic paraffinic oil reported in [ 9 ], [ 10 ] and to fluid XRM 109 reported in [ 11 ].

Figures 21 - 24 along with Tables 7 and 8 show the low shear stress data. Viscosities at atmospheric pressure are equal for the two lubricants. The pressure viscosity relations at 100°F are also very nearly identical. There is a trend for XRM 109 F4 to show slightly higher viscosities than XRM 177 F4 at higher pressures and temperatures. The greatest deviation is found at 50 kpsi and 300°F. XRM 109 F4 has a viscosity which is about 8% higher than the corresponding viscosity of XRM 177 F4.

Figure 25 shows a pressure-viscosity plot of XRM 109 F4, XRM 177 F4 and Fluid D. The figure illustrates the difference between samples which are not from the same lot. The viscosity of Fluid D is consistently lower than the viscosities of the XRM fluids. The figure also shows the slightly increased viscosities for XRM 109 F4 compared with XRM 177 F4. The trend is particularly visible at 300°F. The anti-wear additive reduces the viscosity slightly compared with that of the base fluid.
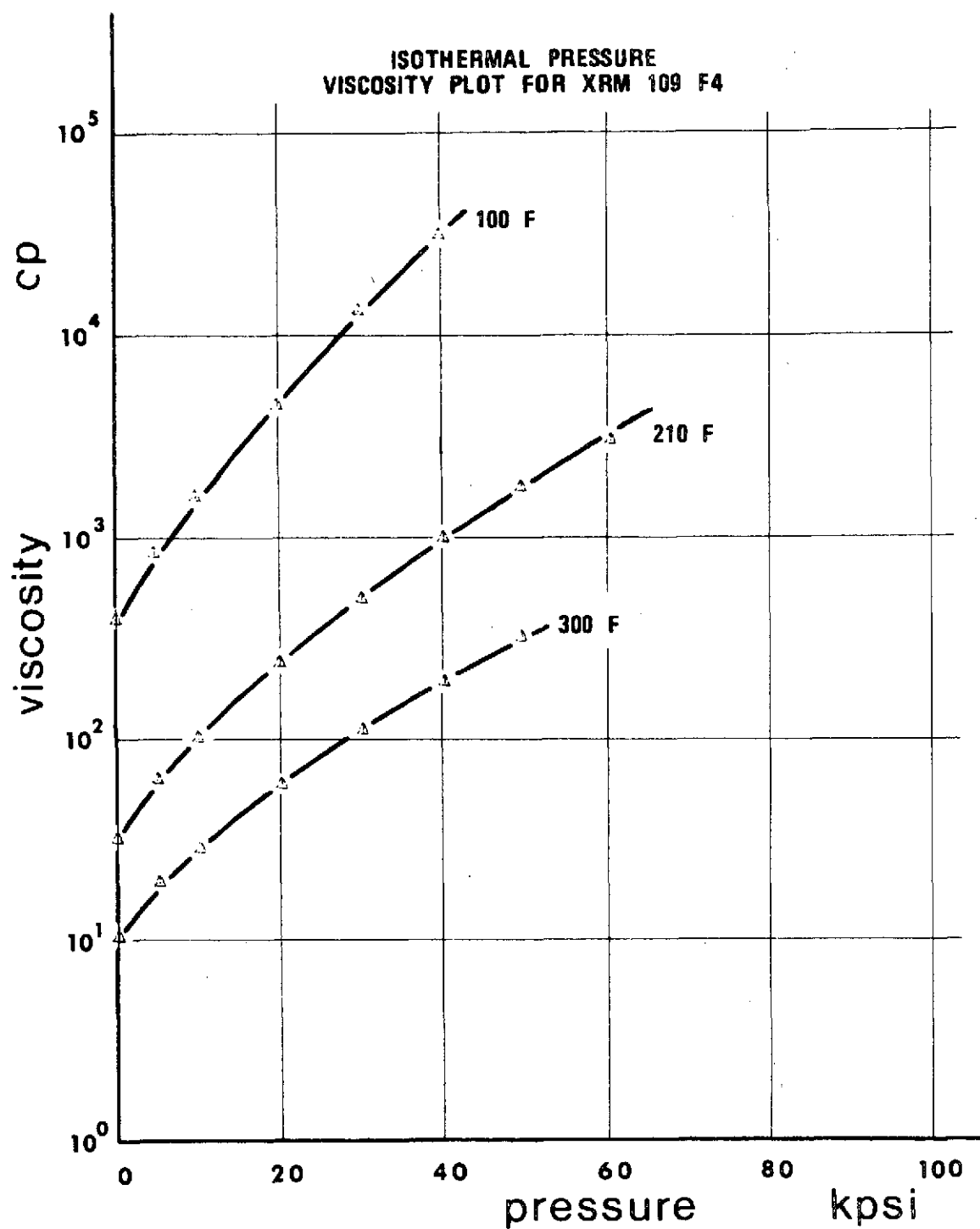
Figure 21. Isothermal Pressure Viscosity Plot for XRM
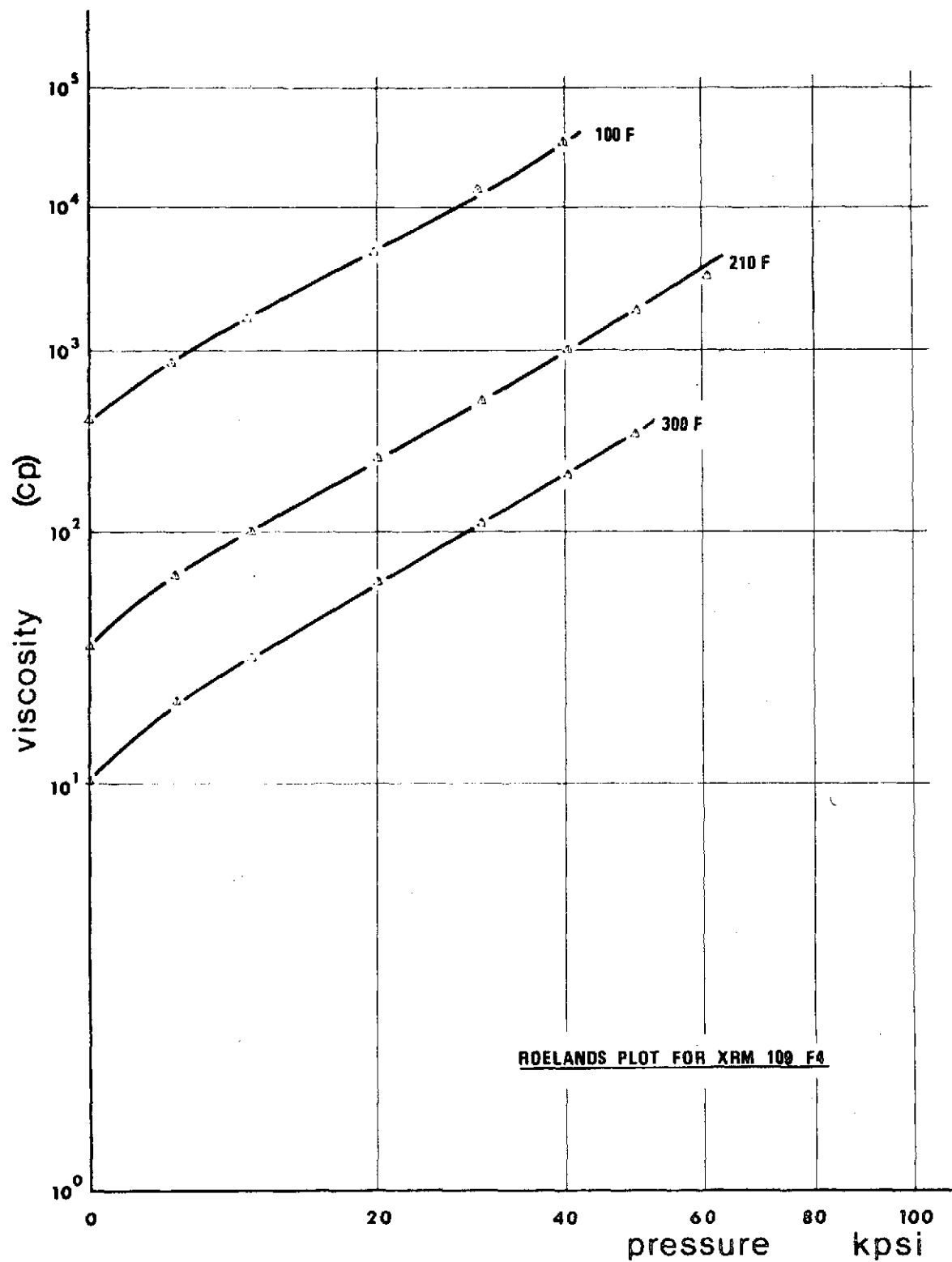109 F4. (Semilog Presentation.)

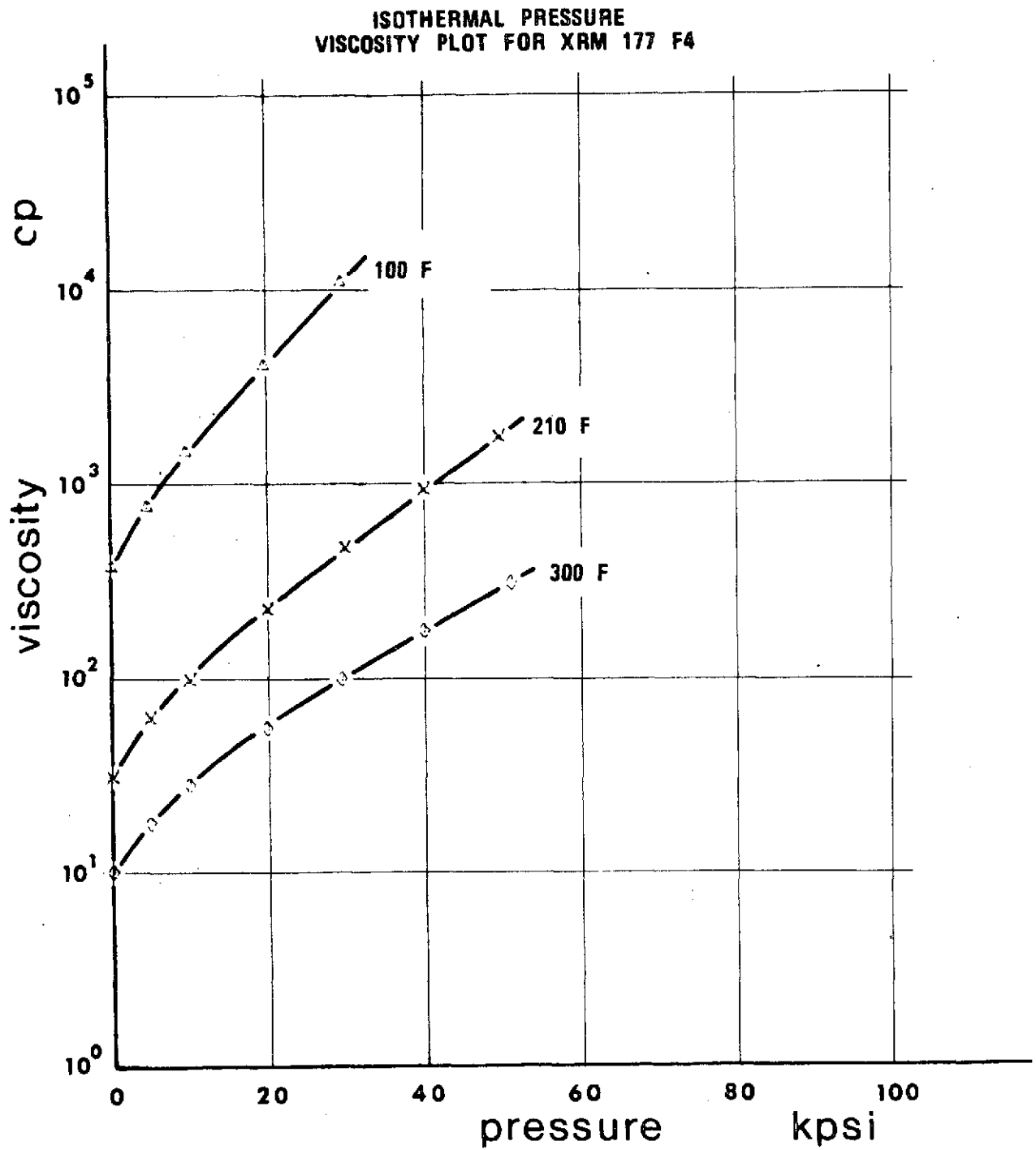Figure 22. Roelands Plot for XRM 109 F4.

Figure 23 .  Isothermal Pressure Viscosity Plot for
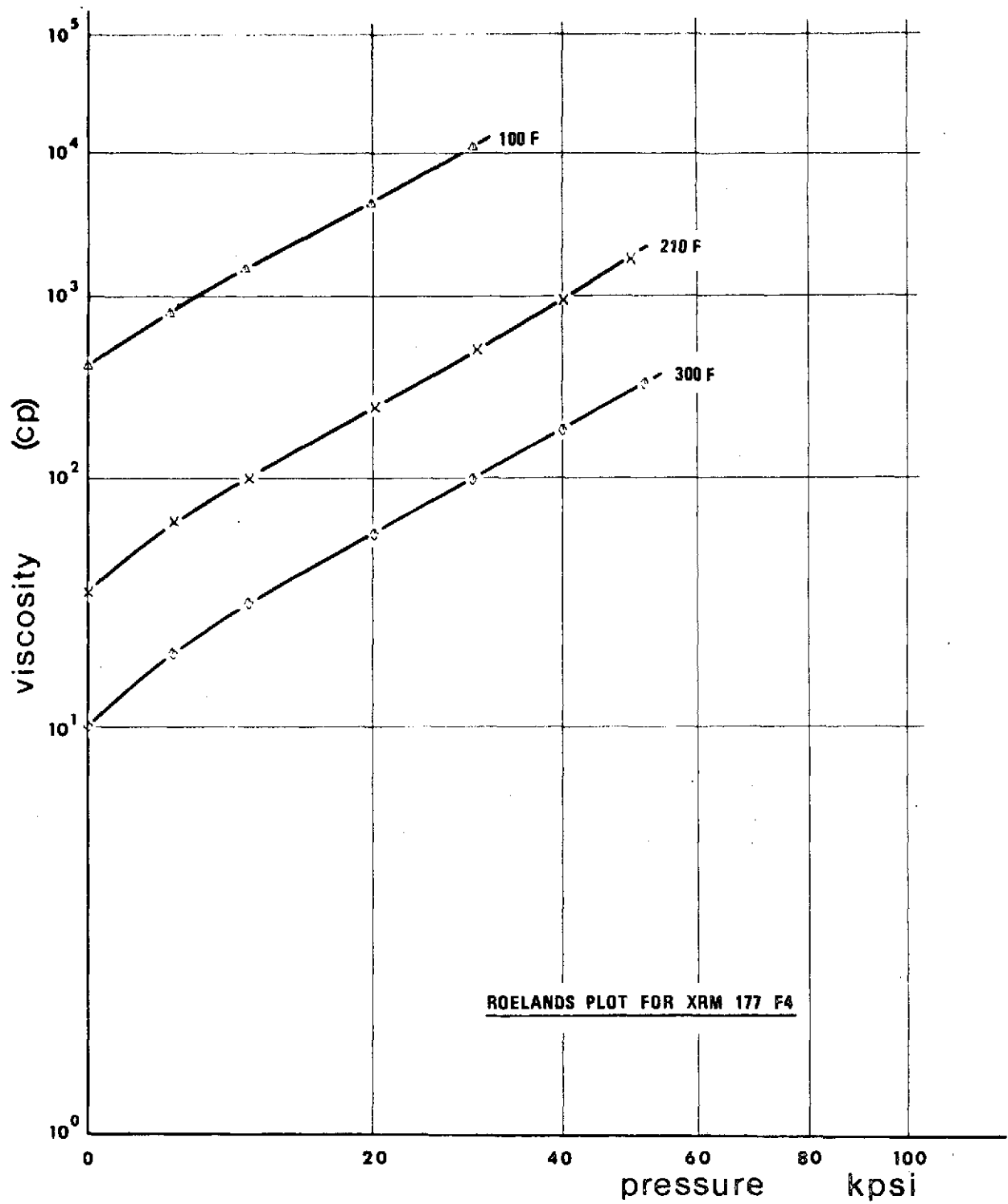XRM 177 F4.  (Semilog Presentation.)

Figure 24 . Roelands Plot for XRM 177 F4.

Table 7    XRM 109 F4, Synthetic Paraffinic Oil,

Plot, L/D = 297

### Averaged Data Points

XR  109 F4  100 F

| P (PSI) | V (cP) |
|---|---|
| .00000 | .37600+03 |
| .47530+04 | .80367+03 |
| .97724+04 | .15267+04 |
| .19794+05 | .43194+04 |
| .29879+05 | .12829+05 |
| .39870+05 | .30525+05 |

XRM 109 F4  210 F

| P (PSI) | V (cP) |
|---|---|
| .00000 | .31600+02 |
| .49462+04 | .62895+02 |
| .99898+04 | .10047+03 |
| .20023+05 | .23623+03 |
| .30184+05 | .49047+03 |
| .40246+05 | .97936+03 |
| .49608+05 | .17384+04 |
| .60497+05 | .29581+04 |

XR 109 F4  300

| P (PSI) | V (cP) |
|---|---|
| .00000 | .16220+02 |
| .50313+04 | .19251+02 |
| .10065+05 | .28248+02 |
| .20112+05 | .58539+02 |
| .30257+05 | .10861+03 |
| .40363+05 | .18823+03 |
| .49687+05 | .31313+03 |

NOT REPRODUCIBLE

Table 8    XRM 177 F4, Synthetic Paraffinic Oil,

Plot, L/D = 297

Averaged Data Points

FLUID XRM 177F4   100°F

| P (PSI) | V (cP) |
|---------|--------|
| .00000 | .37600+03 |
| .47029+04 | .76613+03 |
| .96466+04 | .14697+04 |
| .19651+05 | .41280+04 |
| .29578+05 | .11027+05 |

FLUID XRM 177F4  210 F

| P (PSI) | V (cP) |
|---------|--------|
| .00000 | .31600+02 |
| .49475+04 | .63243+02 |
| .99268+04 | .99644+02 |
| .19991+05 | .22776+03 |
| .30020+05 | .47191+03 |
| .40206+05 | .93740+03 |
| .49704+05 | .17434+04 |

XRM 177 F4   300 F

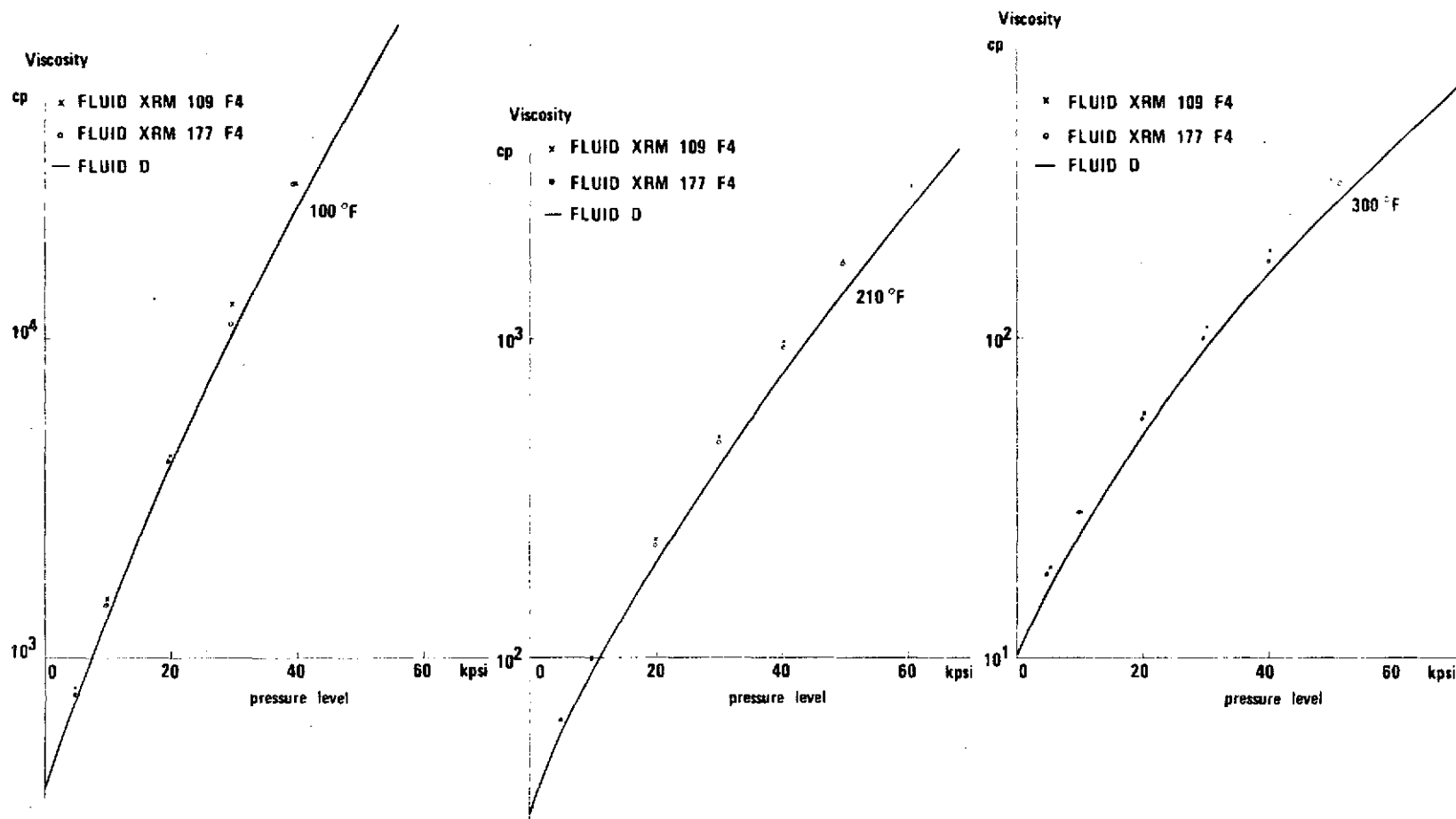| P (PSI) | V (cP) |
|---------|--------|
| .00000 | .12220+02 |
| .48992+04 | .18247+02 |
| .98698+04 | .28595+02 |
| .19905+05 | .55708+02 |
| .29546+05 | .99291+02 |
| .40126+05 | .17470+03 |
| .51372+05 | .30802+03 |

Figure 25.    Isothermal Pressure Viscosity Plot of Fluid D, XRM 109 F4 and XRM 177 F4.    (The effect of the antiwear additive, XRM 109 and XRM 177, and the difference in properties when the fluids are not from the same lot, fluid D and fluids XRM, are shown.)

Figure 26 shows the high shear stress measurements for fluid XRM 177 F4. The two fluids XRM 177 F4 and XRM 109 F4 were found previously during the low shear stress investigation to be very nearly identical. shear stress investigations of XRM 109 F4 would expectedly not yield significant new information and were therefore not carried out.

Some of the flow curves for a capillary cover more than two decades of shear stress. The Newtonian parts of the curves are particularly far extended into the low shear region showing good agreement with measured low shear data. The overlap zone is more than a decade wide. The heating effect of the curves of capillary 1 is distinctly seen. The general form of the flow curves suggests that the apparent non-Newtonian behavior measured with capillary 0 is caused by heating alone. The highest shear stress measured was $4.78 \times 10^7 \mathrm{dyn/cm^2}$ (695 psi).

The operating characteristics for the lubricant in an EHD contact are also shown in Figure 26. The two vertical lines are estimated working conditions for the lubricant at a load of 15 lbf at 55 in/sec sliding speed in a steel ball and sapphire disc contact. The positions in the contact are at the center (the right vertical line) and 1/4 of the contact radius from the entrance (the left vertical line). Figure 26 shows clearly that capillary viscometry is not very far from the situation where EHD conditions for a lubricant can be created in a laboratory experiment in which the parameters of interest can be varied independently of each other.

An investigation of all the reported flow curves of the four lubricants has shown that all characteristics do fit to one general standard curve, regardless of the fluid type and for both capillary 1 and capillary 0 measurements. Deviations from this master curve are of the same magnitude as the experimental error. This observation of generality strongly indicates
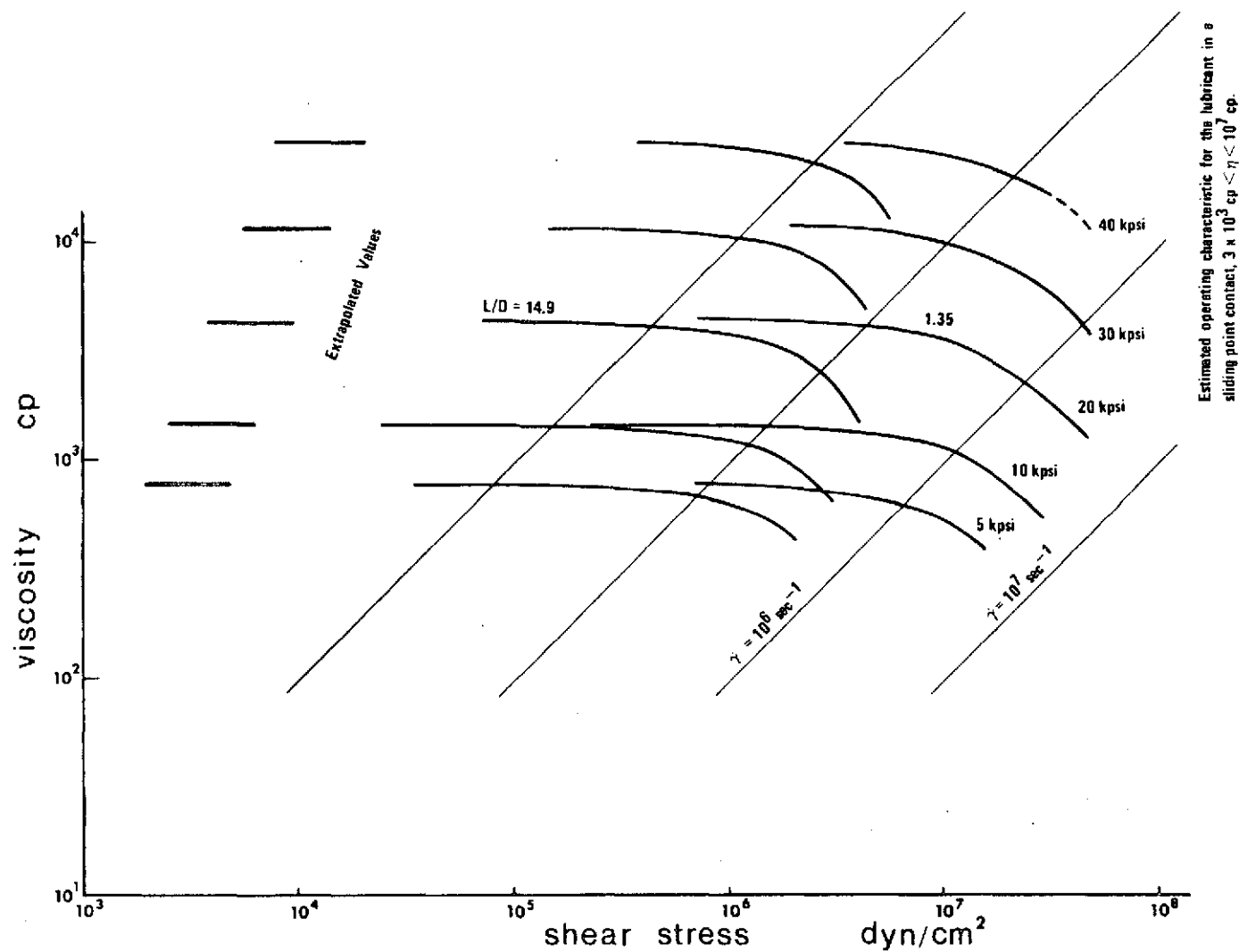
Figure 26. High Shear Measurements of XRM 177 F4, 100°F. (A maximum shear stress of about 700 psi is obtained. The figure shows the operational characteristic for the lubricant in an elastohydrodynamic contact with a maximum Hertzian pressure of 150 kpsi.)

that the same mechanism is responsible for deviation from a Newtonian characteristic. Further work on the hypothesis of dissipation heating is under way, particularly with respect to the influence of the coefficients of temperature-viscosity and heat condition.

B3J: Paraffinic Mineral Oil with 11.5% Polyalkylmethacrylate MW = $.2 \times 10^7$. Polymer blended lubricants have long been used extensively in various engineering fields, particularly the automotive industry. High shear stress investigations of a polymer mixed lubricant are therefore of interest. It was decided to select a high molecular weight polymer in a relatively high concentration with a straight paraffinic mineral base oil for such an investigation.

The base oil as well as mixtures with a lower molecular weight polymer (MW $\sim .56 \times 10^6$) have been investigated before [ 1], however, only up to about $10^6 dyn/cm^2$. The base oil was then found to have completely Newtonian characteristics in the investigated range.

The same base oil (R-620-12) was selected in this investigation. A polymer (Rohm and Haas PL 4523) with considerably greater molecular weight (MW $\sim .2 \times 10^7$) than used before, was used in order to produce extreme properties of the mixture. The polymer was delivered in solution with a paraffinic oil similar to the base oil. A viscosity increase of 20 times the base oil viscosity was desired. The appropriate percentage polymer, 11.5%, was predicted from [1 ] and [8 ]. A blend with this concentration was prepared and mixed vigorously for 48 hours at room temperature. The mixing was carried out by bubbling dry, filtered air through the charge from the bottom of the container.

Data obtained with capillaries 4 and 1 showed a large amount of
scatter. Lack of expected consistancy of the data led to a suspicion of
incomplete mixing. The viscometer was then purged. The remaining blend
was agitated vigorously for another 24 hours at $160^{O}F$. Measurements with
the more thoroughly mixed charge were carried out with all three capillaries
at $100^{O}F$ and at 5, 10 and 20 kpsi. It was found that the extra mixing
operation did not improve the consistancy of the newly collected data.
The results of both experiments are, therefore, considered representative
for the behavior of the mixture. Figure 27 summarizes the tabulated data.

It is seen from the figure that non-liquid response sets in for
a relatively low magnitude of shear stress of about $3 \times 10^5 dyn/cm^2$ (4psi).
A pronounced directional effect is found for capillary 1 measurement at
20 kpsi. Apparent viscosities differ by a factor 2-3 for capillary 0
measurements at 10 kpsi and for the same shear stress or the same shear
rate. The method of generating the data was different, however. The 10
kpsi series at $2 \times 10^6 dyn/cm^2$ was produced with the constant speed unit.
The 10 kpsi data from $7 \times 10^6$ to $3 \times 10^7 dyn/cm^2$ were produced manually.

The data from capillary 4 may be regarded as second Newtonian
viscosities. A pronounced viscosity increase ($\sim 30\%$) occurs for increasing
shear stresses before apparent non-liquid response sets in at about $3 \times 10^5$
$dyn/cm^2$. Such viscosity increases as well as the non-liquid behavior were
not observed in previous measurements [1] in the same shear stress range.
The concentration of polymer and the molecular weight were, however, signifi-
cantly lower.

Figure 28 and 29 and Table 9 show the pressure-temperature-viscosity
relations at shear stresses believed to correspond to the second Newtonian

Table 9    B3J:  Paraffinic Mineral Oil R-620-12 + 11.5
per cent Polyalkylmethacrylate PL 4523
(MW = .2 + 07), Plot, L/D = 297

FL B3J 75 F

| P (PSI) | V (CP) |
|---------|--------|
| .00000 | .10000+04 |
| .47541+04 | .40188+04 |
| .96455+04 | .19952+05 |

FL B3J 100 F

| P (PSI) | V (CP) |
|---------|--------|
| .00000 | .42000+03 |
| .47652+04 | .10053+04 |
| .97187+04 | .22384+04 |
| .19797+05 | .94024+04 |

FL B3J 150 F

| P (PSI) | V (CP) |
|---------|--------|
| .00000 | .15500+03 |
| .47369+04 | .29473+03 |
| .96952+04 | .51290+03 |
| .19735+05 | .13066+04 |
| .29838+05 | .35385+04 |

FL B3J 190 F

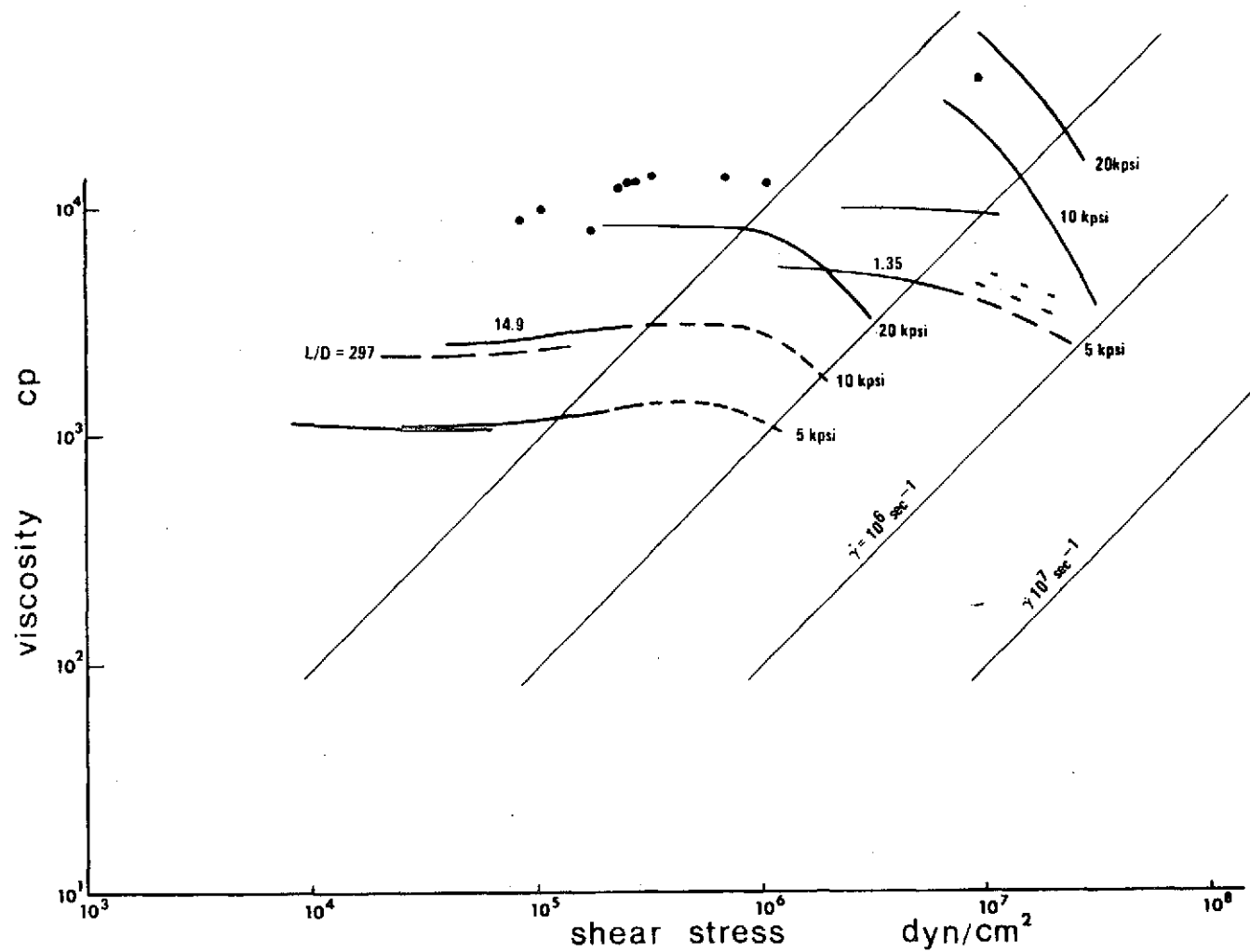| P (PSI) | V (CP) |
|---------|--------|
| .00000 | .10000+03 |
| .47804+04 | .17128+03 |
| .97525+04 | .27204+03 |
| .19772+05 | .58191+03 |
| .29778+05 | .13774+04 |
| .39625+05 | .28990+04 |

Figure 27. High Shear Measurements of Fluid B3J. (Paraffinic mineral oil with 11.5 per cent polyalkylmethacrylate (MW = 2 x 10^6).)

viscosities. The temperature-pressure-viscosity characteristics plotted on an ASTM D 341-43 chart show a pronounced curvature. Viscosities at atmospheric pressure (in Table 10) are estimated from an ASTM type rectifying chart. The viscosities at atmospheric pressure were measured with a Cannon Fenske Routine Glass Viscometer No. 400. The applied shear stress is about 60 $dyn/cm^2$ for $\rho \sim 0.85$, whereas the lowest shear stresses reported in Table 9 are approximately $10^4$ $dyn/cm^2$. The measured viscosities at the very low level of shear stress were about 2.5 times greater than the viscosities at $10^4 dyn/cm^2$. Table 10 summarizes these viscosities at atmospheric pressure. The tabular values are believed to represent the first Newtonian state (column 1) and the second Newtonian viscosity level (column 2).

Fluid B3J shows the expected flow curve characterized by a first Newtonian viscosity $\eta_1$ at low shear stress ($\sim 10^2 dyn/cm^2$) and a second Newtonian viscosity $\eta_2$ at a shear stress of about $10^4 dyn/cm^2$. The ratio $\eta_1$ / $\eta_2$ is approximately 2.5. The second Newtonian viscosity $\eta_2$ never approaches the viscosity $\eta_b$ of the base liquid. The ratio $\eta_2$ / $\eta_b$ is of the order of 10. The second Newtonian viscosity level does not significantly exceed $10^4 dyn/cm^2$. The apparent viscosity increases with increasing shear stress in the range $10^4 - 10^5 dyn/cm^2$. The increase in viscosity amounts to about 30%. Distinct non-liquid behavior appears shortly above $10^5 dyn/cm^2$ (1.4 psi) and continues to the highest shear stress $\sim 3.5 \times 10^7$ $dyn/cm^2$ (500 psi). It is significant that non-liquid behavior sets in at stresses (1.4 psi) which are more than $10^3$ times smaller than the average shear stress in a moderately loaded elastohydrodynamic point or line contact. These shear stresses ( 1.4 psi), where transition to non-liquid
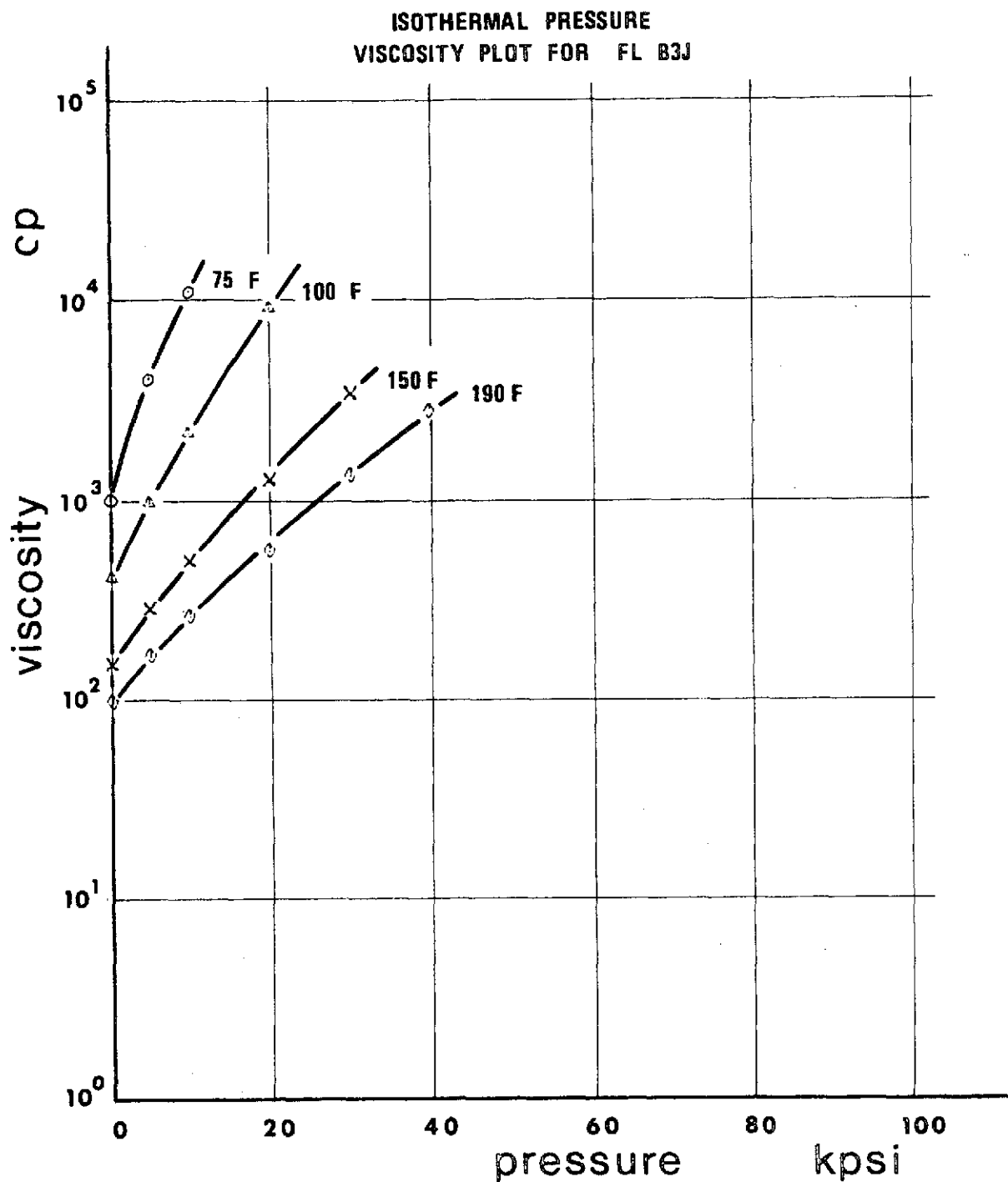
Figure 28. Isothermal Pressure Viscosity Plot for Fluid B3J.
(Paraffinic mineral oil with 11.5 per cent polyalkyl-
methacrylate (MW = 2 x $10^6$). Measurements with
capillary 4. Semilog presentation.)
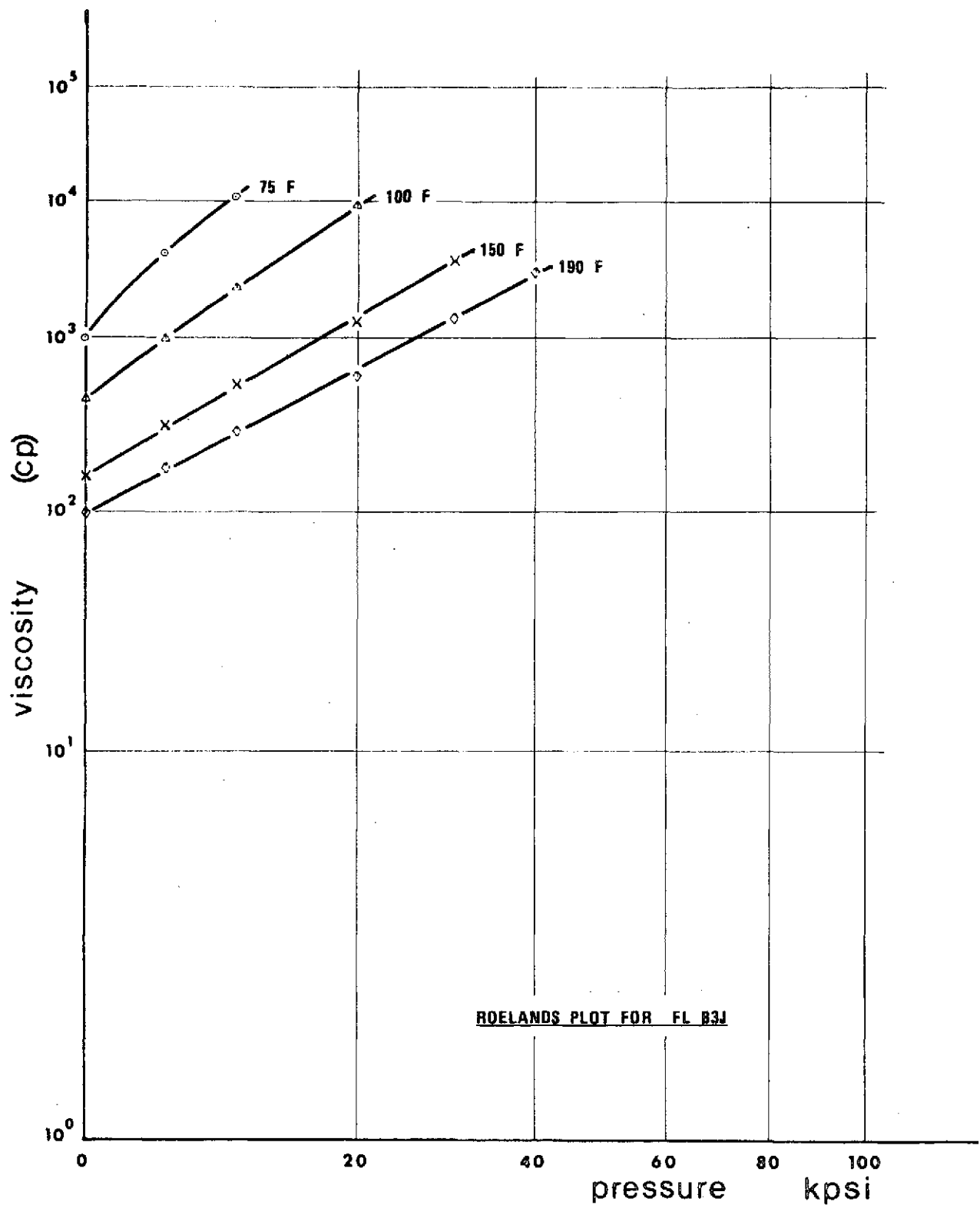
Figure 29. Roelands Plot for Fluid B3J. (Paraffinic mineral
oil with 11.5 per cent polyalkylmethacrylate
(MW = 2 x $10^6$). Measurements with Capillary 4.)

Table 10

Paraffinic Mineral Oil with 11.5% Polyalkylmethacrylate
$MW = .2 \times 10^7$. Viscosities at Atmospheric Pressure.

|  | 1 | 2 |
|---|---|---|
|  | $\simeq 60$ dyn/cm$^2$ | $10^4 - 10^5$ dyn/cm$^2$ |
|  | Capillary No 400 | Cap 4 + Cap 1 * |
| 75 °F | – | 1000 cp |
| 100 °F | 1010 cp | 420 cp |
| 150 °F | 384 cp | 155 cp |
| 190 °F | 221 cp | 100 cp |

*   Table values are estimated from extrapolated
    characteristics on ASTM D 341 – 43
    type charts.

behavior appears for the material B3J, are found far into the inlet zone of an elastohydrodynamic contact. At this location, the pressures are low, film thicknesses are many times the centerline film thickness and temperatures are very nearly equal to ambient temperatures.

b. Revised Pressure Viscosity Coefficients

In last year's progress report a complete set of pressure-viscosity data on all the fluids investigated for NASA was presented. Included were pressure-viscosity coefficients for each fluid. Both $\alpha_{OT}$ and $\alpha^*$ were presented where

$$\alpha_{OT} \equiv \frac{d\ln\mu}{dp}\bigg|_{T,P=0} \quad ; \quad \alpha^* \equiv \left[\mu_0 \int_0^\infty \frac{dp}{\mu(p)}\right]^{-1}$$

These were computer processed for the viscosity-pressure data. As is to be expected, the value of $\alpha^*$ should be more reliable because it involves the integration of experimental data over the entire range of data obtained. However, the values of $\alpha_{OT}$ are obtained by the differentiation of experimental data at one end of the range of the data, which inherently introduces the possibility of significant errors. Further, it was found after last year's progress report was submitted that the algorithm employed in calculating the values of $\alpha_{OT}$ introduced additional errors in the values of $\alpha_{OT}$ when the viscosity or viscosity-pressure coefficient were in certain ranges.

Therefore, the values of $\alpha_{OT}$ were recalculated by plotting the data and obtaining the slope of the log viscosity-pressure isotherm at atmospheric pressure by the best visual fit to the data. The revised data are presented in Table 11 and Figure 30 and replace Table 1 (p.25) and Figure 5 (p.28) respectively in the last year's progress report. To the best of our knowledge, the other data presented in that report are correct.

Table 11 . Revised Table 1 – PRESSURE VISCOSITY CHARACTERISTICS[1] – $\alpha_{oT}$ – of 1972 Progress Report

$$\alpha_{oT} \text{ X } 10^4 \text{ (psi)}^{-1}$$

| Fluids | 100°F | 210°F | 300°F | 75°F[2] |
|---|---|---|---|---|
| Advanced Ester | 1.05 | 0.95* | 0.92* | 1.08 |
| Formulated Advanced Ester | 1.27 | 1.02* | 0.84* | 1.32* |
| Naphthenic Mineral Oil Plus Additive | 1.84* | 1.48* | 1.25* | 1.95* |
| Synthetic Paraffinic Oil Plus Additive | 1.40* | 1.25* | 1.02* | 1.44* |
| DN-600 Plus Additive | 1.42 | 1.25* | 1.03* | 1.43 |
| DN-600 | 1.40* | 1.20* | 1.00* | 1.43 |
| FN-2961 | 2.12 | 1.25 | 0.92* | 2.53 |
| MCS-418 | 1.00* | 0.63* | 0.51* | 1.18* |
| MCS-460 | 2.17 | 0.94 | 1.03 | 3.00 |
| Krytox | 3.07* | 3.02 | 3.00* | 3.08* |
| XRM-109 | 1.40* | 1.53* | 0.97 | 1.25 |

1) To obtain the pressure viscosity coefficient in $[N/m^2]^{-1}$, divide the entry by $6.894 \times 10^3$.
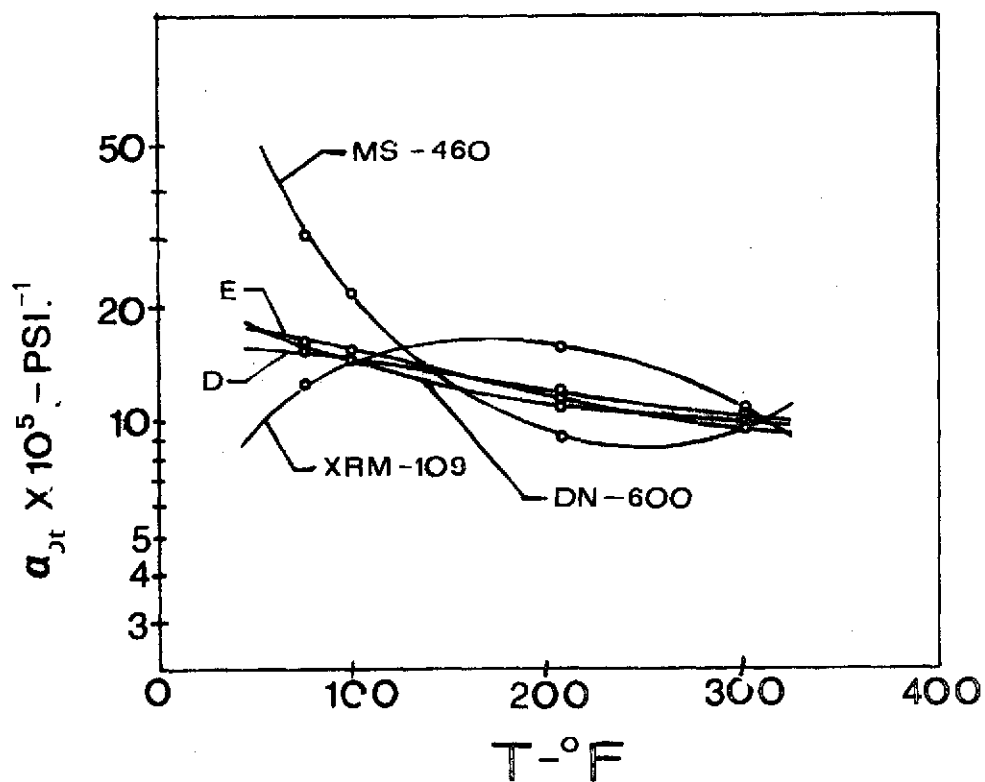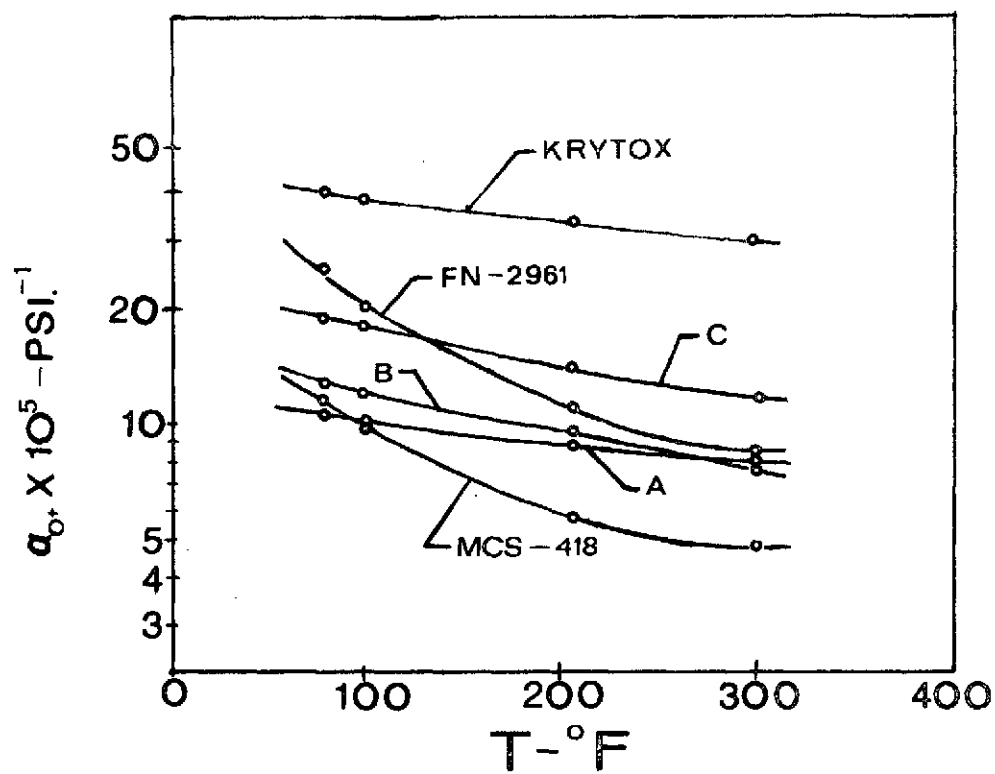2) Extrapolated data from Figure 6.

* numbers that have been changed.

Figure 30 - Revised Figure 6. (1972 Report) - Viscosity-Pressure Characteriistic $\sigma_{oT}$ as a Function of Temperature (0 - measures, ■ - extrapolated).

III.  ELASTOHYDRODYNAMIC LUBRICATION INVESTIGATIONS

a.  EHD Pressure Measurement Investigations

A study was conducted to determine the feasibility of a technique to measure the pressure profile in a sliding EHD point contact.  The pressure measurement technique employed a transducer consisting of a 9.0 x $10^{-5}$ m (.0035 in.) diameter piston attached to a cantilever load cell and allowed to move in a 9.0 x $10^{-5}$ diameter orifice in the sapphire bearing plate.

The equipment (Figure 31) that was used is basically the same as that used in previous EHD investigations ( 12,13). The spherical bearing surface is a steel ball of 3.18 x $10^{-2}$ m (1.25 in) diameter.  The sphere is rotated through a flexible coupling cemented to its surface.  The sphere is supported and loaded against the bearing sapphire by three radial ball bearings and located in a lubricated bath.  A significant amount of inertia was incorporated into the drive mechanism in order to maintain a nearly constant sliding velocity between the spherical bearing and sapphire.

The upper surface of the contact is a synthetic sapphire disc having one of its plane surfaces directed toward the contact.  The sapphire bearing used to determine the pressure distribution has dimensions as shown in Figure 32 .

The needle, designed to slide as a piston in the orifice of the sapphire, was processed from a steel rod whose end was ground in the sapphire orifice.  A diamond polishing compound with a particle size of 0.25 micron was used for grinding.  The length of the needle in the sapphire was ground to 2.504 x $10^{-4}$ m (0.010 in) and to a corresponding diameter of 9.0 x $10^{-5}$ m (0.0035 in) (Figure 33).  The needle was cemented to a holder rigidly attached to a micrometer screw mounted in the cantilever
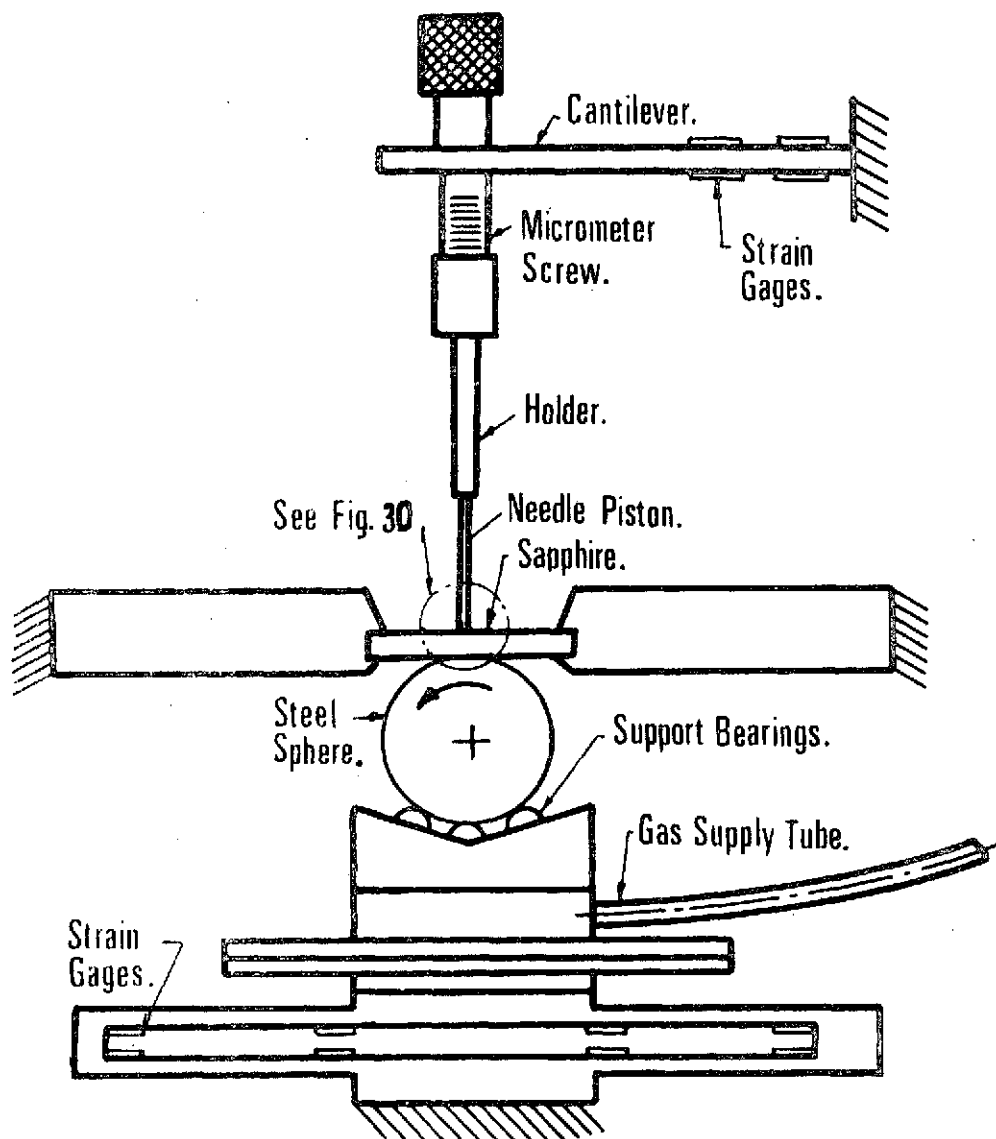
**Figure 31.** Schematic Diagram of the Experimental Apparatus for Pressure Measurement.
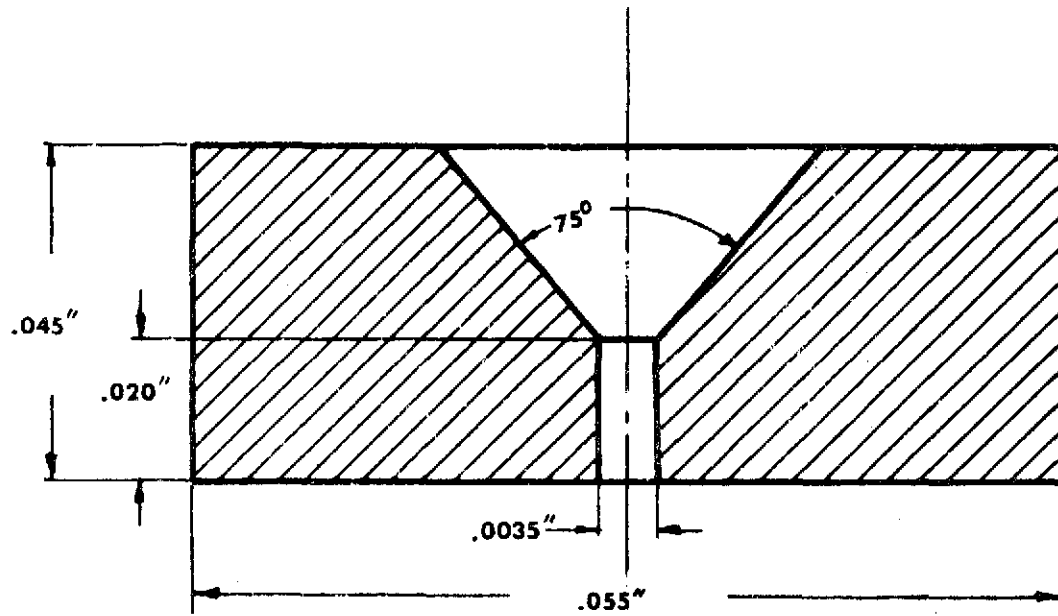
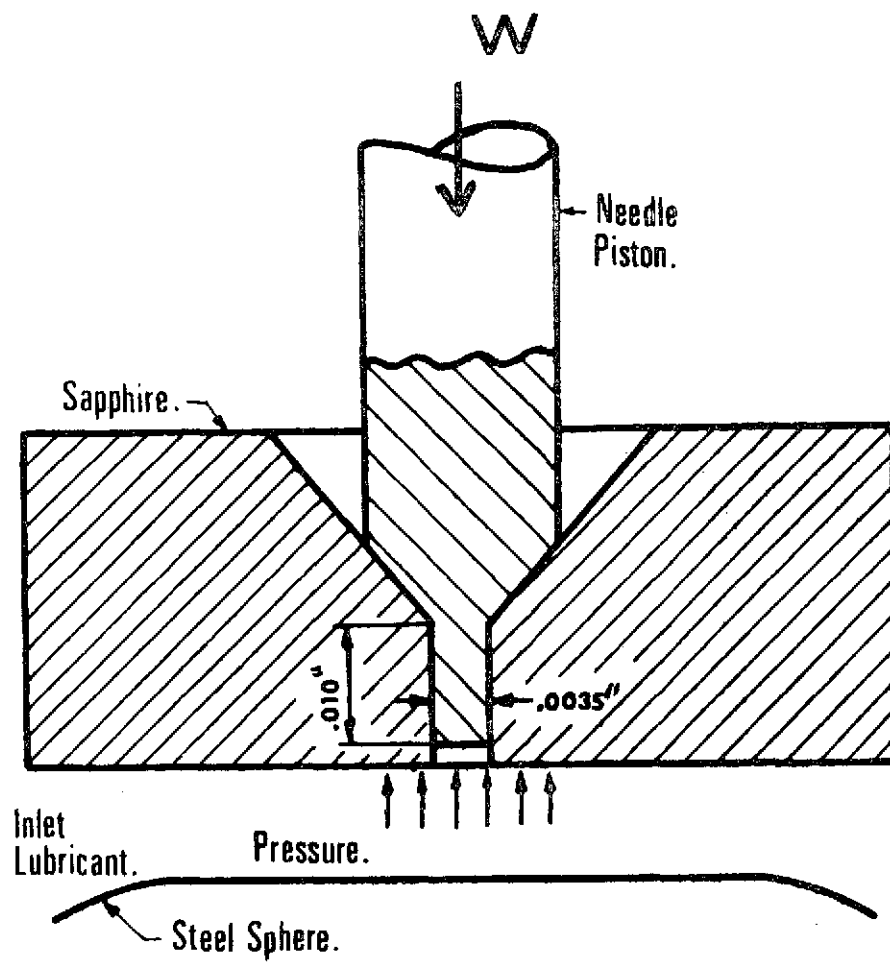Figure 32. Geometry of the Bearing Sapphire.

Figure 33. Detail of the Needle - Sapphire Assembly.

beam (Figure 31).

Four silicon semi-conductor strain gages were cemented on the cantilever beam. The strain gages were connected in a four gage bridge circuit. The sensitivity of this transducer was determined to be 0.072 mV/kpsi. The deflection of the cantilever beam is approximately 0.001 in/lbf.

A pneumatic system has been used to apply the normal load of 15 lbf (150,000 psi Hertz) between the bearing surfaces. The normal force load cell was calibrated statically by placing known weights on the sapphire support. A linear response up to 30 lbf normal load was obtained.

The transducer was calibrated in a separate mounting as shown in Figure 34 . Lubricant oil at a known pressure was fed into the fitting. The pressure acting on the end of the needle resulted in a normal force on the needle causing a deflection of the cantilever load cell. The output voltage (see Figure 35 ) was plotted against each value of pressure $0 - 0.69 \times 10^9$ N/m$^2$ (0 - 100 kpsi). During the calibration experiment no leakage of lubricant from the system was observed.

The location of the orifice in the sapphire bearing relative to the elastohydrodynamic contact was observed through a Leitz metallurgical microscope. The upper plate of the apparatus in which is mounted the sapphire bearing offers a two direction freedom of movement by means of micrometer screws in each direction.

Many attempts were made to record an output signal from the transducer while passing the sapphire orifice through the elastohydroydnamic contact. None of them was successful. However, an immediate explanation of failure to record pressure could not be determined because the conditions
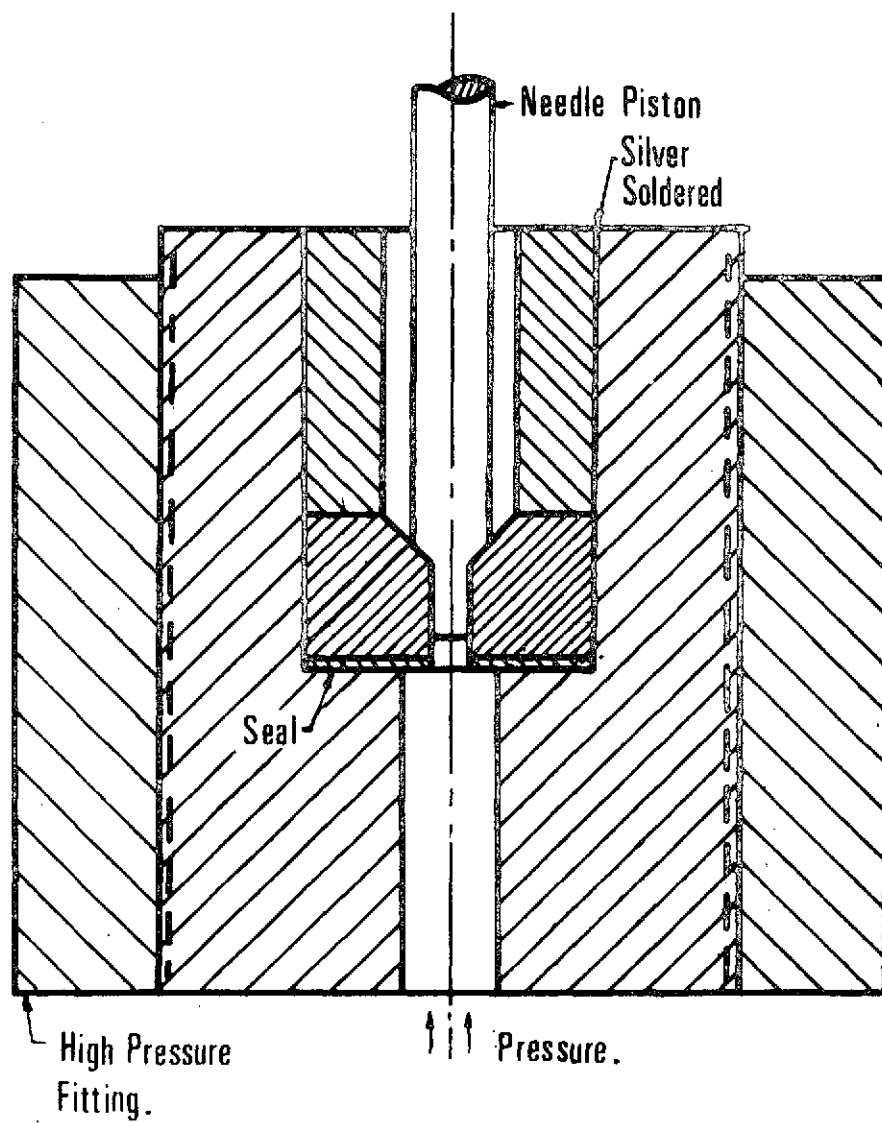
Figure 34. Needle - Sapphire Assembly Used for
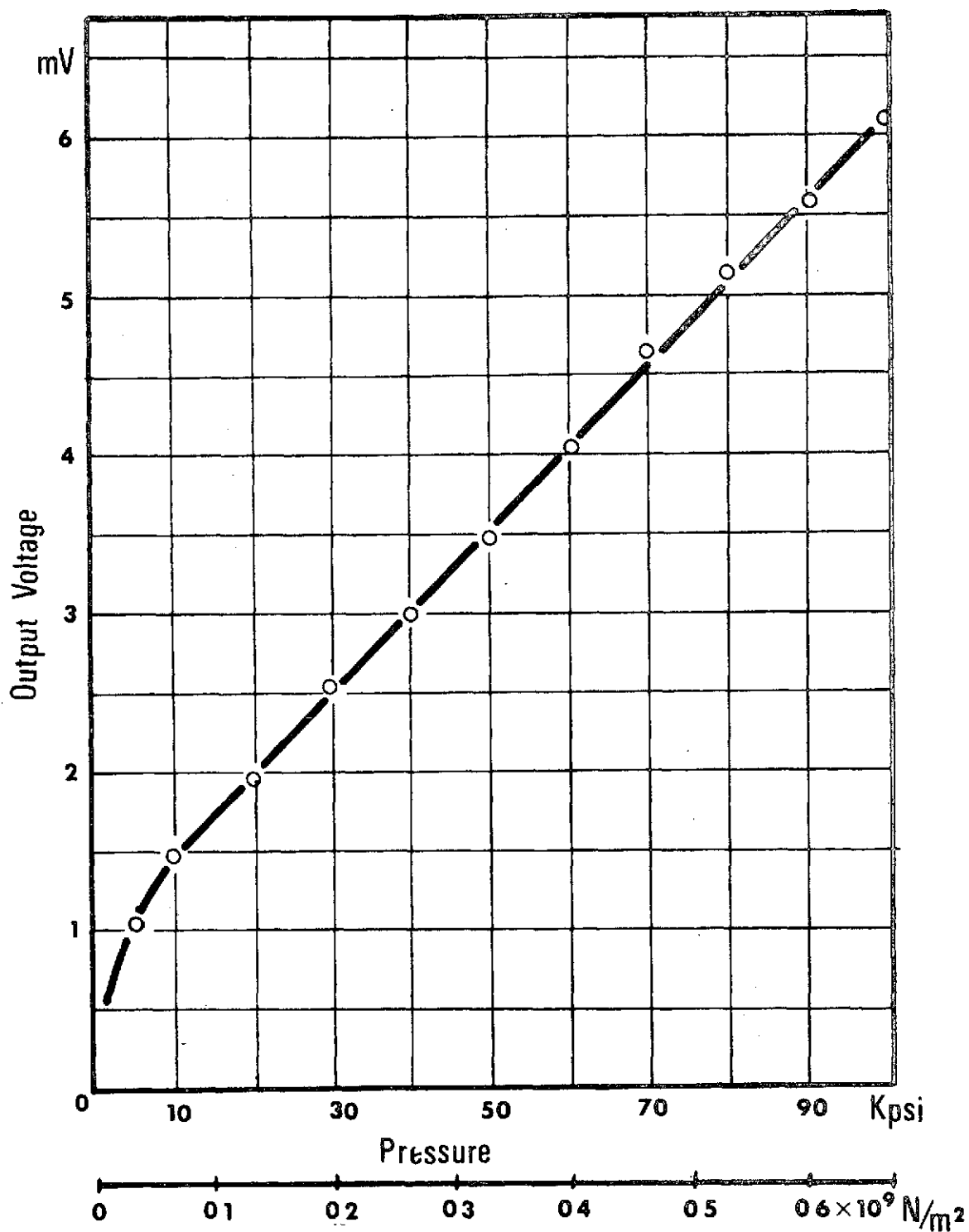Pressure Calibration.

Figure  35, Calibration Curve for the Pressure
Transducer.

during the successful calibration appeared to be similar to those of the elastohydrodynamic contact.

During repeated experiments, a leakage of the lubricant oil between the needle and the wall of the orifice in sapphire bearing was observed. This leakage was not noticed during the calibration experiment. The radial clearance between the needle and orifice remained the same as during calibration at a value $\geq 0.25$ micron ($10^{-5}$ in) due to the particle size of the diamond compound used to grind the piston portion of the needle. The hydrocarbon oil used during the experiment has a viscosity of 100 cp at a pressure of $0.69 \times 10^8$ N/m$^2$ (10 kpsi). Under these conditions the leakage flow rate would be $3.5 \times 10^{-5}$ in$^3$/sec, for an isothermal annular flow with pressure dependent viscosity. The fluid flow rate in the elastohydrodynamic contact passing by the orifice is only $3.0 \times 10^{-6}$ in$^3$/sec, however, at a sliding speed of approximately 50 in/sec. As the pressure builds the viscosity increases and, therefore, at very high pressures the leakage flow rate will decrease with increasing pressure. This was the case during the calibration where the fluid flow rate available was very large compared to the leakage flow rate.

Because the annular leakage flow rate is greater than the flow rate of the fluid entering the EHD contact, the pressure will never build up to levels where the viscosity reaches values where the leakage can be neglected as an important factor in pressure measurement.

An additional difficulty in the elastohydrodynamic contact is the elevated temperature which causes the viscosity to be low compared to conditions during high pressure calibration.

The technique presented in this chapter to determine a pressure profile across the elastohydrodynamic contact was found not to be feasible. It has also been determined that more accurate machining of the needle-

sapphire assembly will not make the technique feasible. The clearance between the needle and orifice is already very small and significantly smaller clearances would be difficult to produce.

A technique employing two sapphires is under consideration at this time. One sapphire would have a small orifice and a conical opening as shown in Figure 32. A second sapphire having a manganin strain gage evaporated on its surface would be mounted above the first with the manganin gage positioned over the conical hole. This method combines two of the most widely used techniques in experimental research to determine the pressure distribution; the orifice technique and that of evaporated manganin strain gage. This method appears to solve the difficulties which were encountered in each of the separate techniques. The leakage flow rate from the piston – orifice technique would be eliminated by not using a piston and the manganin strain gages would no longer be exposed directly to the severe stress conditions of the elastohydrodynamic contact. The orifice in the sapphire could further be enlarged at its upper exit to allow the use of a coil strain gage rather than an evaporated one.

The orifice adjacent to the contact could be made much smaller than that used previously since a mating piston would not be required. The reduction in orifice diameter would increase the pressure measurement resolution.

b. EHD Temperature Measurements.

A technique has been developed for obtaining a map of the steel ball surface temperature and the lubricant temperature averaged across the film in an EHD contact. The temperature measurement system consists of an infrared micro-detector used to collect infrared radiant energy

from the elastohydrodynamic contact and, thereby, allowing the deduction of the local temperature. The problem of separating the infrared radiation contributions from the ball, lubricant film and sapphire bearing plate has been solved by collecting the infrared radiation under three different conditions, two of them using steel spheres with different emissivities and one using a filter consisting of a calibrated fluid sample "cell" placed between the infrared detector and sapphire bearing plate.

Because the surfaces used for the EHD contact are steel and sapphire, the pressures in the contact are in the range of current design practice. The maximum Hertz pressure is $1.034 \times 10^9$ N/m$^2$ (150,000 psi) for the data reported. These data are for a sliding contact. For a given set of conditions the ball surface temperature reaches a maximum of 115°C and the average fluid temperature reaches a maximum of 360°C, both occurring near the side lobes. The experiment was performed at room temperature with sliding velocities of 1.39 m/sec (54.9 ips).

The sliding EHD point contact is formed using a $3.18 \times 10^{-2}$ m (1.25 in) diameter steel ball rotating and loaded against a $1.52 \times 10^{-3}$ m (0.060 in) thick sapphire flat. The system has been used previously in extensive investigations of film thickness [12], traction [13] and pressure measurement as mentioned in section IIIa.

It is shown in Figure 36, that the pressure transducer has been replaced by an infrared radiometric detector (Barnes Engineering Company, Model RM-2A). The purpose of this detector is to measure the infrared radiation emitted from the contact and, therefore, allow the contact temperatures to be deduced.

The radiometric detector has been equipped with a 15X reflecting objective which allows a spot size resolution of $3.56 \times 10^{-5}$ m (0.0014 in.).
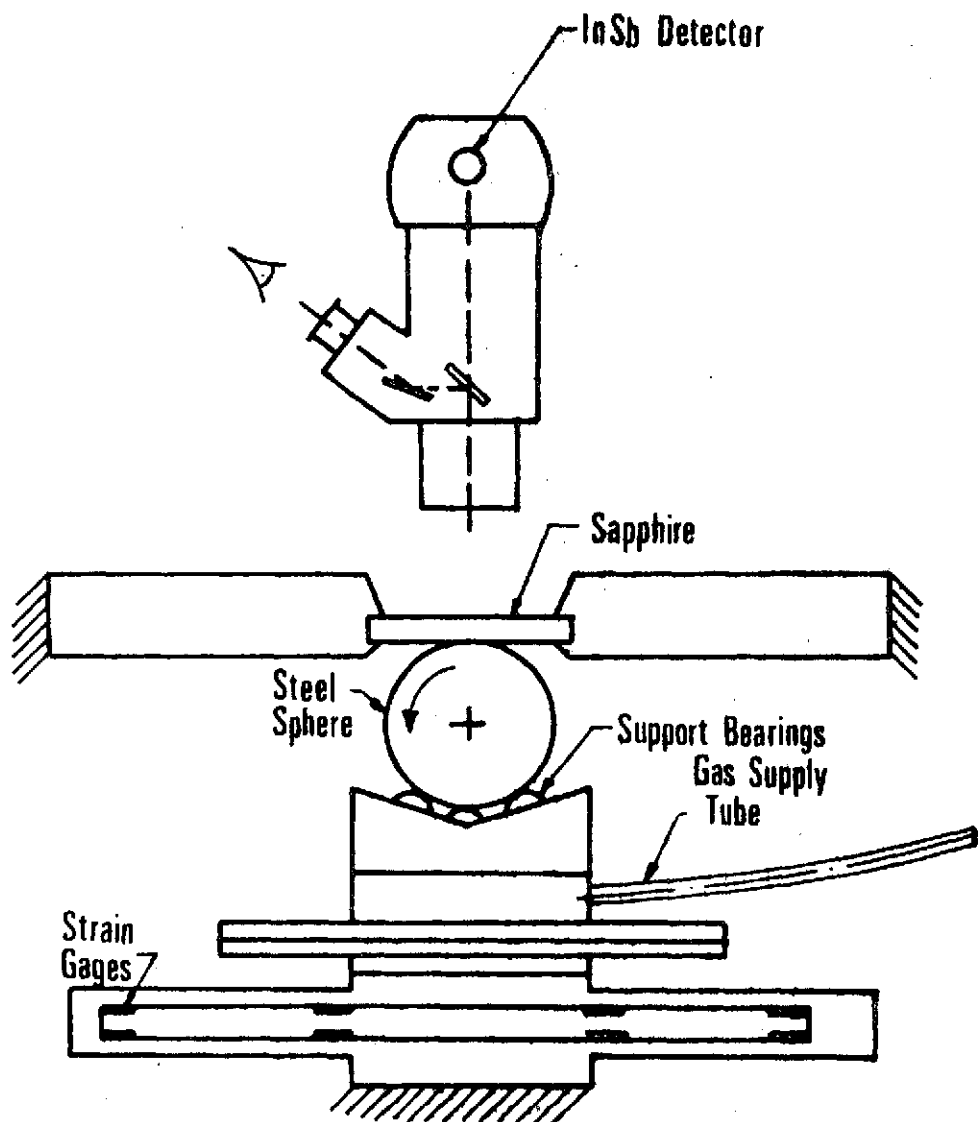
Figure   36. Schematic Diagram of the Experimental
Equipment.

The radiation from this spot plus that from a related solid angle (Figure 36 ) between this spot and the objective are focused onto a liquid nitrogen cooled indium antimonide detector. This detector has a spectral response of 1.8 to 5.5 x $10^{-6}$ m (1.8 to 5.5 microns). The sapphire has a transmissivity of 0.90 over this same range thus allowing the steel ball and oil film radiation to reach the detector. The visible light also collected by the objective is separated from the IR and is directed toward a visual eyepiece. The visual and IR systems are parfocal, and the visual field of view is twenty times as large in diameter as the area which is covered by the IR detector. The area covered by the detector is located in the center of the visual field of view and is indicated by intersecting cross hairs. This allows one to focus on the oil film by visually searching for the interference fringe pattern characteristic of the EHD contact. The detector will then respond to radiation from the 3.56 x $10^{-5}$ m (0.014 in.) diameter oil film and steel ball surface plus a volume of the sapphire disk (see Figure 36 ). Since the temperatures of the lubricant film and the bearing surfaces are desired separately, rather than an average contact temperature, experimental techniques have been devised to isolate the radiation contributions from the sapphire, lubricant film, and steel ball.

Figure 37 shows the components of the radiation received by the In-Sb detector. The radiation emitted from a surface per unit time, area and solid angle is called areal radiant intensity and has units of watts · $cm^{-2}$ · $ster^{-1}$. There are four areal radiant intensity sources: $N_o$ - due to reflected ambient background radiation, $N_s$ - due to emission from the sapphire, $N_b$ - due to emission from the steel ball, and $N_f$ - due to emission from the lubricant film. There is also an attenuation factor
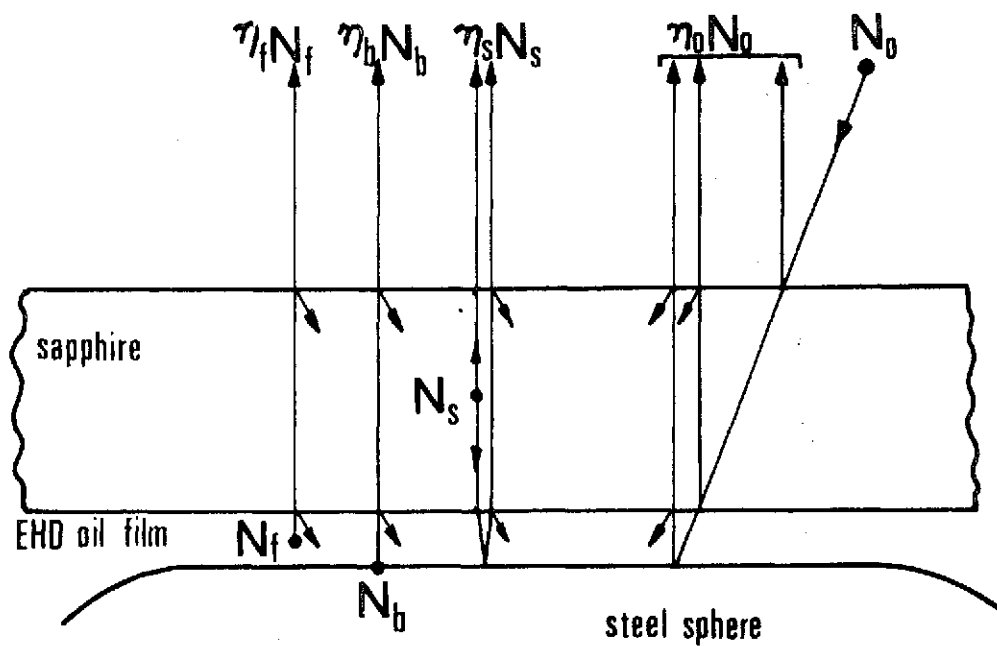
Figure   37. Radiation Incident on the Detector (Angles
Exaggerated for Clarity).

associated with each of these components. Under the conditions listed below, these factors are:

$$\eta_0 = 0.082 + 0.683 \ \rho b$$

$$\eta_s = 1. + 0.830 \rho b \qquad (1)$$

$$\eta_b = 0.830$$

$$\eta_f = 0.830$$

based on

1. Fresnel reflection losses of 0.076 at the sapphire-air interface and 0.0064 at the sapphire - oil interface [ 14 ].

2. sapphire transmissivity of 0.90 for the $1.52 \times 10^{-3}$ m (0.060 in.) thick disk [ 14 ],

3. that the sapphire radiates to both hemispheres and a portion of the radiation initially directed toward the oil film is reflected back to the detector.

4. absorptivity of the oil film is negligible due to its thickness of approximately $2.54 \times 10^{-7}$ m ($10^{-5}$ in.), and

5. that, although the oil film also radiates to both hemispheres, the effect has been accounted for in the value of emissivity assigned to the film.

The IR radiometric detector contains a black body source at ambient temperature. A mechanical chopper in the detector alternately exposes the detector to the total incident radiationand then to the black body reference. The output signal, therefore, is a function of the difference between these values

$$E = k(N_{TOTAL} - N_o) \qquad (2)$$

where k is a known instrument constant. It can be seen from Figure 37 that the total incident radiation is given by

$$N_{TOTAL} = \eta_f N_f + \eta_b N_b + \eta_s N_s + \eta_o N_o \qquad (3)$$

therefore, combining equations 1 – 3 ,

$$E/k = 0.830 \ (N_f + N_b) + (1. + 0.830 \ \rho_b) \ N_s$$

$$+ \ (0.683 \ \rho_b - 0.918) \ N_o \qquad (4)$$

The reflectivity of the ball surface $\rho_b$ can be measured with the radio-metric detector. The quantity $N_o$ is dependent on the ambient temperature only and can be evaluated. The individual areal radiant intensity values $N_f$, $N_b$ and $N_s$ are known functions of the source emissivity and temperature.

The sapphire which is $1.52 \times 10^{-3}$ m (0.060 in.) thick will have a large temperature gradient due to the viscous heating in the oil on one side and ambient air on the other. Radiation is emitted from throughout the thickness rather than just at a surface. Because the temperature distribution of the sapphire is unknown a sapphire surface temperature has not been determined thus far.

Since the steel ball is opaque, a surface emissivity and tempera-ture can be associated with the areal radiant intensity $N_b$. The Emissivity of the ball surface has been determined at several temperatures using the radiometric detector. The technique is to paint a small spot of flat black paint ($\epsilon \simeq 0.95$) on the ball surface, heat the ball to an elevated tempera-ture and then compare the areal radiant intensities at adjacent points on the ball surface – one on and one off the painted section. This technique gave a surface emissivity of 0.28 for the 52100 chrome steel ball. This value was reproducible at several temperature levels.

The emissivity of the oil film must be determined before a film temperature can be calculated. Since the oil film is an absorbing medium with anticipated high temperature gradients, the temperature which will be

assigned to the oil film will be an average temperature across the film. Because the areal radiant intensity is related to the fourth power of temperature, however, this average value will be skewed toward the maximum temperature in the film. In general, the emissivity of the oil film is a function of oil chemistry, wavelength and film thickness. The emissivity, therefore, must be determined for the lubricant being used with the same detector to be used in temperature measurements. Once the dependence on film thickness is known, film thickness profiles previously obtained [ 12 ] can be used to obtain a local emissivity value. McMahon [ 15 ] presents a relation between effective emissivity and film thickness of a semi-transparent material. For a lubricant film thickness h, considered as a heated, reflecting, partially transparent body, the relation is

$$\varepsilon = \frac{(1 - \rho^*)(1 - e^{-\lambda h})}{(1 - \rho^* e^{-\lambda h})} \tag{5}$$

where $\lambda$ is an absorption coefficient for the oil film and $\rho^*$ is the effective reflectivity of the oil film. In a separate experiment in which a stationary ball was placed in a constant temperature bath of the test lubricant with the sapphire resting on top of the ball, the areal radiant intensity was measured near the contact between the surfaces. An oil film occupied the space between the ball and sapphire. Since the dimensions of the gap can be determined from geometry alone, the areal radiant intensity data at a known fluid temperature can be transformed into a local emissivity value. The data obtained resulted in an emissivity of 0.352 for a film thickness of $5.08 \times 10^{-5}$ m (0.002 in.). Solving equation ( 5 ) for $\lambda$ yields $\lambda = 9.43 \times 10^{3}$ m$^{-1}$ (240 in$^{-1}$). For EHD film thicknesses on the order of $10^{-7}$ m ($10^{-5}$ in.), the quantity

$\lambda \cdot h$ is of the order $10^{-3}$, allowing equation ( 5 ) to be accurately approximated by

$$\varepsilon_f = \lambda h \qquad (6)$$

For a given experiment, temperature is a function only of areal radiant intensity and emissivity, therefore,

$$T_b = f \ (N_b, \ \varepsilon_b) \qquad (7)$$

$$T_f = f \ (N_f, \ \varepsilon_f) \qquad (8)$$

Since the film thickness at any point in the contact can be determined using the optical interference technique [ 12 ] $\varepsilon_b$ and $\varepsilon_f$ can be found. However, there remain three equations ( 4,7,8) with five unknowns $(N_f, \ N_b, \ N_s, \ T_b, \ T_f)$. Clearly, two additional independent relations must be found. This has been done by the following two alterations to the experiment described thus far.

In order to determine the ball surface temperature, the EHD experiment was repeated under identical conditions, but with a ball having an emissivity of 0.47 compared with that of 0.28 used in the first experiment. The increase in emissivity was accomplished by allowing the ball surface to react in a high temperature oil bath. A comparison of film thickness values taken using each ball indicated that the conditions in the contact were identical regardless of which ball was used. All other variables remaining constant, the higher ball emissivity will give a higher ball areal radiant intensity $N_b$. We have shown through an order of magnitude analysis (see Appendix D ) that the increased radiation from the ball surface will have a negligible effect on the film and surface temperatures. Therefore, for a given point in the contact, the data from the two experiments using a low and high emissivity ball will result in two different output signals $E_1$ and $E_2$. Since the transmissivity of the

ball is zero [ 16 ]

$$\rho_b + \alpha_b = 1 \qquad\qquad (9)$$

but at equilibrium [ 16 ]

$$\alpha_b = \varepsilon_b \qquad\qquad (10)$$

therefore

$$\rho_b = 1 - \varepsilon_b \qquad\qquad (11)$$

Equation ( 4 ) may now be rewritten for the experiments using balls with low and high emissivity

$$E_1/k = 0.830 \ (N_f + N_{b1}) + 1.598 \ N_s - .426 \ N_o \qquad (12)$$

$$E_2/k = 0.830 \ (N_f + N_{b2}) + 1.440 \ N_s - .556 \ N_o \qquad (13)$$

where the subscript 1 refers to the low emissivity ($\varepsilon_{b1} = .28$, $\rho_{b1} = .72$) and 2 refers to the high emissivity ball ($\varepsilon_{b2} = .47$, $\rho_{b2} = .53$). Subtracting equation ( 12 ) from ( 13 )

$$\frac{E_2 - E_1}{k} = 0.830 \ (N_{b2} - N_{b1}) - 0.158 \ N_s - .130 \ N_o \qquad (14)$$

The black body areal radiant intensity is a function of temperature only with

$$N = \varepsilon \ N^{BB} \qquad\qquad (15)$$

Since the ball surface temperatures are assumed equal in cases 1 and 2, equation ( 14 ) may be rewritten as

$$\frac{E_2 - E_1}{k} = 0.158 \ N_b^{BB} - .158 \ N_s - .130 \ N_o \qquad (16)$$

With an ambient temperature of 20°C, $N_o = 3.7 \times 10^{-3}$ watts/cm$^2$ - ster.

A conservative estimate of $N_s$ (see Appendix E) is on the order of $0.4 \times 10^{-3}$ watts/cm$^2$ - ster or about 2 percent of $N_b^{BB}$ and has, therefore, been neglected. The value of $N_b^{BB}$ is typically of the order $20 \times 10^{-3}$ watt/cm$^2$ - ster. The only unknown in equation ( 16) is $N_b^{BB}$. The temperature can be obtained from the black body areal radiant intensity through the calibration curve supplied with radiometric detector.

Although the two experiments described above allow the determination of the ball surface temperature they are not sufficient to allow the film temperature to be deduced. The technique devised to isolate the film areal radiant intensity consists of an experiment in which the low emissivity ball is used. The detector output signal $E_1$ is then compared with the signal $E_3$ obtained with a filter placed between the upper sapphire surface and the detector objective (see Figure 36). The filter consists of a sandwich of two sapphire disks and a $5 \times 10^{-5}$ m (0.002 in.) thick film of oil identical in composition to that being used in the EHD contact. Hence the radiation from the EHD oil film is absorbed by the oil in the filter. As can be seen from Figure 38, those contributions other than $\eta_f N_f$ shown in Figure 37 have been attenuated by a filter attenuation factor $\eta_F$. Because of a strong absorption band (C-H bond) in the aliphatic oil at 3.4μ, the EHD oil film will emit primarily at this wave length. Since a much thicker film of the same oil is used in the filter, the filter will absorb the entire contribution $\eta_f N_f$ from the EHD oil film. A reflecting shield is placed between the upper surface of the EHD contact sapphire and the filter until just prior to recording the total radiation to maintain the filter at ambient temperature. Otherwise, the absorption of $\eta_f N_f$ would raise the filter temperature to some unknown value. Figure 38 also shows that the filter itself is emitting at $T_o$ and that some of the background radiation

$$\eta_f \eta_0 N_0 \quad \eta_F \eta_s N_s \quad \eta_f \eta_b N_b \quad \epsilon_r N_0 \quad \rho N_0 \qquad \cdot N_0$$

sapphire

oil film

filter

sapphire

air

sapphire

$$\eta_0 N_0 \quad \eta_f N_f \quad \eta_s N_s \quad \eta_b N_b$$
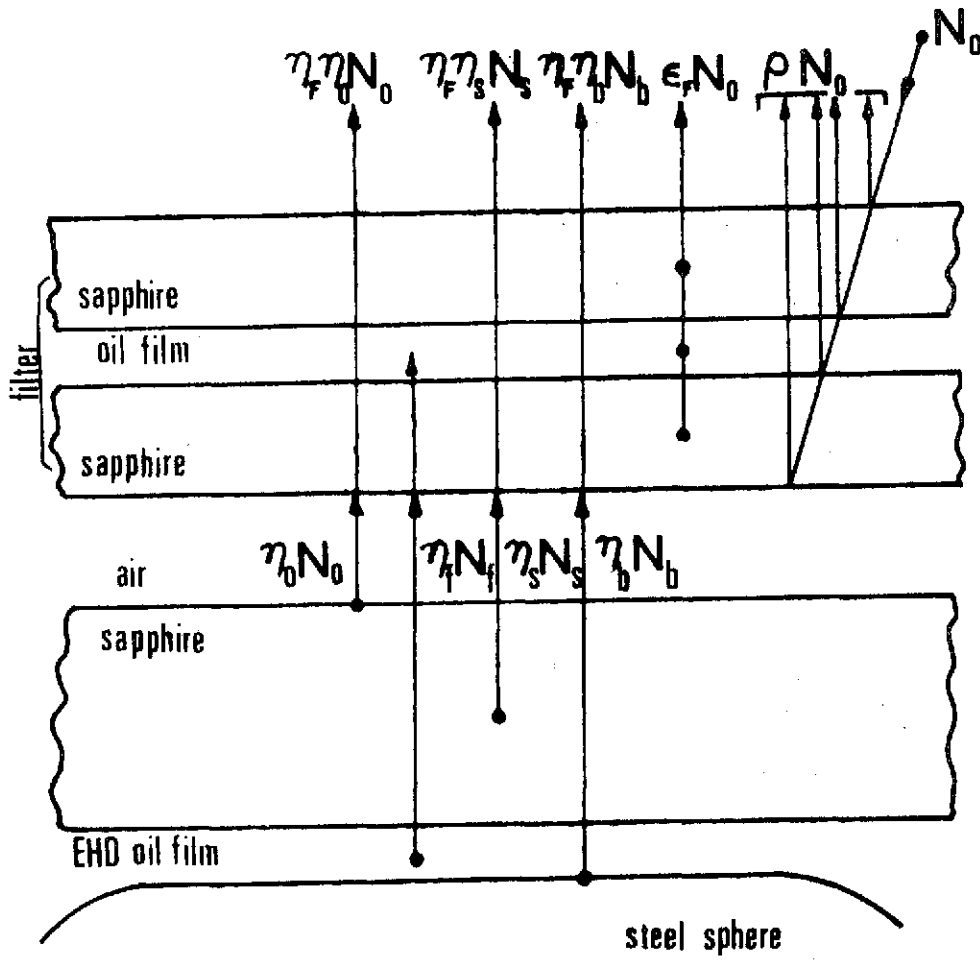
EHD oil film

steel sphere

Figure   38. Oil Film Filter (Not to Scale).

is also reflected from the filter. The total areal radiant intensity received in this third experiment is, therefore,

$$(N_{TOTAL})_3 = \eta_F (\eta_{b1} N_{b1} + \eta_s N_s + \eta_o N_o) + \varepsilon_F N_o + \rho_F N_o \qquad (17)$$

Substituting equations ( 1 ) and (17 ) into equation (12) we get,

$$E_3/k = \eta_F (.830 N_{b1} + 1.598 N_s + .574 N_o) - (1 - \rho_F - \varepsilon_F) N_o \qquad (18)$$

Since for transparent medium [16 ]

$$t_F + \rho_F + \varepsilon_F = 1 \qquad (19)$$

the last term in equation ( 18) may be written as $t_F N_o$. The transmissivity of the filter $t_F$ can be related to the attenuation factor $\eta_F$ which includes transmission and reflection losses

$$\eta_F = (1 - \rho_F) t_F = 0.850 \ t_F \qquad (20)$$

where the reflection losses are calculated Fresnel reflections at the sapphire-air and sapphire-oil interfaces. Substitution of equation ( 20) into ( 18) and subtracting from equation ( 12) yields,

$$(E_1 - \frac{E_3}{\eta_F}) \frac{1}{k} = 0.830 N_f + 0.176 N_o = 0.830 \varepsilon_f N_f^{BB} + 0.176 N_o \qquad (21)$$

The quantities $E_1$ and $E_3$ are the output signals, and k and $N_o$ are known. The film emissivity $\varepsilon_f$ can be obtained from equation ( 6) since the film thickness profile has also been obtained throughout the contact [17]. The filter attenuation factor has been found experimentally by placing the filter between the detector objective and a calibrated black body source (Barnes, Model RM 121). Because of the spectral shift in peak

power wavelength with increasing temperature, this attenuation factor is
a function of the equivalent black body source temperature. Using the
black body source, a calibration curve of $\eta_F$ as a function of temperature
was obtained.

Based on an initial estimate of the EHD film temperature $T_f$, a
value of $\eta_F$ is inserted in equation (21) which is then solved for $N_f^{BB}$.
The film temperature is then determined directly from this value. A
better estimate of $\eta_F$ can be used in equation (21) until convergence on a
film temperature is obtained. Because the variation of $\eta_F$ in the range
of interest is small, convergence is rapid.

The procedure needed to obtain a mean film temperature and ball
surface temperature, therefore, requires that data from four separate
experiments be obtained: the film thickness using optical interference
methods and radiation data for the low emissivity ball with and without
the oil film filter and the high emissivity ball without the filter. The
success of the procedure is based on the fact that the data in the EHD
experiment are reproducible [ 17] thereby assuring identical conditions in
each of the four experiments.

In order to collect a large amount of data in a short period of
time so that the contact temperatures will not change significantly, a
scanning system has been built into the detector mount which permits the
detector to scan through the contact area in the direction of the surface
velocity. Data were taken continuously in the direction of the scan at
a constant detector speed of 0.0075 in/sec. The infrared detector has a
temperature resolution of 5°C corresponding to 0.01 sec response time.
The temperature resolution improves to 0.5°C for a response time of 1.0 sec.
Successive passes were made at $2.5 \times 10^{-5}$ m (0.001 in.) increments. From

these data points, the contour maps shown in Figures 39 and 40 were developed. The recorded output E/k of the detector, after analysis, can then serve directly as a map of total areal radiant intensity as a function of contact position.

## Experimental Results

The lubricant used during this investigation is a naphthenic mineral oil used in previous EHD studies [12,13 ,17 ] and viscometric studies [ 2 ] in this laboratory. The fluid has been shown to be Newtonian [ 2 ] at shear rate and pressure levels approaching those anticipated in the EHD contact. The atmospheric pressure viscosity is $0.0217$ $Ns/m^2$ (21.7 cp) at 37.8 C and $0.0032$ $Ns/m^2$ (3.2 cp) at 98.9 C and the pressure-viscosity characteristic $\alpha^*$ is $2.32 \times 10^{-8}$ $m^2$ (1.60 x $10^{-4}$ $in^2/lbf$).

All data was obtained with a peak Hertz contact pressure of $1.034 \times 10^9$ $N/m^2$(150,000 psi). Sliding velocities of 0.35, 0.69 and 1.39 m/s (13.7, 27.4 and 54.9 in/sec) were used in the investigation.

Using the infrared techniques developed in the previous section, contour maps of the steady state film and ball surface temperatures have been obtained and are shown in Figures 39 and 40 for the maximum sliding velocity. In each of these figures the boundary of the Hertzian contact region is shown for reference. Since the EHD contact is assumed to be symmetric about the centerline only one half of the contact area has been studied. Figure 41 shows the interference fringe pattern for the same conditions (1.39 m/s, $1.034 \times 10^9$ $N/m^2$) as used in Figures 36 and 37 .

In all these figures, the lubricant is entering the contact at the top of the figure. Referring to Figure 39 , it can be seen that along the contact centerline, the lubricant is at 30°C just ahead of the contact
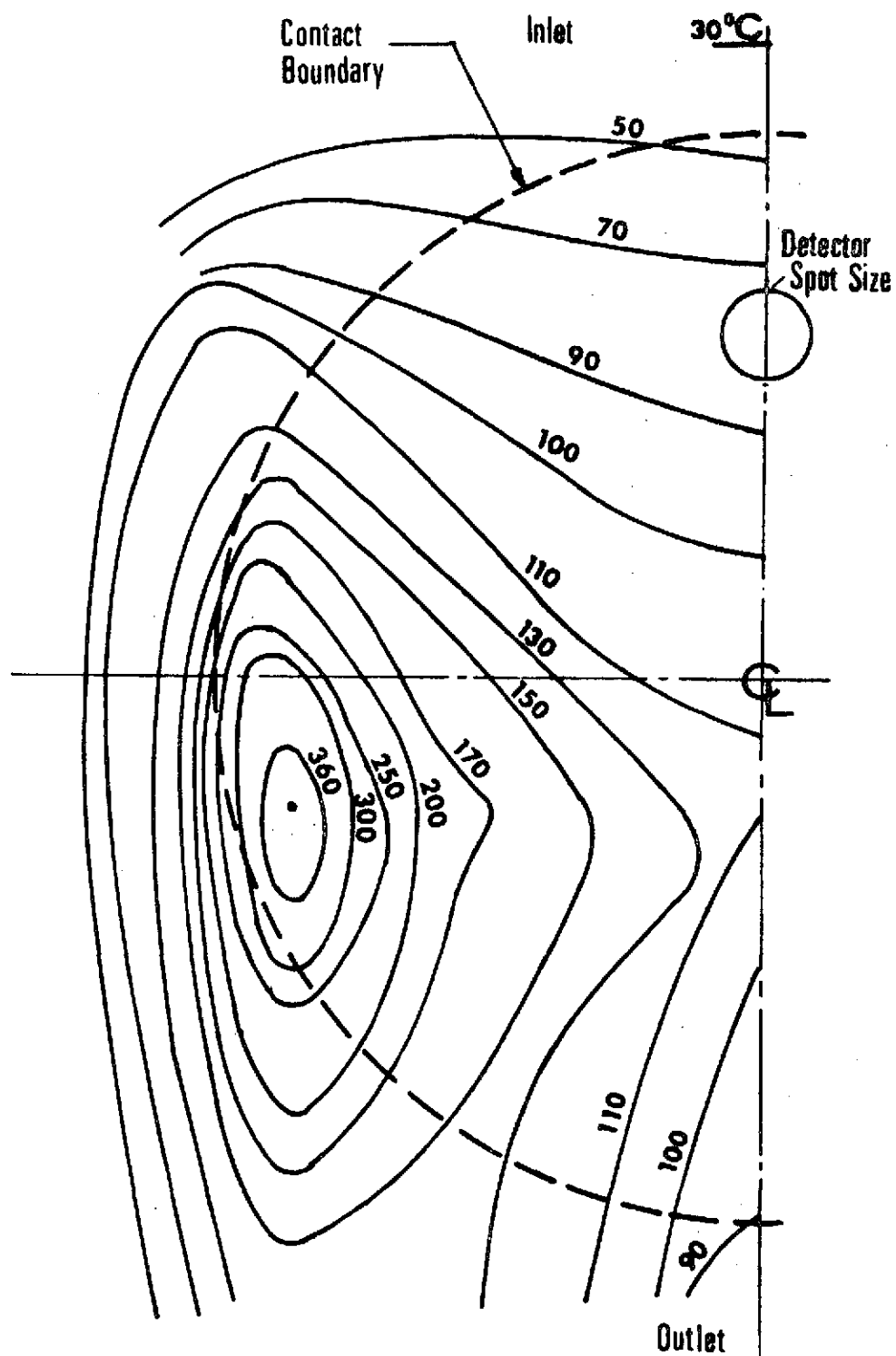
Figure   39. Steady State Film Temperature in the EHD
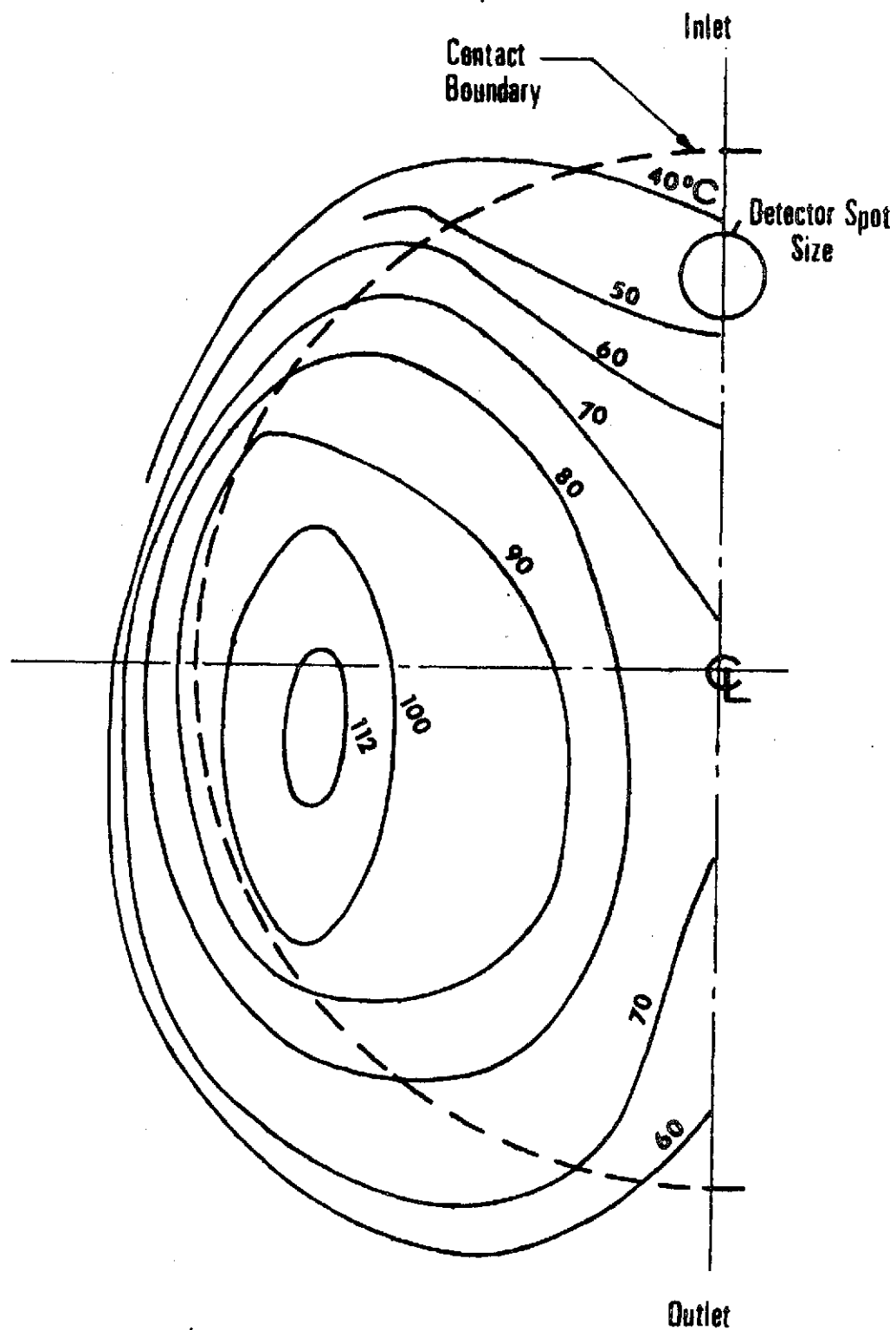         Contact at 1.39 m/sec (54.9 ips) Sliding
         Speed.

Figure 40. Ball Surface Temperature in the EHD Contact
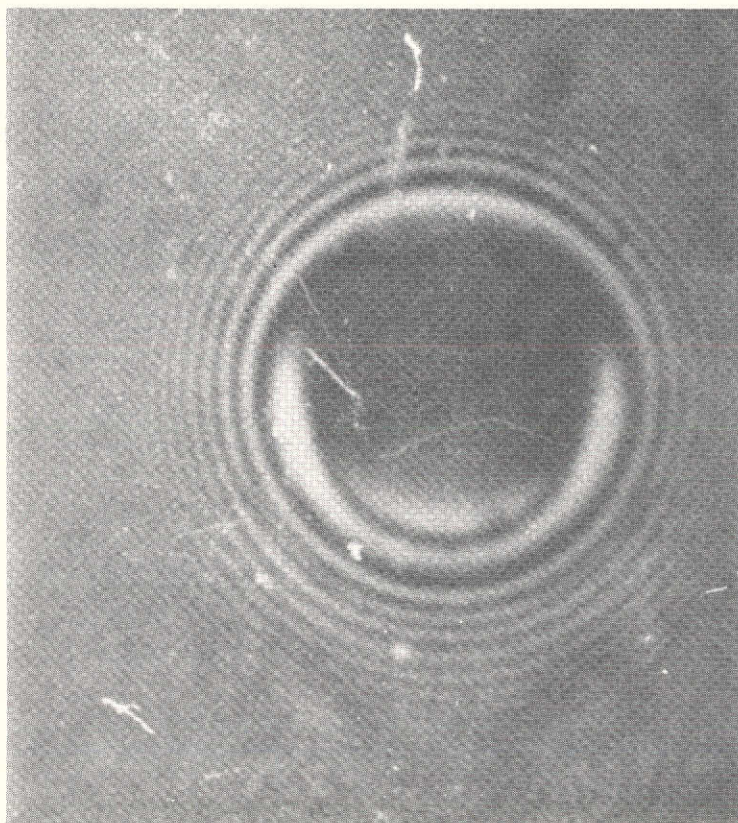at 1.39 m/sec (54.9 ips) Sliding Speed.

Figure 41.  Interference Fringe Pattern of the EHD Contact
at 1.39 m/sec (54.9 ips) Sliding Speed.

inlet and increases in temperature to almost 50°C as it crosses the
Hertzian contact boundary. The film reaches a maximum of 115°C just
beyond the contact center and exits from the contact region at 75°C.
The most striking feature about Figure 39, however, is the fact that the
maximum film temperature ($\simeq$ 360°C) occurs at the minimum film thickness
location (See Figure 38) in the EHD side lobe constriction. Based on
previous measurements [ 17] the film thickness at this location is only
6.35 x 10$^{-8}$ m (2.5 x 10$^{-6}$ in.).

Figure 40 is a plot of the ball surface temperature distribution.
The ball surface temperature is less than 40°C at the contact inlet,
rises to over 70°C just beyond the contact center and exits the contact
at just under 60°C. As is the case for $T_f$, the maximum ball surface
temperature occurs in the side lobe constriction. The maximum values of
$T_f$ and $T_b$ do not appear to be at precisely the same locations, however.
The maximum ball temperature is only 115°C compared with 360°C for the
lubricant film.

The temperature contours shown in Figures 39 and 40 were the
maximum steady state values obtained during the investigation. Figures
42 and 43 show the variation with sliding velocity of steady temperature,
$T_f$ and $T_b$ along the contact centerline. At each position in the contact
and at each speed, the mean film temperature is substantially higher than
the ball surface temperature. This is consistent with the fact that there
is internal heat generation in the film due to viscous shear and that con-
duction to the boundaries is a primary heat transfer mechanism.

Finally, Figure 44 is a plot of maximum ball surface temperature
in the contact as a function of sliding velocity. As was mentioned above,
the maximum temperature is found in the EHD side lobe constriction.
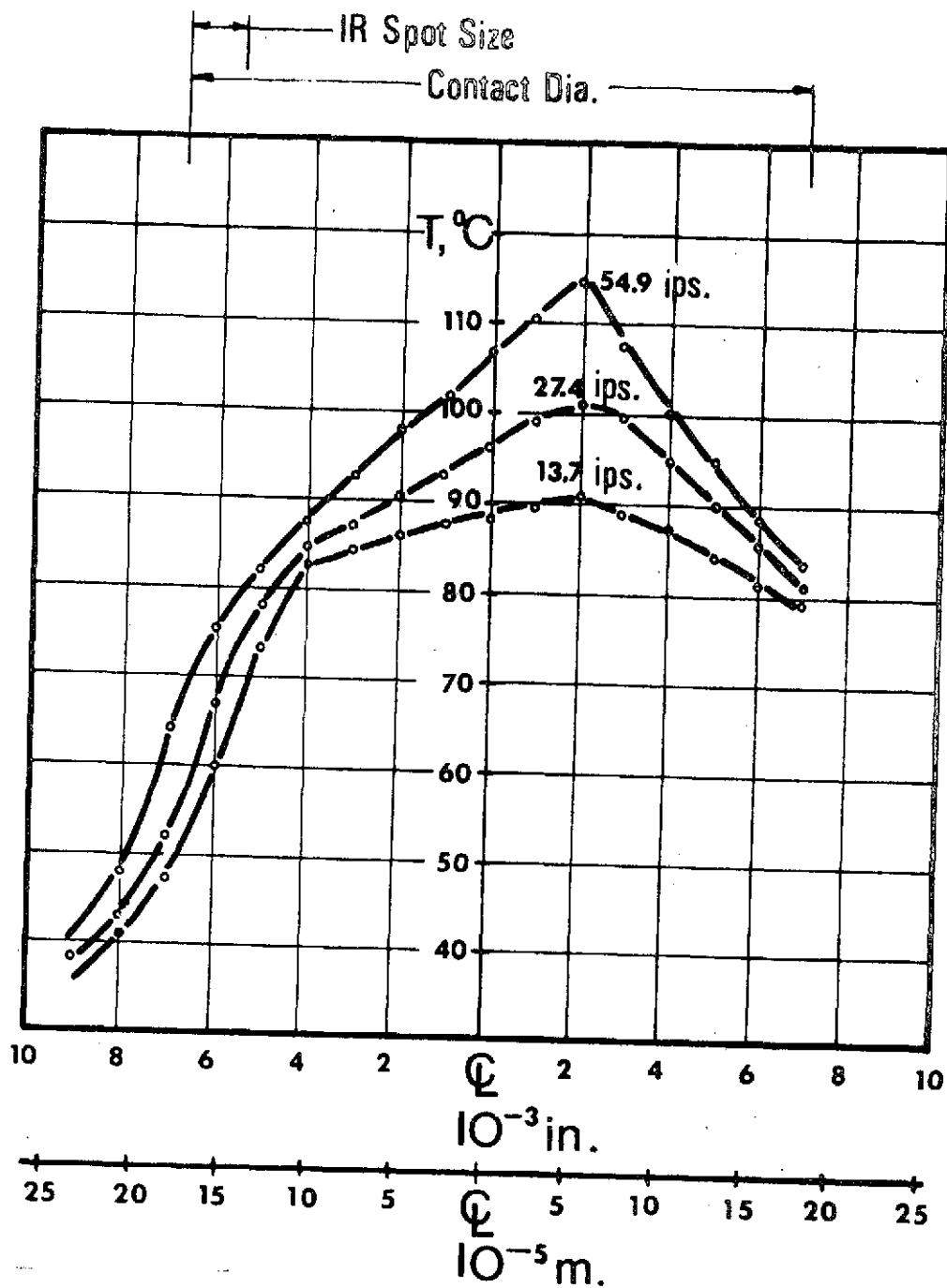
Figure 42. Steady State Film Temperature Distribution along the Contact Centerline as a Function of Sliding Speed.
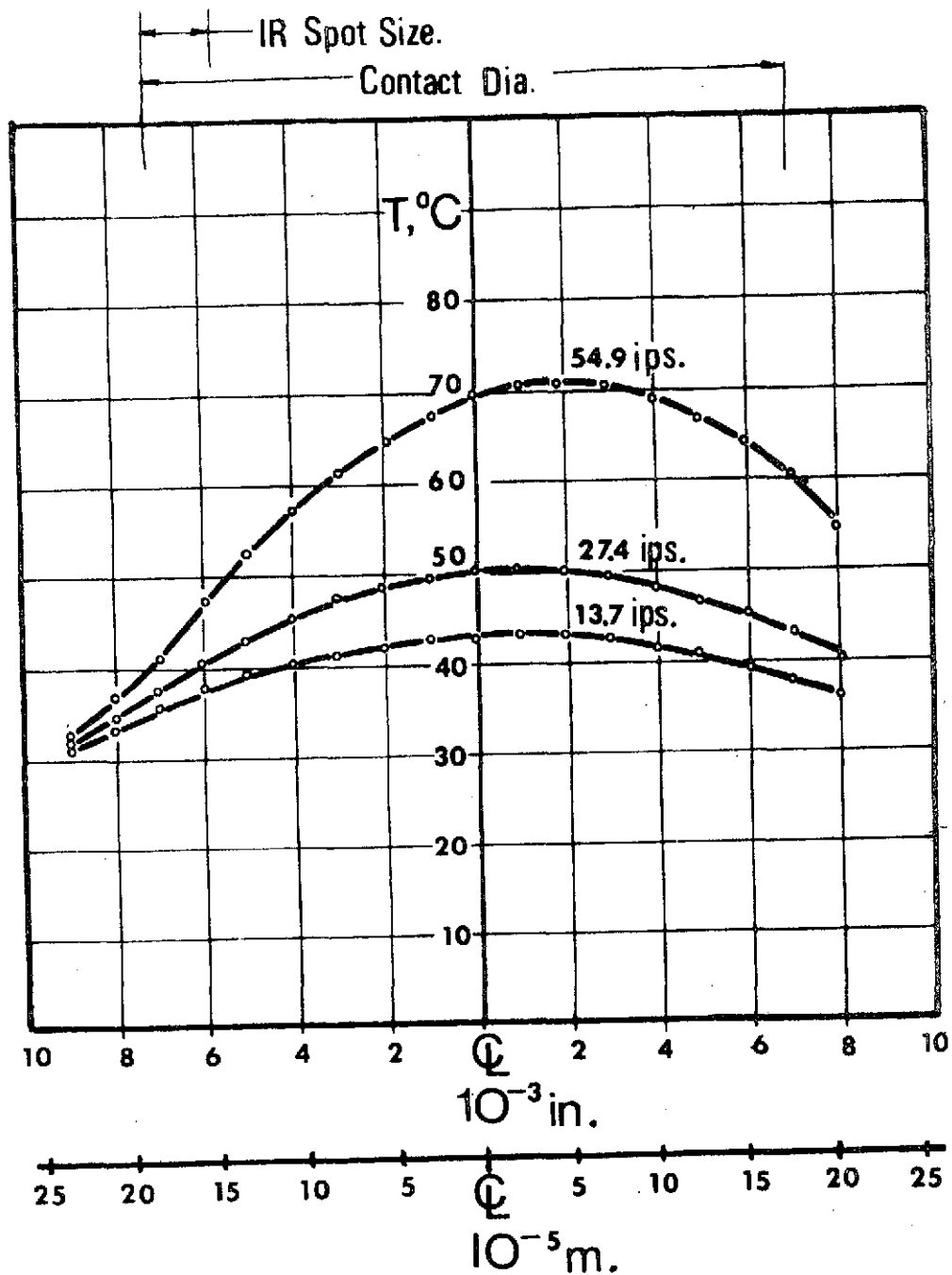
Figure 43. Ball Surface Temperature along the Contact Centerline as a Function of Sliding Speed.
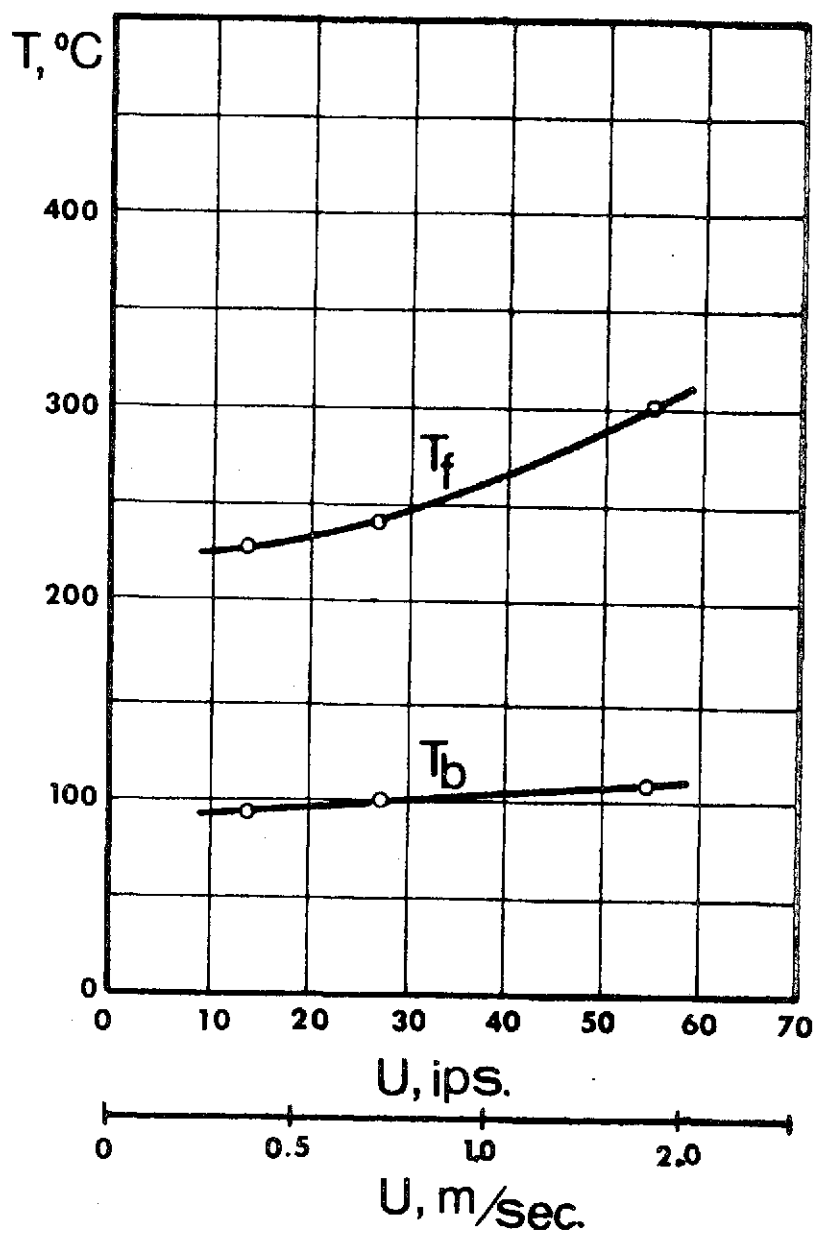
Figure 44. Maximum Ball Surface Temperature and Film
Temperature as a Function of Sliding Speed.

Figure 43 also shows the film temperature variation with sliding velocity at the same contact location where the maximum ball temperature was found. Due to significant film emissivity variation throughout the contact, this location, which is the point of maximum radiation is not necessarily the point of maximum $T_f$. Except for the highest sliding velocity experiment, sufficient data were not obtained to find the maximum fluid temperature in the side lobe constriction.

## Discussion of Results

The most useful temperature data which could be obtained for an EHD contact would be the sapphire and ball surface temperatures plus the temperature profile through the lubricant film. We have presented a technique wherein the actual ball surface temperature and a fourth power average fluid temperature taken through the film can be determined. The fact that the fourth power average is determined means that the peak film temperatures will be somewhat higher than the data presented.

Throughout the above discussion film thickness data has been used which was taken in a separate experiment with essentially the same apparatus. In the film thickness investigations, a $3.18 \times 10^{-3}$ m (.125 in.) thick sapphire was used whereas a $1.52 \times 10^{-3}$ m (.060 in.) sapphire was used in IR investigations. Because the thickness of the sapphire may influence its temperature distribution, thus changing the thermal boundary condition in the contact, film thickness and traction data were taken using both sapphires and were found to be identical.

The detector has been calibrated over the temperature range of interest using a radiometric calibration source (Barnes, Model RM-121). The detector resolution under the conditions of the experiment is 0.5C

according to manufacturer's specifications. Because of this relatively high resolution, the accuracy of the temperature data reported is primarily a function of the emissivity values and the proportion of received radiation assigned to each source in equations ( 15 , 16 , 21 ). The measured emissivity values for the ball surface used are believed to be correct to well within 10%. If this $\pm$ 10% error is carried through the above equations it amounts to an error in ball temperature of $\pm$ 4 $^{\circ}$ C at the maximum contact temperature of 115 $^{\circ}$ C. At locations where the temperature is less than this maximum the error will be lower. Also, if any of the calculated coefficients in quations ( 16 ) and ( 21 ) are in error by $\pm$ 10%, a similar error in ball temperature will result.

The most significant possible error is in the emissivity assigned to the oil film. From equation ( 6 ) it is seen that the emissivity is proportional to film thickness. Unfortunately, the error in film thickness is an absolute quantity (depending on fringe order interpretation (see Figure 41) rather than a percentage of the film thickness. This yields a maximum relative error at points of minimum film thickness, which are located at the points of maximum film temperature. The maximum error in film thickness has been assessed at $\pm$ 1.8 x 10$^{-8}$ (0.7 x 10$^{-6}$ in.) corresponding to misreading a contour on the film fringe pattern. At the point of maximum film temperature (360$^{\circ}$C) this $\pm$ 1.8 x 10$^{-8}$m error in minimum film thickness (6.4 x 10$^{-8}$ m) results in an error in temperature of $\pm$ 30 $^{\circ}$C. At all other locations within the contact, this error is substantially less because the film thickness is larger and the error in reading represents in this case only a fraction of its actual value. Also, for investigations in which the minimum film thickness is greater than 6.4 x 10$^{-8}$ m, which includes most cases previously investigated in

this laboratory [12, 13, 17], the error is expected to be less.

The extremely high local fluid temperatures found in this investigation are thought to be a result of the high shear rates ($10^7$ sec$^{-1}$) at minimum film thickness locations in the Hertzian contact. The question does arise, however, whether the shearing is viscous with complete separation of the surfaces, or there is actually some asperity contact at the minimum film thickness locations. This is a possibility for the cases reported above since the minimum film thicknesses in the side lobes are of the order of the surface roughness values for the ball and sapphire. It is not obvious if asperity contact is occurring, however, since the ball surface shows no surface damage after running under load for several minutes. An investigation is currently under way [18 ] to determine which mechanism is causing these extreme temperature values.

In this research [ 18] a model was developed to determine the relationship between the adiabatic stationary wall temperature $T_{mw}$, which is the maximum fluid temperature and the moving wall temperature $T_1$. This model is based on the assumptions that the only heat source is the viscous dissipation at constant shear stress rate. It results in a relationship of the form,

$$\int_{T_1}^{T_{mw}} K_T \frac{dT}{\eta(p,T)} = U^2 \tag{22}$$

where:

$K_T$ = thermal conductivity

= 0.0167 lbf/sec $^\circ$F

$\eta(p,T)$ = fluid viscosity function of the local pressure and temperature

U = sliding speed

It should be noticed that the average fluid temperature, mapped in the Figure 39, has to be at any time smaller than that of the adiabatic stationary wall temperature, unless some additional heat sources other than viscous dissipation in the fluid are present. The equation ( 22) was solved graphically for the maximum wall temperature due to viscous dissipation. The temperature obtained from the analysis was found to be less than the lubricant temperature experimentally deduced in some regions. The findings indicate the existence of a region in the contact area where a heat source, other than viscous dissipation, influences the lubricant temperature (Figure 45). In the conditions under investigation the asperity contact is assumed to be the additional energy source causing the high fluid temperature.

As seen in Figure 45, part of the area where the asperity contact may be present corresponds to that expected as a result of small film thicknesses in the side lobes. The roughness of the sphere used is $3.18 \times 10^{-8}$ m ($1.3 \times 10^{-6}$ in.) and the minimum film thickness for a speed of 1.30 m/sec (54.9 in.sec) and load of 6.8 Kgf (15 lbf) is $6.35 \times 10^{-8}$ m ($2.5 \times 10^{-6}$ in.).

If the asperity contact plays an important role in causing the high fluid temperature, the infrared technique can be an useful tool in detecting incipient film failure in highly loaded contacts.

## Conclusions

We have presented a technique for mapping the temperature distribution in a sliding EHD contact. Both the ball surface temperature and a fourth power average lubricant film temperature have been obtained
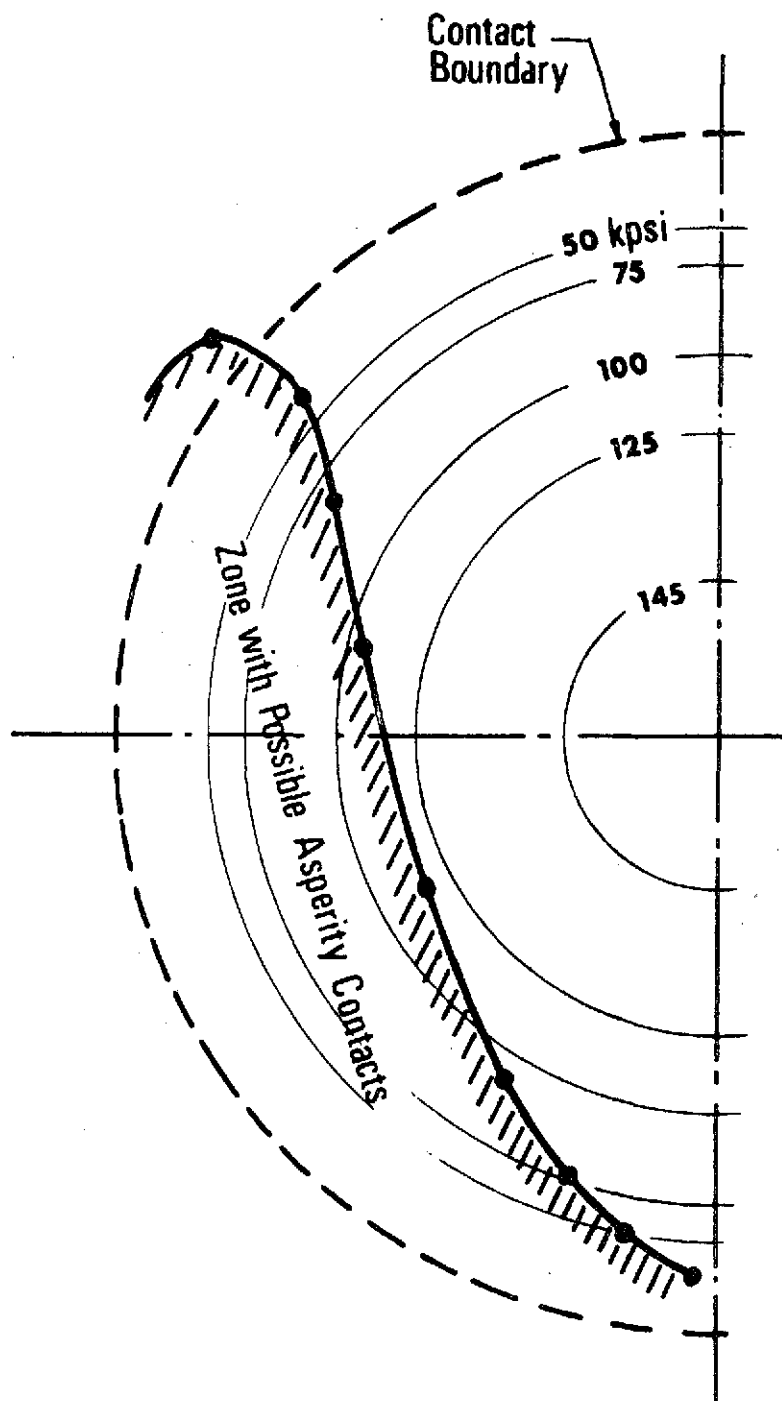
Figure 45. Contact Region with External Heat Source
(Asperity Contacts).

at points throughout the contact. Under a specific set of experimental conditions, ball temperatures as high as 115°C and average fluid film temperatures as high as 360°C have been reported. Both temperature peaks were found to occur in the contact side lobes where the film thickness is a minimum. It was also observed that at each point in the contact, both temperatures increased significantly as the sliding velocity was increased.

Although only a limited amount of data was collected, it is sufficient to show that the technique reported can be useful in obtaining detailed temperature data in the EHD contact. In addition, it also suggests additional experiments using the IR microdetector; namely extensions to rolling contact experiments, to a determination of the sapphire surface temperature, to a spectral analysis of the materials in the contact, to aid in evaluating lubricant constitutive equations under EHD conditions, and to an investigation of the mechanisms leading to film failure.

c.  The General Viscous Lubrication of Rolling and Sliding
Rigid Cylinders

## Introduction

The objective of the research in this section is to develop

a general theory of the viscous lubrication of sliding and rolling cylinders.

The fluid behavior considered is restricted to the case of the rheological

behavior of the fluid being completely described by a viscosity function

which is time independent.  That is, the rheological model of the fluid

excludes either normal stress effects or shear viscoleasticity.  To

date, and in the next six months, the isothermal case only is considered.

The load range being studied spans the complete range from the lightly

loaded case characterized by rigid cylinders to the highly loaded elastic

cylinder case of full elastohydrodynamic lubrication.

This report is of the completion of the first phase; that of rigid

cylinders and shear thinning fluids which do not exhibit a second

Newtonian in their viscosity shear stress relation.  The cases of the

fluid with a second Newtonian and that of elastic cylinders with the

full range of fluid behavior are both nearly completed and a complete

report on those is expected in the next year.

## Problem Formulation

A description of the system considered and its mathematical

representation is discussed in detail in the previous annual report.

This representation will only be briefly reviewed here.  The system

geometry and kinematics are shown in Figure 46.  Let $(R)$ be the equivalent

radius of the system and $(h_o)$ be the centerline spearation.  Let $(u_1)$

and $(u_2)$ be the lower and upper surface velocities.  Let $(x_a)$ and $(x_b)$ be
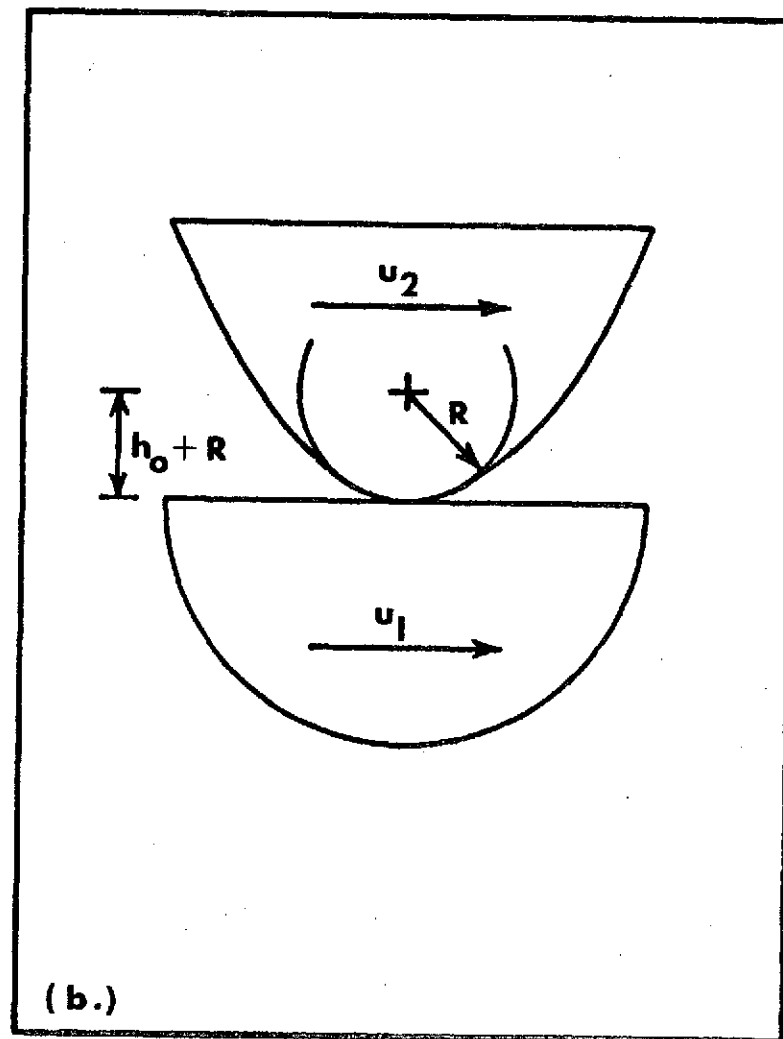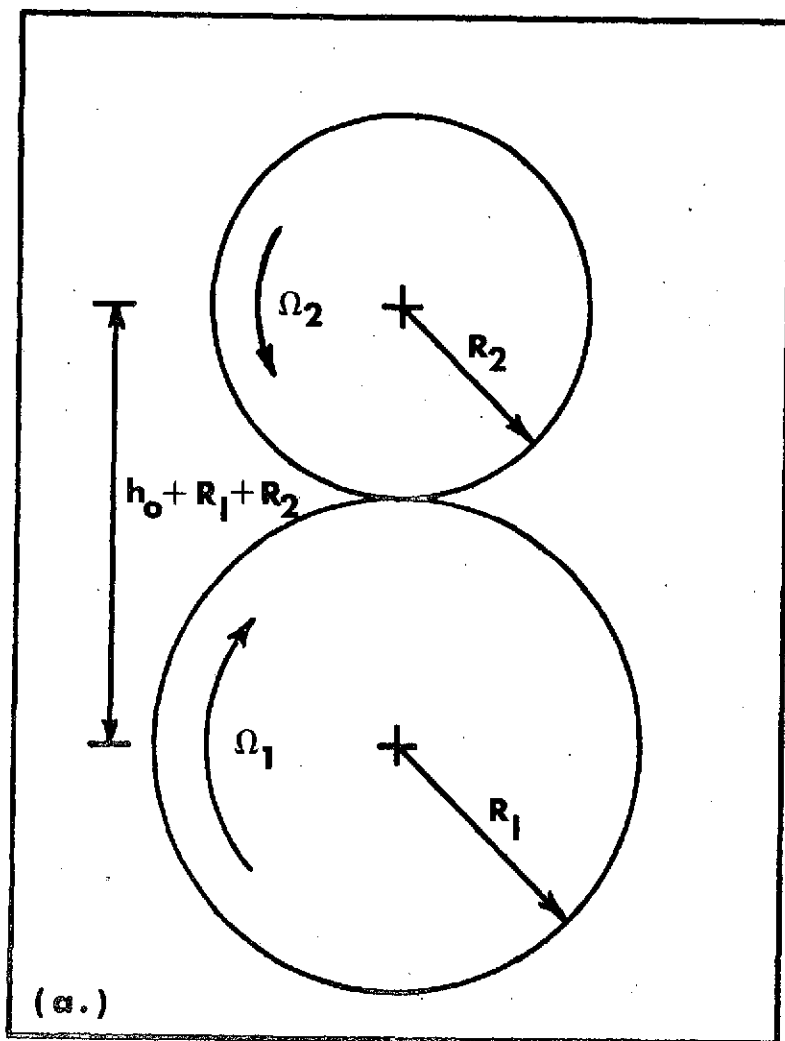
Figure 46. System Geometry & Kinematics. (a.) Original Geometry & Kinematics. (b.) Equivalent Geometry & Kinematics.

the inlet and outlet coordinates of the film. Let (h) be the film thickness, (s) be the shear stress on the lower surface and (p) be the pressure. Let (d) be the density and (z) be the viscosity of the fluid. The density and viscosity functions may be expressed in the form

$$d = d_0 \, (1 + dn)^{-1} \tag{23}$$

$$z = z_0 \, e^{b \, p} \, (1 + zn)^{-1} \tag{24}$$

where $(d_0)$ and $(z_0)$ are respectively the base density and viscosity, (b) is the log viscosity pressure coefficient and (dn) and (zn) are the density and viscosity deviation functions. The term (dn) is a function of pressure only while the term (zn) is a function of shear stress only. Then the shear stress on the lower surface and the pressure are given by

$$S(s,t) = s - s_0 - sn(s,t) = 0 \tag{25}$$

$$T(s,t) = t - t_0 - tn(s,t) = 0 \tag{26}$$

subject to the boundary conditions

$$x_a = 0 \tag{27}$$

$$x_b = 0 \tag{28}$$

and where

$$s_0 = 6 \, U \, z_0 \, e^{b \, p} \, (- (1 + A) \, h + (1 + dn) \, h_b) \, h^{-2} \tag{29}$$

$$t_0 = 12 \, U \, z_0 \, e^{b \, p} \, (h - (1 + dn) \, h_b) \, h^{-2} \tag{30}$$

$$t = h \, (\frac{dp}{dx}) \tag{31}$$

$$sn(s,t) = -4 \, SIn(s,t) - 6 \, TIn(s,t) \tag{32}$$

$$tn(s,t) = 6 \, SIn(s,t) + 12 \, TIn(s,t) \tag{33}$$

$$SIn(s,t) = t^{-1} \int_s^{s+t} Z \ zn \ (Z) \ dZ \qquad (34)$$

$$TIn(s,t) = t^{-2} \int_s^{s+t} Z \ (s - Z) \ zn(Z) \ dZ \qquad (35)$$

$$h = h_0 + .5 \ R^{-1} \ x^2 \qquad (36)$$

$$h_b = h_0 + .5 \ R^{-1} \ x_b^2 \qquad (37)$$

$$U = .5 \ (u_1 + u_2) \qquad (38)$$

$$A = (-u_1 + u_2) \ (6 \ U)^{-1} \qquad (39)$$

The equations (25) through (39) represent the system behavior for fluids described by equations (23) and (24). For evaluation of the system, the density and viscosity deviation functions must be specified. A large class of fluids is described by

$$dn = e \ p \ (1 + f \ p \ )^{-1} \qquad (40)$$

$$zn = (k \ t)^m \qquad (41)$$

where (e) and (f) are reciprocal pressures and (k) is a reciprocal shear stress. The exponent (m) is assigned a value of 2 in this investigation. Such a specification is in agreement with observations of the density and viscosity behavior of a variety of fluids of interest. Such fluids as common petroleum oils, silicone oils and various bulk polymers are adequately described over a wide range of pressures and shear stresses by this specification. The values of (e) and (f) are of the order $5 \times 10^{-6}$ $\text{psi}^{-1}$. Such a value of (k) implies that the viscosity of the fluid has been reduced by 50% at a shear stress of 5 psi. A plot of the nondimensional log viscosity vs. the nondimensional log shear stress is shown in Figure 47 .

For the above choice of viscosity deviation functions (zn), equations (32) and (33) reduce to

$$sn(s,t) = k^{-2} \ (-s^3 + .5 \ s \ t^2 + .2 \ t^3) \qquad (42)$$

$$tn(s,t) = k^{-2} (-3 \ s^2 \ t - 3 \ s \ t^2 - .9 \ t^3) \qquad (43)$$
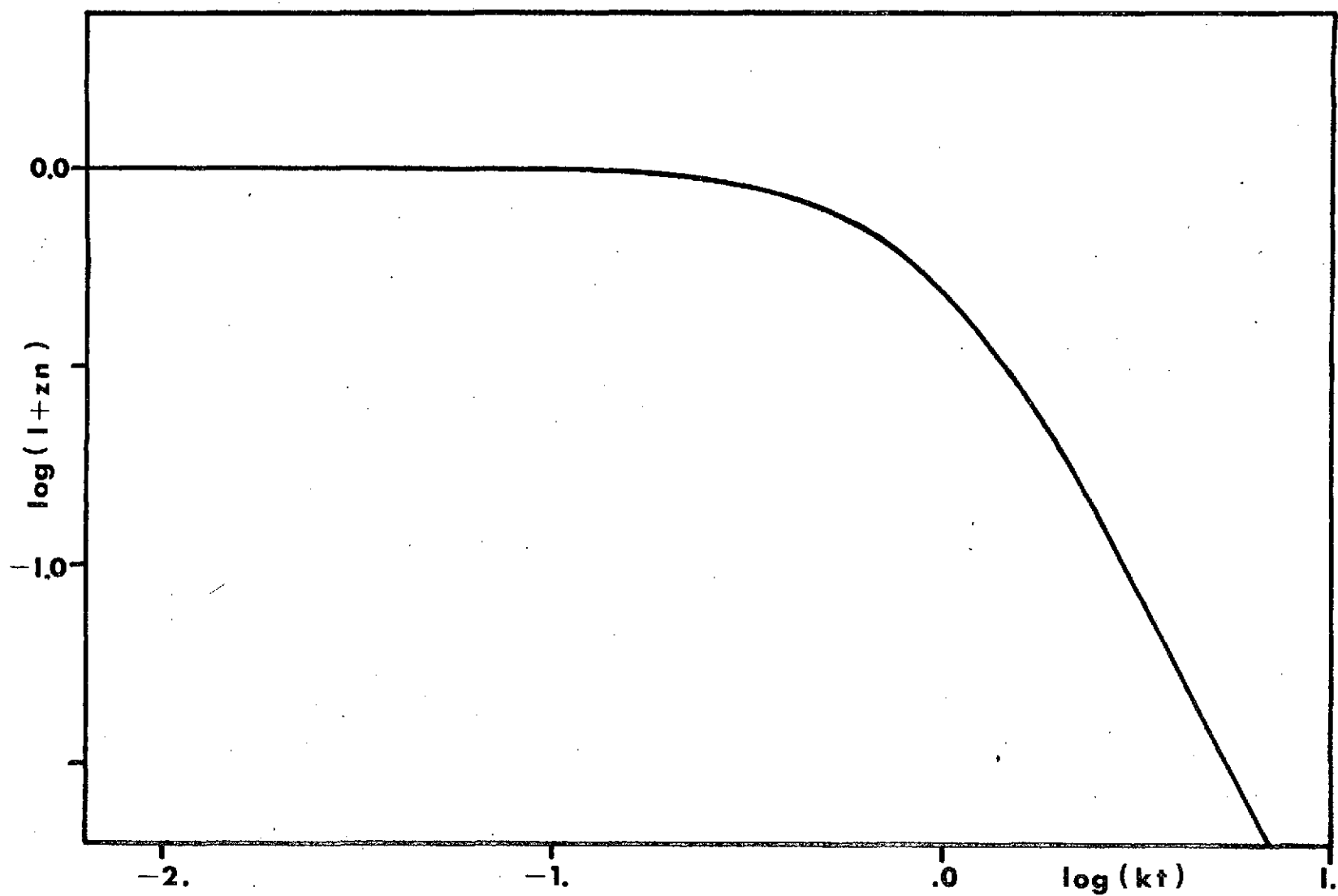
**Figure** 47. **Nondimensional Log Viscosity** $(-\log(1+zn))$ **vs Nondimensional Log Shear Stress** $(\log(kt))$.

## Problem Solution

This system of equations is essentially a nonlinear first order differential equation with a free boundary. An approximate solution of such equations can be obtained as the solution of the related system of finite difference equations. These are nonlinear algebraic equations and may be solved by a variety of well-known iterative methods.

A direct application of the Newton-Raphson method is ineffective and a modified method is shown schematically in Figure (48). The grid spacing is variable. The inlet and outlet regions are separated and solved separately. The variables (s) and (t) are treated separately and equations (25) and (26) are solved for s and t respectively.

These latter modifications do not effect the accuracy of the solution of the finite difference system. The maximum error for computation was set at 0.1%. Comparison of pressure distributions from increasingly dense grid spacings indicates that a variable spacing of 50 points in the $(x_a, x_b)$ interval is sufficient for an error of less than 1% in the pressure distribution due to the finite difference representation.

## Results

Two objectives were pursued in this investigation. The first was to determine the details of the distribution of shear stress on the lower surface and the distribution of pressure for a typical fluid in a typical operation. The second objective was to map out the system parameters over the entire range of fluids and operations.

For the first investigation a fluid was chosen with $d_o = 1. \times 10^{-3}$ slugs in $^{-3}$, $z = 2. \times 10^{-5}$ reyn, $b = 0.0$ psi$^{-1}$, $e = f = 0.0$ psi$^{-1}$ and $k = 0.0$ psi in case A, $k = .1$ psi$^{-1}$ in case B. The operation was chosen with $R = 2.0$ in, $h_o = 3 \times 10^{-4}$ in, $u_1 = u_2 = 100$ in/sec in case I and $13\ u_1 = 7\ u_2 = 910$ in/sec in case II. The resulting distribution in all cases $x_a = .75$ in./s of shear stress on the lower surface and of pressure are shown in Figures 49 through 51. This fluid was chosen to eliminate the effects of pressure on either the density or viscosity functions.

The results of the second investigation follow from the first by varying the fluid and operation parameters. In addition the previously introduced independent parameters, the dependent parameters of load per unit length (W) and traction in the lower surface per unit length (TR) are of interest. In accordance with standard conventions (TR) is positive when it is to the

## Computational Flow Chart

(Subscript (i) refers to inlet region and subscript (e) refers to outlet region. (JAC) is the jacobian of the set of equations in the first argument with respect to the set of variables in the second argument. (ERR) is the relative error function of the set of variables in the argument. (eps) is the error criterion. (g.t.) is (greater than).}

1.  Read system parameters $(x_a, R, U, A, d_0, e, f, z_0, p, k)$

2.  Read state parameter $(h_0)$

3.  Read grid spacing $(dx_I)^T = (dx_{Ii}, dx_{Ie})^T$

4.  Read or calculate starting solution $(s_I^0, p_{I+1}^0, x_b^0)^T$

5.  Set $(s_I^*, p_{I+1}^*, x_b^*)^T = (s_I^0, p_{I+1}^0, x_b^0)^T$

6.  Calculate $(A_{Ii,Ji+1}) = (JAC(T_{Ii}^*, p_{Ji+1}^*)$

7.  Solve $(T_{Ii}^*)^T = (A_{Ii,Ji+1})(p_{J+1} - p_{J+1}^*)$

8.  Calculate $(s_{Ii})^T$

9.  Set $(s_{Ii}^*, p_{Ii+1}^*)^T = (s_{Ii}, p_{Ii+1})^T$

10. If $(ERR((s_{Ii}^*, p_{Ii+1}^*)^T))$ g.t. (eps), go to (6)

11. Calculate $(A_{Ie,Je+1}) = (JAC(T_{Ie}^*, p_b^*), (p_{Je+1}^*, x_b^*)))$

12. Solve $(T_{Ie}^*, p_b^*)^T = (A_{Ie,Je+1})(p_{Je+1} - p_{Je+1}^*), (x_b - x_b^*)^T$

13. Calculate $(s_{Ie})^T$

14. Set $(s_{Ie}^*, p_{Ie+1}^*, x_b^*)^T = (s_{Ie}, p_{Ie+1}, x_b)^T$

15. If $(ERR((s_{Ie}^*, p_{Ie+1}^*, x_b^0)^T))$ g.t. (eps), go to (11)

16. Set $(s_I^0, p_{I+1}^0, x_b^0)^T = (s_I^*, p_{I+1}^*, x_b^*)^T$

17. If $(ERR((s_I^0, p_{I+1}^0, x_I^0)^T))$ g.t. (eps) go to (5)

18. Write $(s_I, p_{I+1}, x_b)^T$

Figure 48
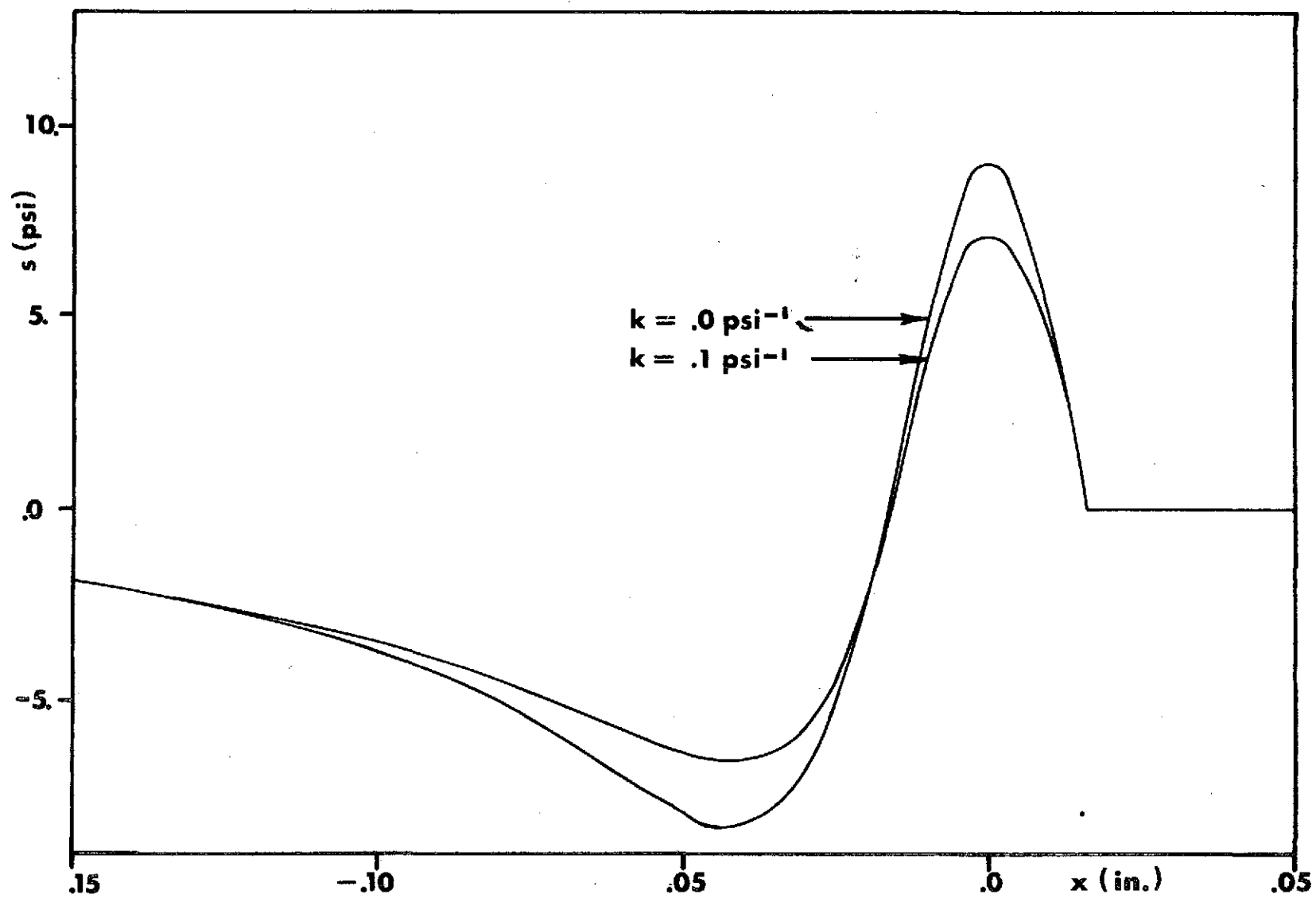
**Figure 49. Distribution of Shear Stress on the Lower Surface for 0% Slip.**
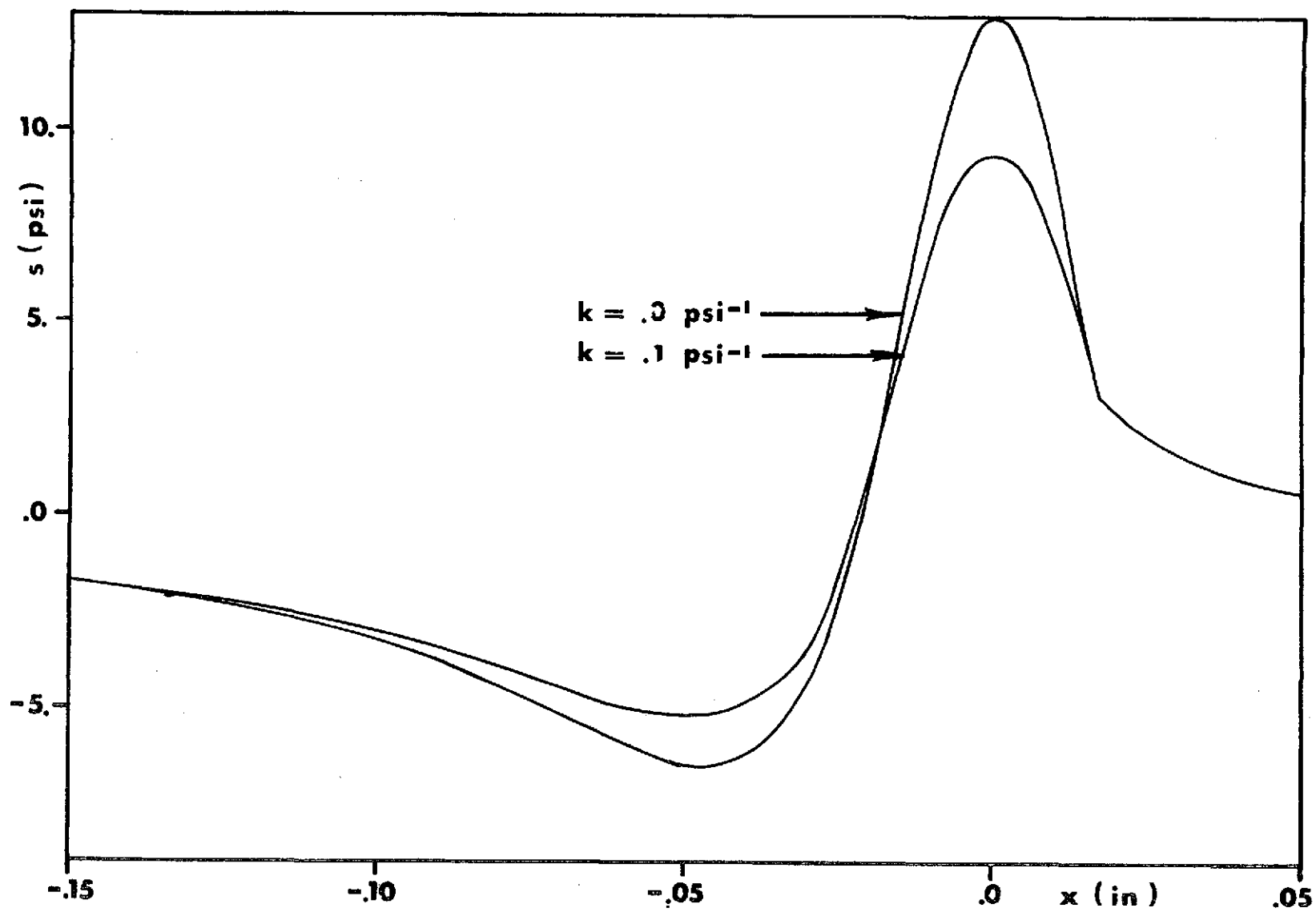
**Figure** 50 . **Distribution of Shear Stress on the Lower Surface for 60 % Slip.**

**Figure 51** Distribution of Pressure.

right in Figure 46. For convenience and economy of display the following nondimensional parameters are introduced

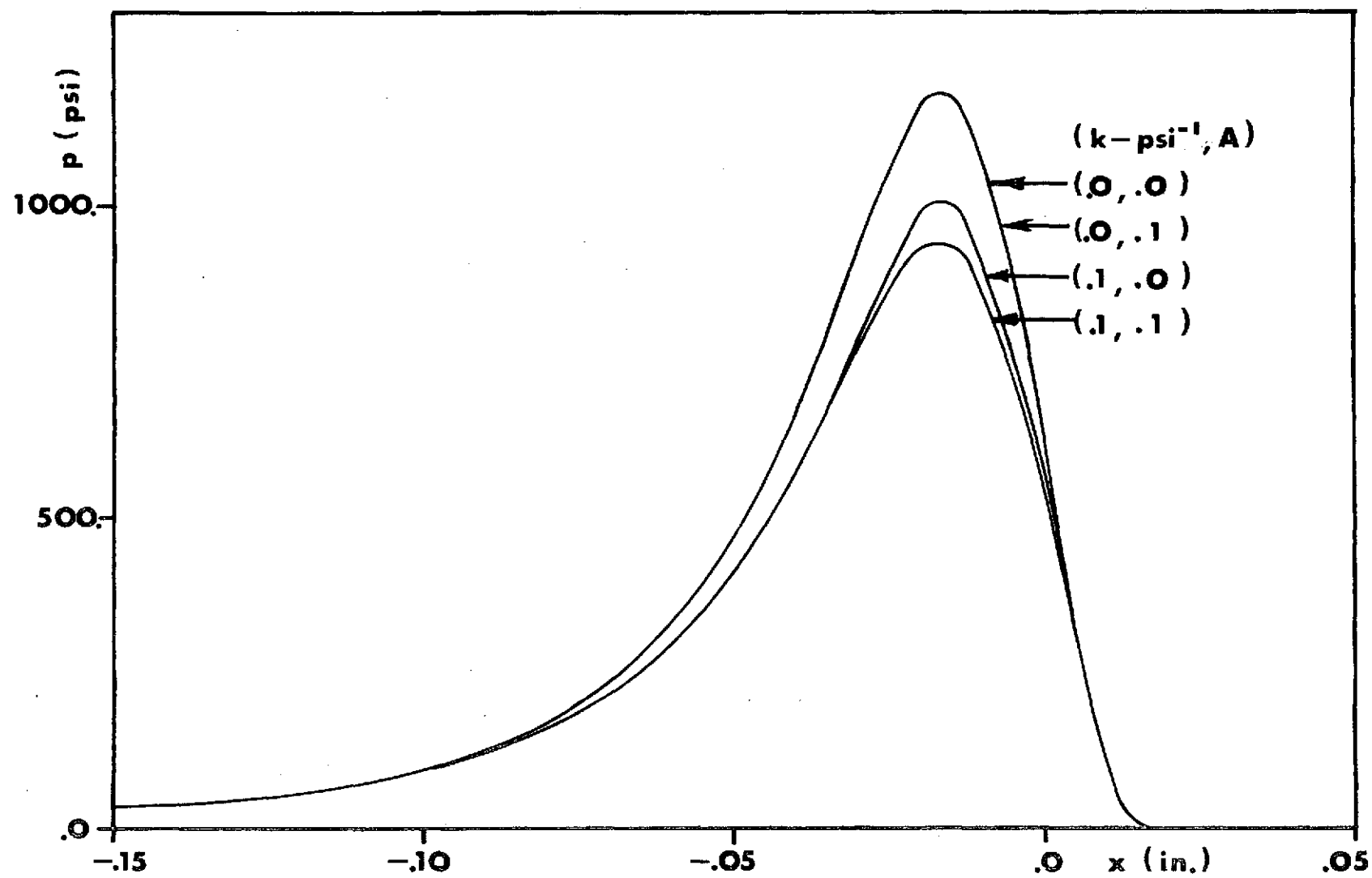$$GI = b \ (2 \ k \ h_o^{-1})^{\frac{1}{2}} \ z_o \cdot U \ h^{-1} \qquad \text{(operation parameter)}$$

$$G2 = k \ z_o \cdot U \ h_o^{-1} \qquad \text{(fluid parameter)}$$

$$G3 = A \qquad \text{(slip parameter)}$$

$$WT = .5 \ W \ R^{-1} \ (z_o \cdot U \ h_o^{-1})^{-1} \qquad \text{(load parameter)}$$

$$TRT = .5 \ TR \ R^{-1} \ (z_o \cdot U \ h_o^{-1}) \qquad \text{(traction parameter)}$$

$$TRC = T/W = TRT/Wt \qquad \text{(traction coefficient)}$$

Nondimensional curves for (WT) and (TRC) are shown in Figures 52 and 53. These curves were calculated for a fluid with $e = f = 0.0 \ psi^{-1}$ (i. e. constant density).

## Discussion

The solution of the system for a given set of data requires 50-100 seconds of CPU time on the Univac 1108. Not all solutions can be obtained from a fixed starting solution such as a linearized system. However, the continuation of solutions yields solutions in all cases of interest. The solutions for $b = 0.0 \ psi^{-1}$ (GI = 0) and $h_o = 0.0003$ indicate a large reduction in peak pressure in cases B compared with cases A (i. e. shear thinning compared to constant viscosity fluids). This results in loss of load capacity. This loss may be significant at high values of the operation parameter (GI). Similarly, there is a large reduction in the peak shear stress on the lower surface and the traction on the lower surface as the fluid parameter (G2) increases. Such behavior is typical for this class of fluids. The maximum pressures are maintained at a low level (under 2000 psi) throughout this investigation so as not to invalidate the assumption of rigid cylinders. At these pressure levels the effects of fluid compressibility are negligible.
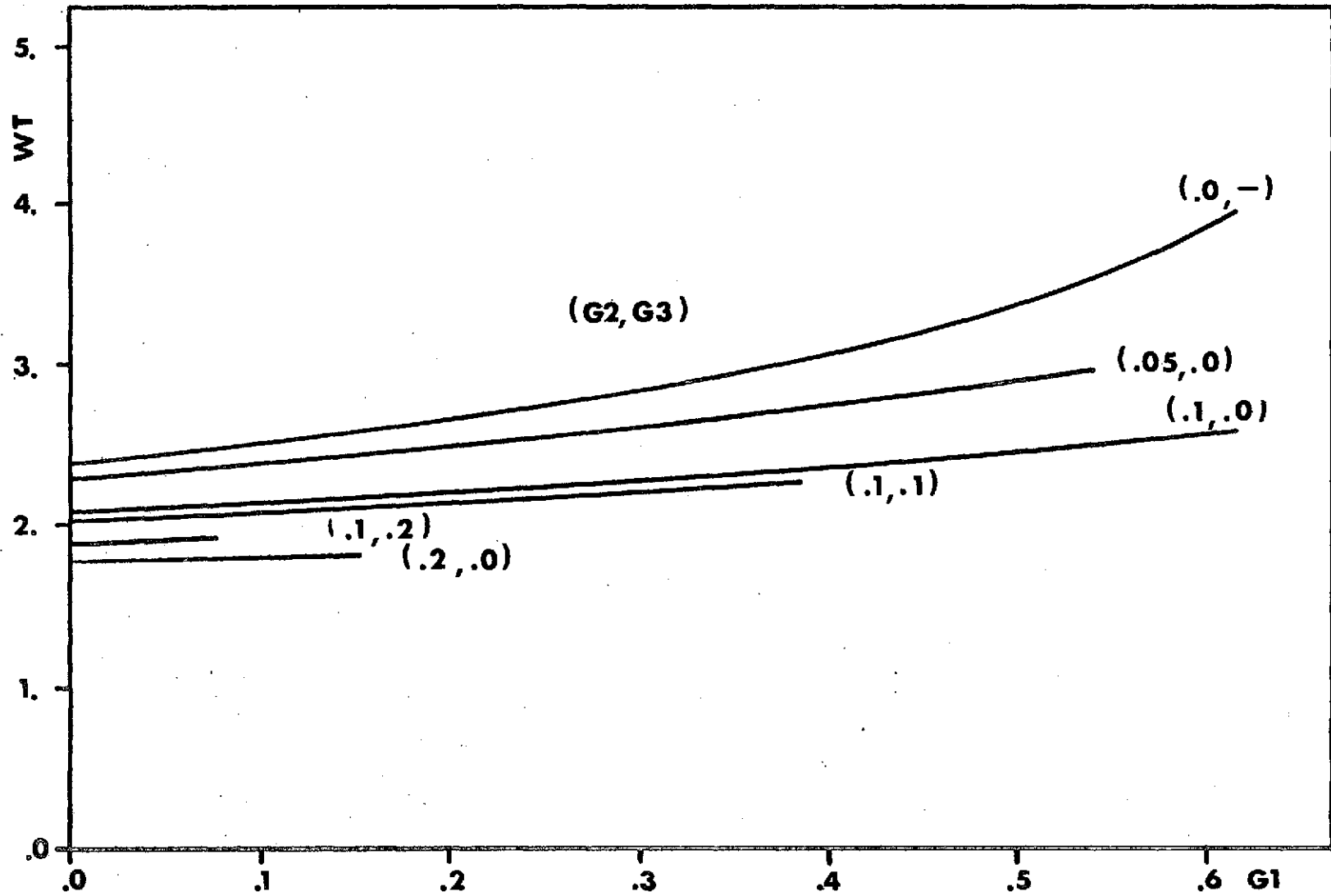
**Figure** 52. **Nondimensional Load (WT) as a Function of Operation Parameter (G1) & Shear Stress Parameter (G2) & Slip Parameter (G3).**
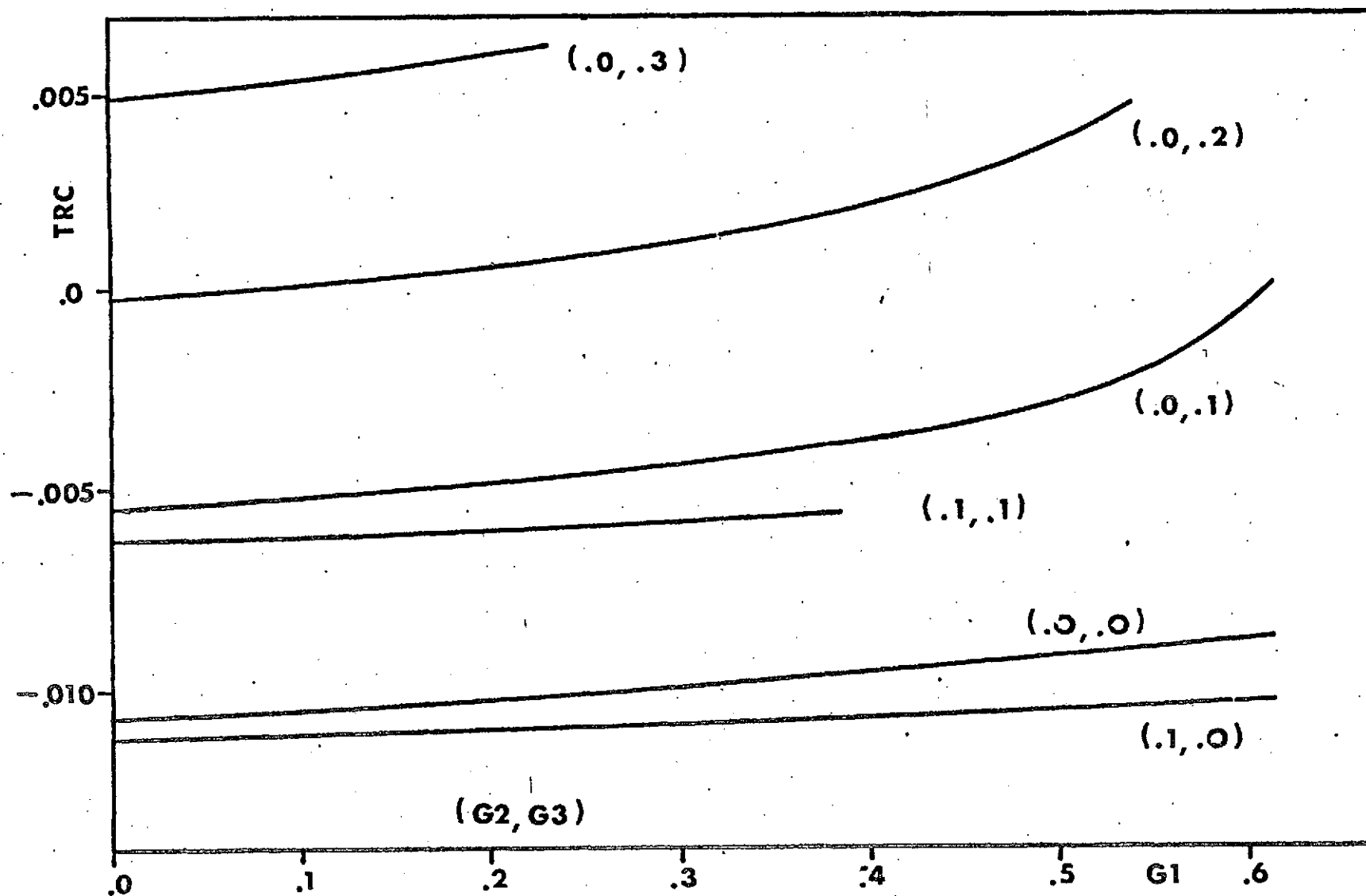
Figure 53, Traction Coefficient (TRC) as a Function of Operation Parameter (G1) & Shear Stress Parameter (G2) & Slip Parameter (G3).

The non-dimensional charts indicate the expected general behavior and are useful as a rough guide to the designer. Such information for the case $k = 0.0$ psi$^{-1}$ and $b = 0.0$ psi$^{-1}$, i. e. for fluids with a constant viscosity function has been presented by Peppler (19) and Cameron (20). The points on the GI = 0 axis of these charts are in agreement with the results for conditions of G1 = G2 = 0. It is interesting to note the large range of negative traction coefficients indicating conditions under which cylinder 1 cannot drive cylinder 2. These charts also allow the measurement of fluid properties, i. e. k, through measurements of the load and traction coefficients.

The methods developed here are readily applied to other fluid models, such as those of the Ree-Eyring, Maxwell, and Reiner-Philippoff type. Similar results have already been obtained for fluids of the Reiner-Philippoff type, but are not reported here. Further, the methods are not restricted to viscosity deviations expressible as combinations of elementary functions.

The objective of this program is to extend these investigations to consider the general viscous lubrication of rolling and sliding elastic cylinders. This work is making progress and results should be forthcoming in the next few months. Calculations for the elastic deformation due to an arbitrary surface pressure have been successfully carried out. It is only necessary to introduce these computational procedures into the programs used for the rigid cylinders.

## Conclusion

Preliminary results in the investigations of the general viscous lubrication of rolling and sliding elastic cylinders have been presented. These are only valid under light loads but indicate the direction of the

investigation and the results to be obtained. The problem formulation and the method of solution will remain essentially the same under heavy loads. These preliminary results have value in themselves. The non-dimensional charts allow the evaluation of lubricants in terms of their shear stress behavior and also allow the rational design of systems employing such fluids.

d.  Energy Dissipation

There is a large variation in the amount of energy dissipated in a lubricant at various locations in gas turbine or reciprocating engines. The amount of energy dissipation can influence the effective viscosity of the lubricant both by increasing its temperature and, in some cases, by molecular degradation.

With respect to shear rates, engine lubrication conditions fall into three catagories which will be designated A, B and C.  Region A has low shear rates which occur in the oil pump inlet and drainage galleries and corresponds to the shear rates commonly encourtered in kinematic viscosity measurements.  Typically film thicknesses are large (>.01m). Behavior in this shear rate range is very important for lubricant circulation particularly at low temperature.

Region B corresponds to what might be called typical hydrodynamic lubrication as occurs in crankshaft journal bearings and other hydrodynamic sleeve bearings in engines and transmissions.  Depending on operating speed, the surface velocities are of the order 1-10 m/s and the film thickness is typically on the order of $10^{-5}$m resulting in shear rates of $10^5 - 10^6 s^{-1}$.  Shear stresses will be on the order of $10^4$ N/m$^2$.

Region C corresponds to elastohydrodynamic lubrication (EHD) conditions such as might be expected in gears, cams, tappets, and other concentrated load contacts in the system.  These are mechanically the most severe conditions to which the lubricant is subjected.  The surface velocities of these contacts are about the same or somewhat lower than those of the journal bearing, but the film thicknesses are typically 100 times smaller, resulting in shear rates of at least an order of magnitude larger.  Shear stresses are not as easily estimated for EHD conditions because the

pressures are very high causing an increase in viscosity, but EHD ex-
periments done in this laboratory suggest that average shear stresses are
$10^7$ N/m$^2$.

Because of the magnitude of the shear stresses in regions B and
C, mechanical degradation of the lubricant is possible. The field of
mechanical degradation of polymers has been reviewed recently by Casale,
Porter and Johnson [21]. They show that although mechanical degrada-
tion does occur in polymer solutions, it is a very inefficient process
when viewed from energy considerations. In some cases, the energy per
mole required to break molecular bonds is as much as a million times the
activation energy of C-C bonds.

Table 12 compares typical shear rates, shear stresses, energy
dissipation rates and friction power factors for regions A, B and C. The
energy dissipation rate can be defined either as the energy dissipated per
unit time per unit volume or per mass of lubricant passing through the
contact. The friction power factor is simply the energy dissipated per
unit time per unit bearing area. To calculate these quantities, the
simple model of a lubricated contact shown in Figure 54 is assumed. The
shear stress, shear rate and film thickness (h) of the shaded volume of
fluid have already been mentioned and are entered in Table 12. The energy
dissipation rate per unit volume is simply the shear stress times the
shear rate and it too is entered in Table 12. However, what is more im-
portant for mechanical degradation is the energy dissipated per unit mass
of the fluid passing through the volume. This is obtained by multiplying
the dissipation rate per unit volume times the volume and dividing by the
mass flow rate through the volume.

The energy dissipation rate per gram-mole is obtained by
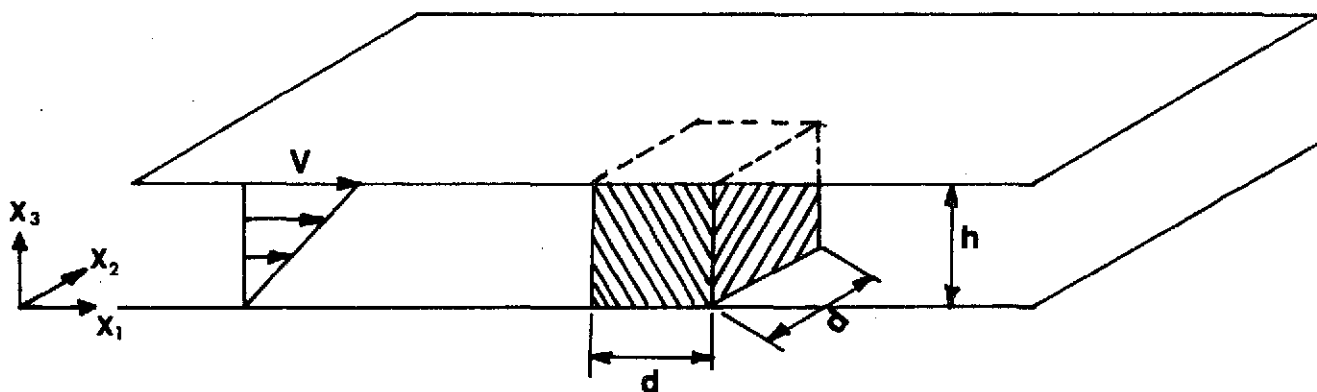
Figure 54    Simplified Model of a Lubricated Contact.

Table 12. Typical Conditions in Lubrication Regimes
as Relating to Mechanical Degradation of
Polymers

| Variable | Units | A Low Shear | B Hydrodynamic Lubrication | C Elastohydrodynamic Lubrication |
|---|---|---|---|---|
| $\dot\gamma$ = shear rate | $s^{-1}$ | $\leq 10^3$ | $10^5 - 10^6$ | $10^6 - 10^7$ |
| $\tau$ = shear stress | $N/m^2$ | $\leq 10^2$ | $10^4$ | $10^7$ |
| $\tau\dot\gamma$ = energy dissipation rate per volume | $W/m^3$ | $\leq 10^5$ | $10^9 - 10^{10}$ | $10^{13} - 10^{14}$ |
| $\dfrac{2\tau d}{\rho h}$ = energy dissipation rate per mass flow | $J/kg$ | $\leq 10^{-1}$ | $10^5$ | $10^8$ |
| $\dfrac{2\tau d(MW)}{\rho h}$ = energy dissipation rate per kmole | $J/kmole$ | $\leq (MW)10^{-1}$ | $(MW)\cdot 10^5$ | $(MW) \cdot 10^8$ |
| $2\dot\gamma h$ = friction power factor | $W/m^2$ | $10^3$ | $10^4 - 10^5$ | $10^7$ |

multiplying the dissipation rate per unit mass by the molecular weight. Finally, the friction power factor is simply the energy input rate per unit volume multiplied by the film thickness. These values have also been entered in Table 12.

Table 13 lists the shear rate, shear stress, energy input rate per unit volume, friction power factor and energy input rate per gram mole of lubricant for the fluids supplied by NASA for examination in this laboratory. If one recalls that the activation energy for a kmole of carbon-carbon bonds is $3.4 \times 10^8$ J/kmole, it is not surprising that some degradation occurs in region C and possibly even region B.

In fact, what is surprising when viewed in light of the numbers in Table 13, is that more degradation does not occur. However, in the review paper by Casale et al. [21] several studies on the mechanical degradation of polymers are cited which indicate that mechanical degradation is a very inefficient process, requiring as much as a million times $(10^6)$ more energy than the activation energy for the bond. Clearly, in the EHD areas (regime C) some mechanical degradation is to be expected and it is probably these (EHD) conditions which cause the degradation observed in the engine tests of Wright and Johnson (22) and Selby and West (23).

An investigation has recently been conducted in this laboratory under sponsorship of the National Science Foundation to study molecular degradation in a single EHD sliding point contact. Several fluids including polymer blends and silicones have been investigated. The permanent loss of viscosity and the change in molecular weight distribution of the sample have been determined. Analysis of the fluids was made on a few micro-liter sample extracted from the exit region of the EHD contact.

Table 13 Typical Elastohydrodynamic Lubrication
Conditions for NASA Supplied Fluids. *

| Fluid | U | $\dot{\gamma} \times 10^{-6}$ | $\tau_{avg} \times 10^{-6}$ | $\dot{\gamma}\tau_{avg} \times 10^{-12}$ | $\dot{\gamma}\tau_{avg}h \times 10^{-6}$ | $\dfrac{2\tau d(MW)}{\rho h} \times 10^{-6}$ |
|---|---|---|---|---|---|---|
| | m/s | s$^{-1}$ | N/m$^2$ | W/m$^3$ | W/m$^2$ | J/kmole |
| Advanced | .35 | 9.5 | 42 | 400 | 14 | 860 (MW) |
| Ester | 1.4 | 9.3 | 25 | 230 | 34 | 120 (MW) |
| Formulated | .35 | 7.6 | 51 | 390 | 18 | 780 (MW) |
| Advanced Ester | 1.4 | 8.2 | 29 | 240 | 41 | 120 (MW) |
| Naphthenic Mineral Oil | .35 | 1.4 | 58 | 81 | 20 | 190 (MW) |
| Plus Additive | 1.4 | 2.7 | 35 | 95 | 48 | 55 (MW) |
| Synthetic Paraffinic | .35 | .89 | 40 | 36 | 14 | 86 (MW) |
| Mineral Oil Plus Additive | 1.4 | 1.9 | 24 | 46 | 35 | 27 (MW) |
| DN600 | .35 | 5.0 | 38 | 190 | 13 | 460 (MW) |
| Plus Additive | 1.4 | 7.3 | 29 | 210 | 40 | 130 (MW) |
| FN 2961 | .35 | 1.4 | 50 | 70 | 18 | 160 (MW) |
| | 1.4 | 3.2 | 38 | 120 | 51 | 71 (MW) |
| MCS 460 | .35 | 2.7 | 69 | 190 | 25 | 410 (MW) |
| | 1.4 | 5.1 | 51 | 260 | 70 | 140 (MW) |
| MCS 418 | .35 | 3.5 | 53 | 190 | 19 | 320 (MW) |
| | 1.4 | 6.3 | 40 | 250 | 55 | 110 (MW) |
| DN-600 | .35 | 5.0 | 34 | 170 | 12 | 400 (MW) |
| | 1.4 | 7.3 | 26 | 190 | 36 | 110 (MW) |
| XRM-109F | .35 | .97 | 47 | 46 | 17 | 110 (MW) |
| | 1.4 | 1.8 | 21 | 38 | 23 | 23 (MW) |
| KRYTOX | .35 | .92 | 68 | 62 | 24 | 68 (MW) |
| | 1.4 | 1.8 | 40 | 72 | 55 | 20 (MW) |

*for 67N normal load, $3.53 \times 10^{-4}$ m contact diameter, pure sliding.

Results indicate that a single pass through an EHD contact is sufficient
to significantly alter the rheology of many lubricants.

REFERENCES

1. Novak, J. D. An Experimental Investigation of the Combined Effects of Pressure, Temperature and Shear Stress Upon Viscosity. Doctoral Thesis, Univ. of Mich., 1968.

2. Winer, W. O., and Novak, J. D., "Some Measurements of High Pressure Lubricant Rheology", Journal of Lubrication Technology, Trans. ASME, Series F., Vol. 90, No. 3, July 1968, pp. 580-591.

3. Pressure-Viscosity Report, Vols. I and II, a report prepared by the ASME Research Committee on Lubrication, ASME, New York, 1953.

4. Hersey, M. D. Theory and Research in Lubrication, New York, Wiley and Sons, Inc. 1966.

5. Appledoorn, J. K., Physical Properties of Lubricants, Chap. 8, Boundary Lubrication, An Appraisal of World Literature, The ASME Committee on Lubrication, New York, 1969.

6. Eckert, E. R. G., and Drake, R. M., Jr., Analysis of Heat and Mass Transfer, McGraw-Hill , 1972.

7. Winer, W. O., Sanborn, D. M., and Jakobsen, J., Investigations of the Rheology of a Series of Silicones as Related to Elastrohydrodynamic Lubrication, a Report Prepared for Dow Corning Corporation, Midland, Michigan. Georgia Institute of Technology, Atlanta, Georgia, November 1972.

8. Wright, W. A. and Crouse, W. W. Jr., "A New Concept in Generalizing Non-Newtonial Fluid Flow Data", ASLE-ASME Lubrication Conference, Washington, D. C., Oct. 1964, Reprint No. 64-LC-11.

9. Winer, W. O., Fluid Measurements NASA Report No. NAS3-15383. Georgia Institute of Technology, Atlanta, Georgia, January 1972.

10. Winer, W. W., Sanborn, D. M., Lee, D., Jakobsen, J., Carlson, S., and Bohn, M. Investigations of Lubricant Rheology as Applied to Elastohydrodynamic Lubrication, NASA Report No. 11-002-133, Georgia Institute of Technology, Atlanta, June 1970.

11. Winer, W. O. and Ehya, H., High Pressure Rheology of Four Solutions of Polytetene in Paraffinic Base Oil, NASA Report No. C-57357-B, University of Michigan, Ann Arbor, Michigan 1969.

12. Sanborn, D. M. and Winer, W. O., "Fluid Rheological Effects in Sliding Elasthydrodynamic Point Contacts with Transient Loading: 1 - Film Thickness", Trans. ASME, Journal Lubrication Technology, Vol. 93, pp. 262-271, 1971.

13. Sanborn, D. M., and Winer, Wo. O., "Fluid Rheological Effects in Elastohydrodynamic Point Contacts with Transient Loading II - Traction", Trans. ASME, Journal of Lubrication Technology, Vol. 93, pp. 342-348, 1971.

14. Kebler, R. W., "Optical Properties of Synthetic Sapphire", Linde Company, 30 East 42nd St., New York, New York.

15. McMahon, H. O., "Thermal Radiation From Partially Transparent Reflecting Bodies", <u>Journal of the Optical Society of America</u>, Vol. 40, No. 6, pp. 376-380, 1950.

16. Kreith, F., <u>Principles of Heat Transfer</u>, International Textbook Company, pp. 177-180, 1964.

17. Sanborn, D.M., <u>An Experimental Investigation of the Elastohydrodynamic Lubrication of Point Contacts in Pure Sliding</u>, Ph.D. Dissertation, University of Michigan, Dec. 1969 and University Microfilms, Inc., Ann Arbor, Michigan.

18. Jakobsen, J., <u>Lubricant Rheology at High Shear Stress</u>, Ph.D. Dissertation, Georgia Institute of Technology, 1973 (to be completed).

19. Peppler, W., "Druckubertragung an Geschmieter Zylindrischen Gleit - und Walzflachen," VDI - Forschungsheft 391 (1938), VDI-Verlag A.M.B.H., Berlin, pp. 1-24.

20. Cameron, A., "Hydrodynamic Theory in Gear Lubrication", Journal of The Institute of Petroleum," J. 38 (1952), pp. 614-622.

21. Casale, A., Porter, R. S., and Johnson, J. F., "The Mechano-chemistry of High Polymers," Rubber Chemistry and Technology, <u>44</u>, April 1971.

22. Wright, W. A., and Johnson, R. H., "Rheological Properties of Automatic Transmission Fluid", SAE Paper, May 1968

23. West, J. P. and Selby, T. W., "The Effect of Engine Operation on the Viscometric Properties of Multigraded Engine Oils", May 1965, SAE Paper No. 650445.

APPENDIX A

DESCRIPTION OF FLUIDS

The table summarizes the investigated fluids and gives characteristic data for each fluid.

## Experimental Fluids

Diester-Plexol 201 bis-2-ethyl hexyl sebacate

Dimethyl Siloxane DC-200-50

Polyalkyl Aromatic plus additive

Synthetic Paraffinic Hydrocarbon plus antiwear additive

Paraffinic Base Oil R-620-12 plus 11.5% Polyalkylmethacrylate $(MW = .2 \times 10^6)$.

## Characterization

Diester

Source - Rohm and Haas Company

Data supplied with the sample

| | |
|---|---|
| Viscosity at 210°F | 3.32 cs |
| Viscosity at 100°F | 12.75 cs |
| Viscosity at -65°F | 7988 cs |
| Viscosity Index (D-2270) | 150 |
| Neutralization number (D-974) | 0.02 |
| Cloud Point (D-2500)°F | below -65 |

Data transferred from literature sources

Heat conductivity at 100°F .087 Btu/h ft °F

37.8°C

.0188 lbf/°F sec

.0154 kp/°C sec

Specific Heat per unit mass 0.46 Btu/lbm °F

at 100°F 0.46 cal/gramm °C

37.8°C 4295 lbf in/lbm °F

Density at 77°F .0328 lbm/in$^3$

25°C

.91 gramm/cm$^3$

Specific Heat per unit volume .01303 Btu/°F in$^3$

.416 cal/°C cm$^3$

139.5 lbf/in$^2$ °F

Heat diffusivity 1.35 x 10$^{-4}$ in$^2$/sec

8.69 x 10$^{-4}$ cm$^2$/sec

Data measured

Kinematic viscosity at at 100°F 12.65 cs

37.8°C

at 210°F 3.33 cs

98.9°C

at 300°F 1.775 cs

148.9°C

Density at 100°F .903 gramm/cm$^3$

37.8°C

|  |  |  |  | at | 210°F | .86 gramm/$cm^3$ |
|  |  |  |  |  | 98.9°C |  |
|  |  |  |  | at | 300°F | .825 gramm/$cm^3$ |
|  |  |  |  |  | 148.9°C |  |

| | | |
|---|---|---|
| Viscosity | at 100°F | 11.41 cp |
| | 37.8°C | |
| | at 210°F | 2.86 cp |
| | 98.9°C | |
| | at 300°F | 1.46 cp |
| | 148.9°C | |
| | at 32°F | 57.5 cp |
| | 0°C | |
| | at 10°F | 130 cp |
| | -12.2°C | |
| Pressure viscosity | at 32°F | Z = .51 |
| Coefficient (Roelands) | 0°C | |

Elastohydrodynamic film thickness and traction data taken at 15 lbf load
(150 kpsi peak Hertzian pressure) 1 1/4 inch diameter steel ball loaded
against a sapphire anvil

| Sliding speed | 13.7 ips | 27.4 ips | 54.8 ips | 92.1 ips |
|---|---|---|---|---|
| $h_c$ ($\mu$-inch) | .4 | .8 | 2.1 | 3.3 |
| $h_m$ ($\mu$-inch) | .4 | .8 | 1.3 | 1.3 |
| TC | .046 | .032 | - | .025 |

Dimethyl Siloxane DC-200-50

Source Dow Corning Corporation, Midland, Michigan,

Data supplied with the sample

Degree of polymerization 43

Data measured

| | | | | | | |
|---|---|---|---|---|---|---|
| Viscosity | at 77°F | 25°C | 50 | cs | 48 | cp |
| | at 100°F | 37.8°C | 41.5 | cs | 39.1 | cp |
| | at 210°F | 98.9°C | 17 | cs | 15.7 | cp |
| | at 300°F | 148.9°C | 8.6 | cs | 7.3 | cp |

| | | | |
|---|---|---|---|
| Density | at 77°F | 25°C | .954 gramm/cm$^3$ |
| | at 100°F | 37.8°C | .943 gramm/cm$^3$ |
| | at 210°F | 98.9°C | .894 gramm/cm$^3$ |
| | at 300°F | 148.9°C | .850 gramm/cm$^3$ |

Pressure viscosity characteristics

| at | | | $\alpha_{OT}$ psi$^{-1}$ | $\alpha^*$ psi$^{-1}$ | Z |
|---|---|---|---|---|---|
| at | 75°F | 23.9°C | $1.28 \times 10^{-4}$ | $.98 \times 10^{-4}$ | .52 |
| at | 100°F | 37.8°C | $1.36 \times 10^{-4}$ | $.96 \times 10^{-6}$ | .51 |
| at | 210°F | 98.9°C | $1.53 \times 10^{-6}$ | $.96 \times 10^{-4}$ | .44 |
| at | 300°F | 148.9°C | $1.53 \times 10^{-4}$ | $.96 \times 10^{-6}$ | .43 |

Roelands temperature viscosity slope index

$$S = .55 \qquad \text{re atmospheric pressure.}$$

Elastohydrodynamic film thickness and traction.

Data taken at 15 lbf load (150 kpsi peak Hertzian pressure)

1 1/4 inch diameter steel ball loaded against a sapphire anvil.

| Sliding speed | 13.7 ips | 27.4 ips |
|---|---|---|
| $h_c$ ($\mu$-inch) | 2 | 3 |
| $h_m$ ($\mu$-inch) | 1 | 2 |
| TC | .069 | .061 |

Polyalkyl Aromatic plus additive.

Source NASA Lewis Research Center, Cleveland, Ohio.

Data supplied with the sample

| Kinematic viscosity | at 100°F | 37.6 cs |
|---|---|---|
| | at 210°F | 6.1 cs |

Data measured (40)

| | 100°F | 210°F | 300°F |
|---|---|---|---|
| | 37.8°C | 98.9°C | 148.9°C |
| Viscosity cp (p = atm) | 32.2 | 5.0 | 2.1 |
| $a_{OT}$ psi$^{-1}$ | $1.41 \times 10^{-4}$ | $1.39 \times 10^{-4}$ | - |
| $a^{*}$ psi$^{-1}$ | $1.17 \times 10^{-4}$ | $.88 \times 10^{-4}$ | - |

Elastohydrodynamic film thickness and traction

Data taken at 15 lbf load (150 kpsi peak Hertzian pressure)

1 1/4 inch diameter steel ball loaded against a sapphire anvil.

| Sliding speed | 13.7 ips | 27.4 ips | 54.8 ips |
|---|---|---|---|
| $h_c$ ($\mu$-inch) | 3 | 4 | 8 |
| $h_m$ ($\mu$-inch) | 2 | 2 | 4 |
| TC | .055 | .048 | .042 |

Synthetic Paraffinic Hydrocarbon (XRM 109 F4)

Source NASA Lewis Research Center, Cleveland, Ohio.

Data measured

| | 100°F | 210°F | 300°F |
|---|---|---|---|
| | 37.8°C | 98.9°C | 148.9°C |
| Viscosity cp | 376 | 31.6 | 10.2 |
| $a_{OT}$ psi$^{-1}$ | $1.52 \times 10^{-4}$ | $1.37 \times 10^{-4}$ | $1.11 \times 10^{-4}$ |
| $a^{*}$ psi$^{-1}$ | $1.37 \times 10^{-4}$ | $1.04 \times 10^{-4}$ | $.89 \times 10^{-4}$ |
| Z | .44 | .46 | .47 |

Synthetic Paraffinic Hydrocarbon plus Antiwear Additive (XRM 177 F-4)

Source NASA Lewis Research Center, Cleveland, Ohio

Data measured

|  | 100°F | 210°F | 300°F |
|---|---|---|---|
|  | 378°C | 98.9°C | 148.9°C |
| Viscosity cp | 37.6 | 31.6 | 10.2 |
| $\sigma_{OT}$ psi$^{-1}$ | $1.52 \times 10^{-4}$ | $1.37 \times 10^{-4}$ | $1.11 \times 10^{-4}$ |
| $\sigma^*$ | $1.35 \times 10^{-4}$ | $1.07 \times 10^{-4}$ | $.86 \times 10^{-4}$ |
| Z | .44 | .46 | .46 |

Fluid XRM 177 F4 is of the same composition as the previous investigated fluid D.     The base fluid is however not from the same lot.

Elastohydrodynamic film thickness and traction for fluid D. Data taken at 15 lbf load (150 kpsi peak Hertzian pressure) 1 1/4 inch diameter steel ball loaded against a sapphire anvil

| Sliding speed | 13.7 ips | 27.4 ips | 54.8 ips |
|---|---|---|---|
| $h_c$($\mu$-inch) | 15 | 23 | 30 |
| $h_m$($\mu$-inch) | 7 | 13 | 19 |
| TC | .058 | .045 | .035 |

Paraffinic Base Oil R-620-12 plus 11.5% Polyalkylmethacrylate ($MW = 2.\times10^{6}$).

Data supplied with the sample

Base oil  R-620-12

Source:  Sun Oil Company

Viscosity  33.33 cs at 100°F (37.8°C)  5.336cs at 210°F (98.9°C)

SUS/100          156.2          SUS/210          43.74

Viscosity index   (ASTM D-2270)        102

Flash point                            410°F

Fire point                             470°F

Pour point                               5°F

Refractive index                       1.4754

Density gramm/cm$^3$                    .8596

Molecular weight (MW)                   401   *

Polyalkylmethacrylate  PL 4523.  (PAMA)

Source Rohm and Haas Company

The polymer was in solution with a paraffinic base oil, a 150 neutral carrier oil similar to the base oil R-620-12. Their chemical composition are alike. They differ only in their molecular weight. The solution contains 19% polymer. It has a kinematic viscosity of 773 cs re 210°F (98.9°C). The molecular weight is $4.51 \times 10^6$ as measured with a permeation chromatography method, GPCM. An estimated molecular weight of $2. \times 10^6$ is however found by extrapolating from viscosity and molecular weight data for lower MW polyalkylmethacrylates, MW = $1.28 \times 10^6$, $.828 \times 10^6$ and $.5 \times 10^6$. It is believed that the GPP technique is not suitable for materials with high molecular weights. The molecular weight of $2. \times 10^6$ determined with viscosity measurements are therefore adhered to. The amount polymer reported, 11.5% is the volume concentration in the final solution.

---

Data measured

| | 100°F | 210°F | 300°F |
|---|---|---|---|
| R-620-12 | 37.8°C | 98.9°F | 148.9°C |
| Viscosity (cp) | 29.2 | 4.5 | 1.9 |
| Density (gramm/cm$^3$) | .849 | .809 | .777 |

## Appendix B

An estimate of the equivalent length of a cone can be arrived at as follows:

In a capillary $\Delta p = \phi(\eta 128/\pi)\ (L/D^4) = (K/D^4)L$

and $d(\Delta p) = (K/D^4)dL$

where $\phi$ is the volume flow per sec, then

$$\Delta p_{cone} = \int_{P_{D_o}}^{P^\infty} d(\Delta p) = (K/2tg\Psi)\int_{D_o}^{\infty} D^{-4}dD = (K/D_o^{-4})\ (D_o/tg\Psi)$$

in that

$$dD_o = 2tg\Psi dL$$

For $\Psi = 45°$ the equivalent length of the cone is $0.167\ D_o$

APPENDIX C

## The Effect of Ball Radiation Change on Film Temperature

The energy dissipation rate in the EHD contact can be determined from film thickness and traction measurements previously obtained (12,13). For the most severe conditions imposed in this investigation (1.39 m/s velocity and 67N normal load) the traction force was observed to be 4.7N. This results in an energy input rate (fU) of 6.53 watts.

From radiation measurements made with each of the two balls, the change in ball radiation is of the order $10^2$ watts/ $m^2$-steradian for a 3.6 x $10^{-5}$m diameter spot size. For radiation to one hemisphere ($2\pi$ steradians) and for an EHD contact diameter of 3.6 x $10^{-4}$m, the radiation heat transfer rate is of the order $10^{-5}$ watts. Therefore, the heat transfer through the film due to ball radiation is negligible compared to the 6.53 watts dissipation rate. The effect of different ball surface emissivity on film temperature should therefore be negligible.

APPENDIX D


Relative Contribution of Sapphire Radiation


As an order of magnitude approximation it has been assumed that the upper sapphire surface is at ambient temperature ($25\,^{\circ}C$) and that the lower surface is at a temperature equal to that of the average fluid temperature ($115\,^{\circ}C$). These temperatures correspond to black body areal radiant intensity values of 37 and 400 watts/$m^2$ - ster respectively. This data represents the maximum temperature condition on the contact centerline. The radiation characteristic of the sapphire should be less than the average of the surface radiation values, due to the fourth power relation between temperature and areal radiant intensity. For an average black body areal radiant intensity of 220 watts/$m^2$ - ster and a sapphire emissivity of 0.018, the sapphire areal radiant intensity becomes 4 watts/$m^2$ - ster, which is 2% of the black body ball radiation shown in equation ( 16). The 2% maximum error resulting from omitting the contribution from the sapphire will result in an error in ball temperature of less than $2\,^{\circ}C$.

THE FOLLOWING PAGES ARE DUPLICATES OF

ILLUSTRATIONS APPEARING ELSEWHERE IN THIS

REPORT.   THEY HAVE BEEN REPRODUCED HERE BY

A DIFFERENT METHOD TO PROVIDE BETTER DETAIL